UNIVERSITY OF OSLO
Department of Physics

Substrate, Doping and Annealing Effects on Sputtered Zinc Oxide Thin Films

Thesis Submitted in Partial Fulfilment for the Degree of

Master of Science in Materials, Energy and Nanotechnology

Heine Nygard Riise

May 30, 2013

Abstract

Zinc Oxide is a promising material for reducing the price of solar cells since its high abundance and low cost makes it attractive in replacing the more commonly used and more expensive Indium Tin Oxide as a transparent front contact. Using co-sputtering of Zinc Oxide and Silicon, highly transparent (>80% transmittance in visible range) and low-resistive ($\sim 1\times10^{-3}\Omega$cm) films have been prepared. Annealing of the films in air at temperatures ranging from 550°C to 1050°C leads to an improved crystal quality, but the heat treatment is seen to have an adverse effect on the electrical characteristics of the films. Both the electrical characteristics and the crystal quality of the samples improve with Si doping up to a concentration of 1.5±0.5%. Above this concentration, these properties degrade. The films have been deposited on different substrates, and it is found that deposition on crystalline Silicon and glass produce films of good electrical and crystal quality while deposition on amorphous Zinc Oxide leads to films of poor quality. Although this substrate leads to films of low crystal quality (close to amorphous), the films still have satisfactory electrical and optical properties. It is also found that Silicon and Aluminium addition to the films leads to lower grain sizes suggesting that Silicon and Aluminium act as mobility inhibiting surfactants. Attempts to manufacture Silicon nanocrystals embedded in a Zinc Oxide matrix have been made but they proved to be unsuccessful. This is most likely due to the low formation energy of Silicon Dioxide.

Acknowledgements

I naturally have many people I would like to thank for their help during the past two years.

My two supervisors have been instrumental in the realisation of this thesis. Prof. Bengt Gunnar Svensson has provided me with a very interesting project, has always pointed me in the right direction when the right course of action was not clear and has given me valuable feedback through his meticulous proof-reading of this thesis. Dr. Ramòn Schifano has patiently introduced me to the equipment and new concepts encountered in the course of the thesis work. He has invariably had his door open to me and my endless questions, and through our discussions and his suggestions and corrections, this thesis has been formed.

For his help with SIMS, discussions and general interest in my work, I am grateful to Ass. Prof. Lasse Vines. I would like to thank Dr. Ragnhild Sæterli for performing TEM analysis on my samples, Dr. Augustinas Galeckas for PL measurements and Dr. Alexander Azarov for RBS measurements. To Viktor Bobal I am grateful for helping me whenever something was amiss with the equipment. For help and hints with XRD I am grateful to Dr. Vishnukanthan Venkatachalapathy.

A big thanks to all my friends at LENS for making the past two years enjoyable and for making MiNaLab a pleasant place to work.

Finally, I am immensely grateful to my family for their love and support in everything I do and to Trude for being there for me no matter what.

Contents

Chapter 1

Introduction

In 2003, Nobel Laureate in Chemistry Richard E. Smalley presented a list of the "top ten problems facing humanity over the next 50 years" [1]. Of these challenges, energy ranked the highest, while several of the other issues on the list are closely linked to energy production and supply (e.g. water, food, environment and poverty). Currently in the world, 1.3 billion people do not have access to electricity, effectively hindering any meaningful economic development for this large fraction of the world's population. Meanwhile, the global energy demand will increase by one-third by 2035 with fossil fuels still remaining the most important energy source with a 75% market share. As a consequence, energy-related CO_2 emissions will increase from an estimated 31.2 Gt in 2011 to 37.0 Gt in 2035. This level of CO_2 emission is stipulated to cause a long-term global temperature increase of 3.6°C [2], an increase which will lead to significant challenges regarding freshwater supply, ecosystems sustainability, food production and health issues to name a few [3].

To combat these climate changes and lift billions of people out of poverty, a complete reinvention of our energy systems is required. Energy efficiency schemes and Carbon Capture and Storage (CCS) must be implemented to a higher degree than today and fossil fuels need to be replaced as the world's largest energy source by renewable energy systems. The harvesting of solar energy will play a large role in this transition.

In 2008, solar energy only constituted 0.1% of global energy production, and 0.8% of the total renewable energy production [4]. However, solar Photovoltaics (PV) energy production will increase to cover 7.5% of the total demand for energy in 2035, a 26-fold increase compared to 2010 numbers according to estimates by the International Energy Agency [2]. Achieving such substantial growth demands a decrease in cost and increase in efficiency of solar cells if they are to compete with fossil fuels [5]. New technologies will be needed to meet these demands, and in thin film photovoltaics, Zinc Oxide (ZnO) is a material which can contribute to reducing the cost of solar modules by replacing the more expensive and less abundant [6] Indium Tin Oxide (ITO) as a transparent front side contact. There are many pathways for increasing the efficiency of solar cells, and one promising technique utilises quantum phenomena of nanocrystals to create more than one electron per incident photon.

This thesis explores several aspects related to ZnO as a transparent front contact and Silicon nanocrystals for increased solar cell efficiency. Co-sputtering of ZnO and Silicon (Si) was employed with the aim of precipitating Si nanocrystals in the ZnO matrix, thus forming a material capable of acting as both an electron generating/down-converting agent and as a transparent front contact. Furthermore, to gain insight in and to improve the electrical and

structural characteristics of the sputtered films, the effects of using different substrates and post-deposition annealing treatments on the Si rich ZnO were investigated. Hall effect measurements were utilised to determine the electrical characteristics, X-Ray Diffraction (XRD) was employed to gain information on the crystal structure. The relative elemental composition of the material was established by Rutherford Backscattering Spectrometry (RBS) and surface topography was investigated by Atomic Force Microscopy (AFM). Imaging of the structures of the samples was performed by Transmission Electron Microscopy while the optical properties were examined by Photoluminescence (PL) spectroscopy and transmittance measurements.

Chapter 2

Theory

This chapter introduces some basic concepts of semiconductor physics in general and ZnO in particular. The crystalline nature and electronic characteristics of materials is introduced as a platform for understanding semiconductors in sections 2.1 and 2.2. Certain important properties of ZnO are introduced in section 2.3, while some previous work relevant for this thesis is presented in section 2.4.

2.1 Crystalline Materials

This section is based on the textbooks by Kittel [7] and Hemmer [8].

Any material consists of atoms, and the characteristics of the material is dependent on the properties of the atoms and the interactions between them. In gases and liquids, the interactions are fairly weak and the molecules or atoms are not bound in a certain configuration, and they are free to move. In solids, the interactions are stronger, the atoms are strongly bound to their nearest neighbors and they can not move freely. Based on the configuration between the strongly bound constituents of the solid, the solid can be classified as either amorphous or crystalline: An amorphous solid has no long range order on a micro-scale, and the atoms are randomly positioned. In a *crystalline solid* however, the atoms show a periodic arrangement and have a repetitive pattern. An ideal crystal consists of an infinite repetition of a group of identical atoms called a *basis*. The basis is repeated for each lattice point in the crystal, and the lattice is defined by three translational vectors $\mathbf{a_1}, \mathbf{a_2}$ and $\mathbf{a_3}$, where any integral multiple of these vectors from an arbitrary lattice point will result in a new lattice point. If $\mathbf{a_1}$, $\mathbf{a_2}$ or $\mathbf{a_3}$ represent the smallest distance between two lattice points, they are defined as *primitive vectors*. Figure 2.1 shows a two dimensional case of how a crystal structure is constructed through a lattice and a basis. A cell spanned by the three primitive vectors is a primitive unit cell, with $|\mathbf{a_1}| = a_1$, $|\mathbf{a_2}| = a_2$ and $|\mathbf{a_3}| = a_3$ being the length of the sides of the unit cell termed the lattice constants. Depending on the translation vectors and the angle between them, many different types of crystal lattices may be constructed. A crystal lattice will be mapped onto itself by certain symmetry operations, and depending on which symmetry operations are possible, a specific lattice type can be defined. In three dimensions, there are 14 different lattice types (often named *Bravais lattices*).

A crystal plane has an orientation decided by three non-collinear points, and can be described by the intercepts of the plane with the Cartesian axes in terms of the lattice constants a_1, a_2 and a_3. By taking the reciprocal of the intercepts and then expanding or reducing the

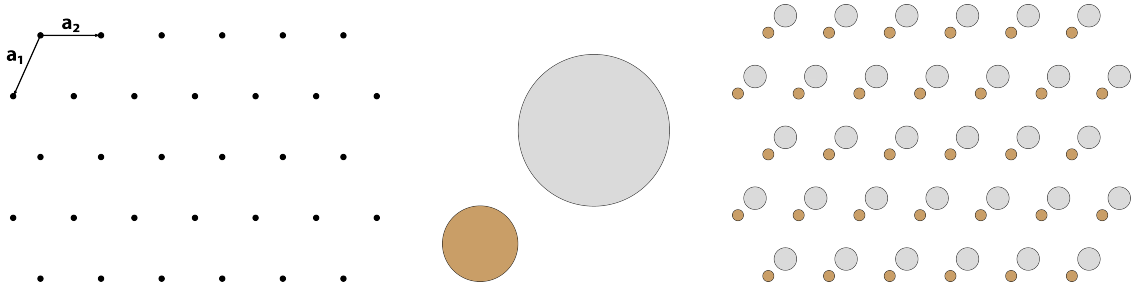

(a) (b) (c)

Figure 2.1: The construction of a crystal structure shown in (c) from the lattice in (a) and the basis in (b). The primitive vectors of the unit cell can be seen in (a).

numbers to integers with the same ratios, one obtains the *Miller indices* of the plane.

These concepts are fundamental to understanding crystalline materials, and both mechanical and electrical effects rely to a large extent on the crystal structure of a material.

2.2 Electronic Characteristics

2.2.1 Energy Bands

This section is based on the textbooks by Kittel [7], Hemmer [8] and Streetman [9].

The electronic characteristics of a material can be deduced by viewing the crystal structure and the electronic properties of the atoms in the material. For a single atom, the characteristics are derived by solving the *Schrödinger equation* for the valence electrons of the atom in question and finding the corresponding energy eigenvalues. With crystals consisting of $\sim 10^{23}$atoms, it is evident that certain simplifications are necessary. At the center of every solution to the electronic characteristics of a crystal there is a periodic potential set up by the atoms centered at each lattice point.

In the nearly free electron model, the periodic potential, $U(\mathbf{r}+\mathbf{R}) = U(\mathbf{r})$, is considered as a small perturbation of a free electron gas present in the material [8]. The Schrödinger equation for one electron in the electron gas looks like:

$$H\psi(\mathbf{r}) = \left[-\frac{\hbar^2}{2m}\nabla^2 + U(\mathbf{r})\right]\psi(\mathbf{r}) = E\psi(\mathbf{r}) \tag{2.1}$$

where $\psi(\mathbf{r})$ is the wave function of an electron in the periodic potential and m is the mass of the electron. This equation has the solution

$$\psi_{\mathbf{k}}(\mathbf{r}) = \mathrm{e}^{i\mathbf{kr}}u_{\mathbf{k}}(\mathbf{r}) \tag{2.2}$$

where $\mathbf{k}$ is an arbitrary wavevector and $u_{\mathbf{k}}(\mathbf{r})$ has the same periodicity as the potential:

$$u_{\mathbf{k}}(\mathbf{r}+\mathbf{R}) = u_{\mathbf{k}}(\mathbf{r}) \tag{2.3}$$

The type of functions shown in equation 2.2 are known as *Bloch functions* after Felix Bloch who introduced them in 1928 [10]. The energy eigenvalues, $E(\mathbf{k})$, are dependent of the wavevector, $\mathbf{k}$, and give rise to energies which electrons with a certain wavevector are allowed to occupy

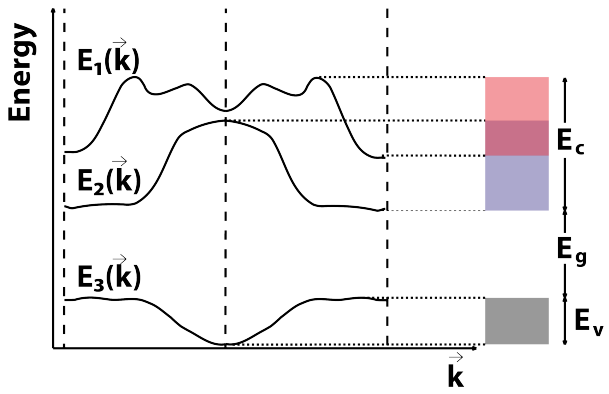

Figure 2.2: An arbitrary (E, **k**) relationship showing that the energy ranges which the electron eigenvalues sweep correspond to energy bands. Figure adapted from Hemmer [8].

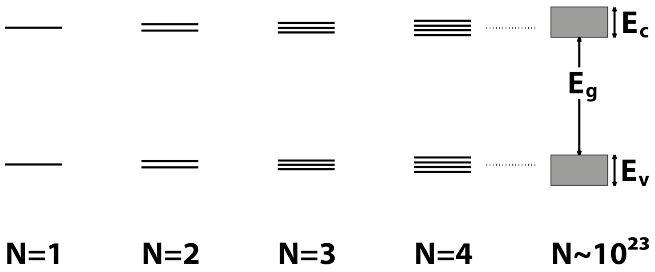

Figure 2.3: A crystal built one atom at a time will have a development of the energy levels of electrons as illustrated, if a Linear Combination of Atomic Orbitals interpretation is used. From this consideration, energy bands also emerge. Figure adapted from Hemmer [8].

(figure 2.2). The energies which electrons are allowed to occupy sweep over a certain range, and these allowed energy regions are termed *energy bands*. If the bands are separated, forbidden energy regions called *band gaps* appear.

The same result can be obtained by considering the crystal as a linear combination of the atomic orbitals (LCAO). As seen in figure 2.3 , the discrete energy levels multiply as more and more atoms are added to the crystal, and eventually the energy levels are so closely spaced that they can be considered as continuous bands of energy that the electrons can occupy. In this approach also, the electrons are confined to certain bands which they can occupy and band gaps where no electron states are present (forbidden regions).

Electrons in a material will seek to minimize their energy, and in the ground state the electrons thusly occupy the lowest possible energy configuration. The band highest in energy containing electrons is the *valence band* (cf. the valence electrons known from basic chemistry) while the band lowest in energy devoid of electrons is the *conduction band* since electrons which conduct current move in this band. Depending on the energy landscape and occupancy of the valence band and the conduction band, the material can be categorized as a metal, a semiconductor or an insulator.

For conduction of current to occur, the electrons in the material must be able to be accelerated by an electric field. They therefore need to have available energy states which to move

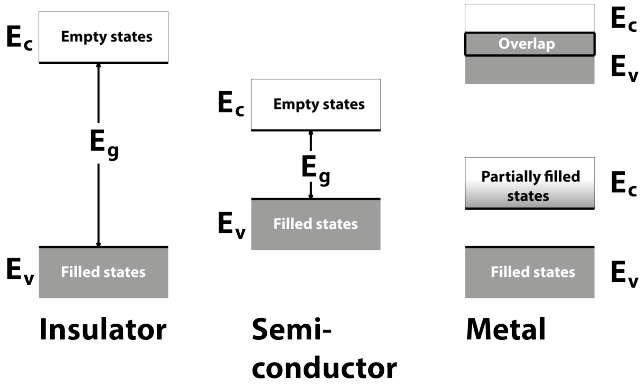

Figure 2.4: A crystalline material can be divided into an insulator, semiconductor or a metal depending on the band structure. An insulator has a large band gap and no charge carriers, a semiconductor has a low band gap below ~ 5 eV and a relatively low number of charge carriers, while a metal has no band gap and a high number of charge carriers. Figure adapted from Streetman [9].

in to. If the valence band is not completely filled or if it overlaps with the conduction band, there are energy states readily available for electrons through a miniscule thermal excitation (the thermal energy of the electrons even at temperatures close to 0 K gives a large enough excitation). Such materials can thusly conduct current easily and are known as metals. If the valence band is completely filled, there is a band gap, E_g, between the valence band and the conduction band, and no energy states are present in the band gap, electrons need to raise their energy across E_g to be free to move. Depending on how large E_g is, the material can be categorized as a semiconductor or an insulator. A semiconductor has a low E_g ($<$5 eV) and can conduct current at relatively low excitations (e.g. optical excitations at normal light intensities and energies or thermal excitations at or above room temperature), while an insulator has a high E_g ($>$5 eV) and does not conduct an appreciable amount of current at practical excitations (figure 2.4).

Semiconductors can further be divided into direct or indirect band gap materials. Viewing figure 2.5 it is evident that the band gap corresponds to the difference between the minimum of the conduction band, E_c, and the maximum of the valence band, E_v. If these do not occur for the same wavevector, a change in momentum ($\mathbf{p} = \hbar\mathbf{k}$) is required if the smallest possible energy transition from E_v to E_c is to occur. If the excitation in the transition is due to light, then the change in momentum must come from a phonon since a photon carries negligible momentum. The transition then becomes a two step process involving three particles (an electron, a phonon and a photon), and is less likely than a transition involving only an electron and a photon. A semiconductor where a change in $\mathbf{k}$ is required is known as an indirect semiconductor, while in a direct semiconductor, no change in momentum is necessary.

2.2.2 Charge Carriers and Charge Carrier Generation

For current to flow in a semiconductor, electrons must be excited across E_g to the conduction band, and when an electron leaves the valence band, an electron vacancy is left behind. This vacancy can be treated as a particle similar to an electron but with a positive charge and is commonly known as a *hole*. A hole will move in the opposite direction of an electron in an

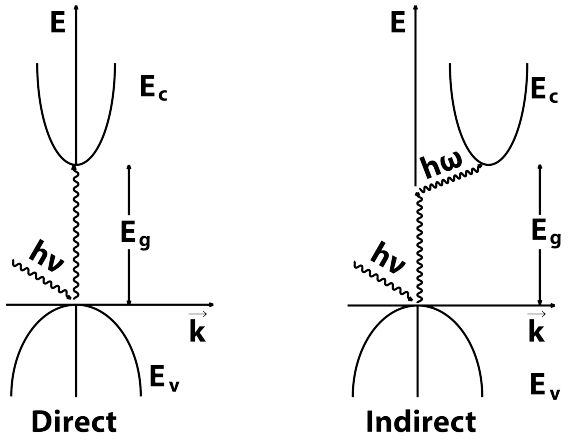

Figure 2.5: A direct band gap semiconductor requires only an energy change to excite an electron from E_v to E_c, but an indirect semiconductor demands a change in wavevector, $\mathbf{k}$, also. This change in $\mathbf{k}$ is usually assisted by the absorption or emission of a phonon.

electric field and like air bubbles in a bottle full of water, holes move in the valence band where the electron states are filled. Bubbles move to the top of the bottle, and holes also move to the top of the valence band to minimise their energy.

When holes and electrons move through a material, they are influenced by the periodic potential from the lattice and they do not move freely. The influence from the potential is contained in the curvature of the energy bands, $\frac{\mathrm{d}^2 E}{\mathrm{d}\mathbf{k}^2}$, and is usually included in a modified mass for electrons and holes known as the *effective mass*, m^*:

$$m^* = \frac{\hbar^2}{\frac{\mathrm{d}^2 E}{\mathrm{d}\mathbf{k}^2}} \tag{2.4}$$

By using the effective mass, the influence of the lattice on electrons and holes are taken into account and the equations in electrodynamics still remain valid. Electrons and holes transported through a material are usually located near the bottom of the conduction band or the top of the valence band where most bands are close to parabolic, and the effective mass is then constant.

Electrons contributing to the conduction of current through a material are located in the conduction band, but at 0 K all electrons are located in the valence band. Electrons must therefore be raised across the band gap by some sort of excitation (e.g. through thermal vibrations or illumination). In a perfect material without impurities or defects, an electron raised to the conduction band must be accompanied by a hole generated in the valence band, and an *electron-hole pair* (EHP) is formed. Such a material is known as an *intrinsic* material, and the electron density equals the hole density. The density of EHPs in an intrinsic semiconductor is dependent on the magnitude of the band gap and the temperature. The concentration of electrons and holes may be raised by introducing impurities in the material. In contrast to an intrinsic material, a material where impurities are intentionally introduced is known as an *extrinsic* material.

Consider a Si lattice where a Phosphorous atom substitutes for a Si atom at a lattice site as seen in figure 2.6. P has five valence electrons, and four of them will form bonds with the neighbouring Si atoms while the last electron is loosely bound to the P atom through Coulom-

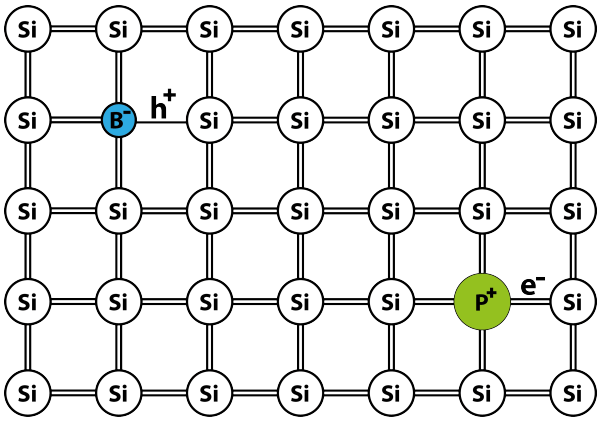

Figure 2.6: In a process called donor doping, a P atom substitutes a Si atom and donates an electron to the lattice. When B is the substituent, a hole is created, and this process is known as acceptor doping.

bic binding. This electron can easily be released from the Coulomb interaction with the P ion and donated to the lattice. Phosphorous is thus called a *donor*, and the process of introducing impurities into the Si lattice is termed *doping*. In terms of the energy band explanation of the lattice, a Phosphorous atom on a Silicon lattice site will introduce an energy level occupied by an electron close to the conduction band inside the forbidden band gap. The electron is easily excited into the conduction band where it is free to move and conduct current. If a instead Boron atom is introduced on a Si lattice site, as in figure 2.6, there are too few electrons present to complete all the bonds to the Si-atoms surrounding B (since Boron only has three valence electrons) and an incomplete bond is introduced. Electrons on a nearby atom may fill the incomplete bond and thus transfer the electron vacancy to a new bond. This can be viewed as a hole moving through the lattice, and when B substitutes Si in the lattice, a hole is introduced which is loosely bound to the B atom and can be released by a small excitation in the same way an electron was for the Phosphorous atom. In the energy band interpretation, Boron introduces an empty electron energy level close to the valence band inside the forbidden band gap, and an electron is easily excited from the valence band into the level leaving behind a hole in the valence band (or equivalently, a hole is excited from the Boron level into the valence band). Boron accepts an electron from the lattice, and it is therefore labelled as an *acceptor*.

Impurities can be introduced in large concentrations, and an impurity density of $10^{20} cm^{-3}$ is not unusual. A semiconductor with a larger concentration of acceptors than donors is known as a p-type semiconductor, while a material with an overweight of donors is known as an n-type semiconductor.

2.2.3 Charge Carrier Density

When the density of charge carriers in a semiconductor is to be quantified, information on both the energy states which the electrons can occupy and the distribution of electrons as a function of energy is required.

The energy distribution of electrons must obey the indistinguishability of electrons, the wave nature of electrons and the Pauli exclusion principle (that two electrons can not have

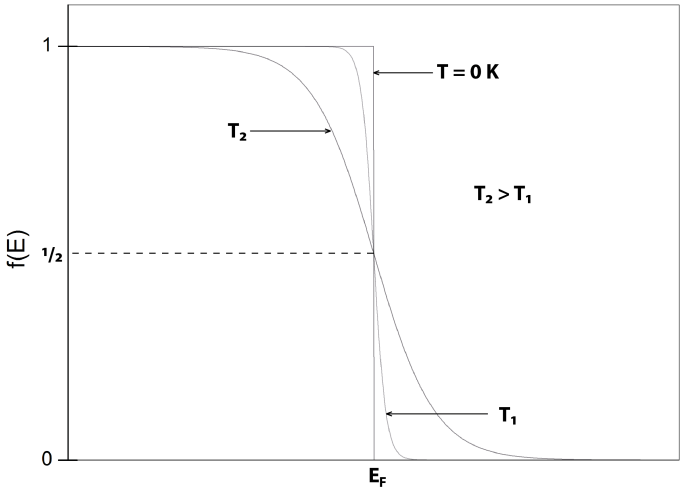

Figure 2.7: The Fermi-Dirac distribution function. At $T = 0K$, the function is a step function, while at higher temperatures the step gets smeared out.

the same quantum number). These considerations lead to the *Fermi-Dirac distribution* for electrons

$$f(E) = \frac{1}{1 + \mathrm{e}^{(E-E_F)/kT}} \tag{2.5}$$

where E is the energy, k is Boltzmann's constant ($1.38 \times 10^{-23} J/K$), T is the temperature in Kelvin and E_F is the *Fermi energy* or *Fermi level* and f(E) is the *Fermi-Dirac distribution function*. f(E) states the probability that an energy state at energy E is occupied at a given temperature, while E_F is the energy where the probability of occupancy is $\frac{1}{2}$. The distribution function is shown in figure 2.7. At 0 K, the function is step like where no states above E_F are occupied while all states below E_F are occupied. When the temperature is increased, the step is smeared out, and there is a finite probability of finding an electron at an energy $E > E_F$. The distribution is also symmetric, and the probability of finding an electron at an energy $E_F + \Delta E$ is equal to the probability of not finding an electron at $E_F - \Delta E$. Equation 2.5 is given for electrons, but the distribution function for holes is easily found through the realisation that a hole is the absence of an electron and the distribution function for holes is then $1 - f(E)$, since this will give the probability that a state is empty. If the Fermi-Dirac distribution function is combined with the density of energy states, $N(E)$, the density of electrons, n, in the conduction band can be found from

$$n = \int_{E_c}^{\infty} f(E)N(E)\mathrm{d}E \tag{2.6}$$

and the density of holes, p, is

$$p = \int_{-\infty}^{E_v} [1 - f(E)]N(E)\mathrm{d}E \tag{2.7}$$

The result of the integrations of equations 2.6 and 2.7 can be compressed into an effective density of states for electrons, N_c, and holes, N_v, at the band edges times the probability of electron occupancy, $f(E_c)$, and hole occupancy, $1 - f(E_v)$, at the band edges.

$$\begin{aligned} n =& N_c f(E_c) \\ p =& N_v[1 - f(E_v)] \end{aligned} \tag{2.8}$$

If E_F is assumed to be several kT below E_c, $f(E_c)$ can be approximated to

$$f(E_c) = \frac{1}{1 + \mathrm{e}^{(E_c - E_F)/kT}} \approx \mathrm{e}^{-(E_c - E_F)/kT} \tag{2.9}$$

Similarly, if E_F is assumed to be several kT above E_v, $1 - f(E_v)$ can be approximated to

$$1 - f(E_v) = 1 - \frac{1}{1 + \mathrm{e}^{(E_v - E_F)(kT}} \approx \mathrm{e}^{-(E_F - E_v)/kT} \tag{2.10}$$

and equation 2.8 becomes

$$\begin{aligned} n =& N_c \mathrm{e}^{-(E_c - E_F)/kT} \\ p =& N_v \mathrm{e}^{-(E_F - E_v)/kT} \end{aligned} \tag{2.11}$$

When considering an intrinsic semiconductor, the hole density equals the electron density:

$$n = p = n_i \tag{2.12}$$

where n_i is the intrinsic carrier density. This means that

$$np = n_i^2 \tag{2.13}$$

Combining equations 2.13 and 2.11 to

$$n_i = \sqrt{np} = \sqrt{N_c N_v}\mathrm{e}^{-(E_c - E_v)/2kT} = \sqrt{N_c N_v}\mathrm{e}^{-E_g/2kT} \tag{2.14}$$

it is clear that the intrinsic density of carriers will only depend on inherent properties of the material (such as E_g and the effective density of states) and the temperature. The product np is also independent of the Fermi level position in the material and is constant at a given temperature. For Si with a band gap of 1.11 eV, the electron concentration at room temperature is $1.5{\times}10^{-3}\mathrm{cm}^{-3}$ [9].

An extrinsic semiconductor is a material where impurities have been introduced in order to increase the carrier density. Commonly introduced donors and acceptors have energy levels which lie close to the band edges, and they are therefore easily ionised. At room temperature it is thus usually assumed that all the dopants are ionised and that they have donated holes or electrons to the valence or conduction band, respectively. If the occupancy of the conduction band or the valence band in the semiconductor is changed, the energy distribution of electrons in the material has changed and this implies that the distribution function, $f(E)$, has changed. This modification to the function changes the position of E_F in the material. If a donor is introduced, more electrons are present in the conduction band, and E_F approaches E_c, while if an acceptor is introduced, less electrons are present in the valence band and E_F moves closer

to E_v. The electron density in an n-type doped semiconductor at room temperature is hence considered to be equal to the doping density:

$$n \approx N_d \tag{2.15}$$

By combining 2.15 and 2.13, the hole density (or the *minority carrier density* since holes are the minority carriers) in a n-type doped material (n-type material) is

$$p \approx \frac{n_i^2}{N_d} \tag{2.16}$$

The donor density can be quite high, and with $N_d = 10^{16} cm^{-3}$ the hole density is as low as $10^4 cm^{-3}$. Similarly, the hole density is high when the material is p-type doped and the electron density (the minority carrier density) is correspondingly low:

$$\begin{aligned} p &\approx N_a \\ n &\approx \frac{n_i^2}{N_a} \end{aligned} \tag{2.17}$$

When the doping density is very high, the density of donor states leads to a delocalisation of the carrier energy levels, and a band of filled carrier states is formed close to the band edge. Semiconductors with such a high doping density behave like metals since their conductivity does not show a temperature dependence, and they are known as degenerate semiconductors.

2.3 Zinc Oxide

In this section, some basic structural and electrical properties of Zinc Oxide are introduced. The section is based on the reviews by Özgür et al. [11] and Pearton et al. [12] as well as other references specified in the text.

2.3.1 Material Properties

Zinc Oxide (ZnO) is a group II-VI binary compound semiconductor, crystallising at ambient conditions in the hexagonal *wurtzite structure* where each oxygen ion is surrounded by four Zn ions in a tetrahedron configuration, as seen in figure 2.8. The hexagonal unit cell of the wurtzite structure is described by the three lattice parameters a, b and c. Numerous studies [11] have been made to determine the lattice constants of ZnO, and in this work the lattice parameters $a = b = 3.2495 \pm (0.00002)$Å and $c = 5.2069 \pm (0.0001)$Å as determined by Heller et al. [13] are used.

ZnO is a wide band gap semiconductor with a direct band gap of ~ 3.4 eV at room temperature [12]. It is commonly n-type and notoriously difficult to dope p-type, and much effort has been made in order to establish which defects are the cause of this n-type conductivity. With regards to native defects in the material, oxygen vacancies (V_O) zinc interstitials (Zn_i) and zinc antisites (Zn_O) may all act as donors. However, investigations of these defects both experimentally and through simulations have shown that none of them are likely to contribute significantly to the n-type behaviour of ZnO. Oxygen vacancies is reported to have a low formation energy [14, 15], something which is supported by experimental studies showing rather high concentrations of V_O ($\sim 10^{17} cm^{-3}$) [16]. This low formation energy is contested [17],

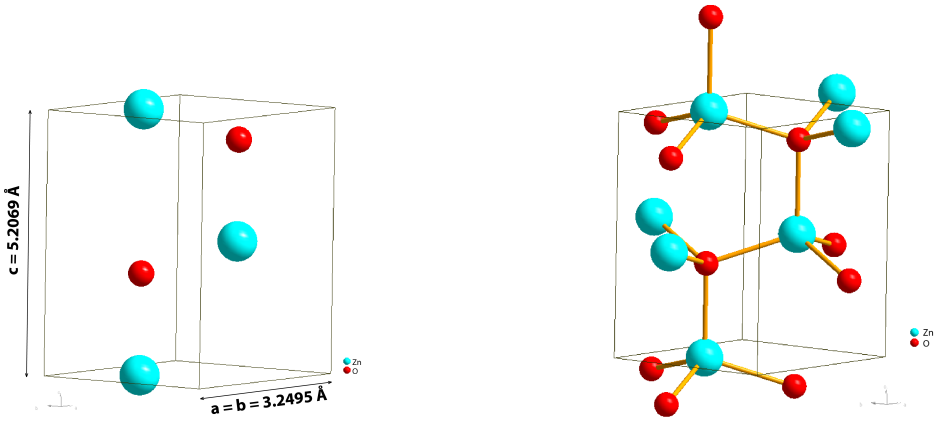

(a) (b)

Figure 2.8: The structure of ZnO. In (a), the unit cell and the lattice constants are shown while in (b) bonds and more atoms are added to show the tetrahedron configuration of the structure. The visualisation was created using the Diamond software (Diamond - Crystal and Molecular Structure Visualization, Crystal Impact - Dr. H. Putz & Dr. K. Brandenburg GbR, Kreuzherrenstr. 102, 53227 Bonn, Germany, http://www.crystalimpact.com/diamond).

but the oxygen vacancy nevertheless has a deep donor level [18, 19] and should not contribute significantly to the n-type conductivity at room temperature. Zinc interstitials are expected to have a shallow donor levels in the band gap [17, 20], but their high formation energy [17, 21] will lead to a too low concentration for providing appreciable donor activity. The formation energy of Zn_i decreases with decreasing Fermi level position suggesting that the defect may be acting as a compensating defect for p-type behaviour. The zinc antisite is also not likely to provide the n-type behaviour. Although it is a shallow donor, it has a high formation energy [21, 22]. As the intrinsic defects fail to explain the n-type conductivity, attention has turned to unintentional doping during crystal growth. In particular, hydrogen is suspected as a possible culprit for n-type ZnO [23, 24] as it is present in all ZnO growth methods, has a low formation energy and a shallow donor state.

N-type doping of ZnO is also achieved with the addition of group III elements such as Al, Ga and In [12]. Si has also proven to be an effective n-type dopant in ZnO [25, 26]. p-type ZnO is not easily achieved and much effort is put into finding suitable acceptors with the most promising candidate to date appearing to be Nitrogen [27, 28]. P-type doping of ZnO will be further discussed in section 2.3.3.

2.3.2 Transparent Conductive Oxide

One application of ZnO is as a *Transparent Conductive Oxide* (TCO). TCOs are used in opto-electronic devices such as flat panel displays and photovoltaic cells where they provide a low resistive contact to the external circuit. In conventional photovoltaic cells, the front contact of the cell is usually thin contact fingers. To lower the resistance of the contacts, a conductive thin film is deposited on top of the photovoltaic cell. TCOs are mostly used in thin film solar cells such as CIGS cells, but there are also examples of TCOs being employed in crystalline photovoltaic cell configurations. The Sanyo HIT cell is such an example [29]. With the HIT

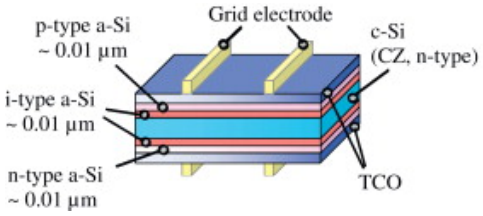

Figure 2.9: The structure of the Sanyo HIT cell showing that a TCO is an integral part of the cell. The image is adapted from Mishima et al. [30].

structure as shown in figure 2.9 Sanyo has reached an efficiency of 23% [30]. Due to their applications, TCOs need to be low resistive and highly transmittive in the visible range. As a result of these requirements, wide band gap, degenerate polycrystalline or amorphous semiconductors are chosen since these transmit most of the sub-band gap light and can exhibit quite high carrier concentrations. Relevant materials should have band gaps of above 3 eV and a resistivity on the order of $10^{-3}\Omega$cm or less which translates to a carrier concentration of around $10^{20}cm^{-3}$ [31]. This narrows the possible number of materials suitable for this application to a few, and presently Tin Oxide, SnO_2, Indium Oxide, I_2O_3, Indium Tin Oxide (ITO) and Zinc Oxide are mostly used. ITO has superior properties with respect to conductivity, but the scarce mineral deposits of Indium [6] is a problem in keeping cost of ITO low. ZnO does not face the problem of low mineral deposits and is much cheaper, but it does not show the same low resistivity as ITO [31]. However, by doping ZnO heavily with Al (AZO), resistivities of $1.3\times10^{-4}\Omega$cm [32] have been achieved and this is comparable to the values for ITO [33]. Si has also has proven to be an effective dopant in ZnO reaching resistivities of $3.8\times10^{-4}\Omega$cm [25]. With transmittance of both materials around 90% in the visible range, ZnO is proven to be a viable alternative for replacing ITO as a TCO.

2.3.3 P-type ZnO

ZnO is not only a promising material as TCOs, but also for piezoelectric transducers and varistors. However, several other interesting devices have not been realised since few pn homojunctions[1] have been reported [34]. If stable and low resistive p-type doping could be achieved in ZnO, useful devices such as UV Light Emitting Diodes (LEDs) and UV Lasers could be made. However, p-type doping in ZnO is a difficult task and few reports of resistivities below 1Ωcm exist [34].

One possible way of realising p-type doping would be through the intrinsic acceptor type defects in ZnO (O_i and V_{Zn}), but these have high formation energies [35] and would also be compensated by the corresponding intrinsic donors discussed in section 2.3.1. Extrinsic doping of ZnO is thus needed in order to achieve p-type doping. The most common extrinsic acceptor doping in ZnO to date is Nitrogen with the first reports of p-type doping in 1997 [36]. Nitrogen doping has also been attempted without successfully achieving p-type films [37], and formation of N-N complexes acting as compensating centers has been proposed as an explanation for the lack of p-type conductivity [38,39]. Yet other attempts with Nitrogen have

[1] A pn-junction is a junction where one side of the junction is n-type while the other side is p-type. Such a system exhibits rectifying behaviour which is utilised in numerous electronic devices. In a homojunction, both sides consist of the same material (albeit with different doping) while in a heterojunction, the p-side and n-side are of different materials.

been done by applying a co-doping method where both a donor and Nitrogen as an acceptor were introduced [40, 41]. The donor is proposed to assist and activate the acceptors [42] but the exact role of the donor is disputed [38]. Another approach is increasing the p-type conductivity by so-called cluster doping [43, 44]. Other group V dopants have also been tried and low resistivities were potentially achieved by Phosphorous doping and subsequent annealing [45].

Group I dopants such as Li, Na and K introduce shallow acceptor levels in ZnO when they substitute for Zn, but by interstitial positioning of Li and Na (Li_i, Na_i) and through K promoting formation of oxygen vacancies, the acceptor action of these dopants is efficiently killed [27].

P-type doping of ZnO thus seems most likely to succeed using N or P as an acceptor, possibly by utilising donors aiding the activation/formation of the acceptor.

2.4 Previous Work

2.4.1 Si Nanocrystals in a ZnO Matrix

This thesis was initially built around Si doping of ZnO with the aim of producing Si nanocrystals in a ZnO matrix. Si nanocrystals prepared from a colloidal solution have previously exhibited multiple exciton generation (MEG) [46]. In this process, two electrons are created from one energetic photon since the quantum confinement of the nanocrystal makes MEG competitive over other relaxation processes [47]. These two electrons could then be extracted from the nanocrystal, or be allowed to relax thus creating two photons with a lower energy than the original, incident photon. The ZnO with embedded Si nanocrystals could therefore act as a down-converting material (converting blue light to red light). Since the normal active layer in a solar cell is Si with a band gap of 1.11 eV, blue light will produce electrons which will lose a large part of their energ to thermalisation. Down-converting the blue light to red light would therefore make a Si solar cell more efficient. Reports by Lai et al. [48] and Schofield [49] suggest that by increasing the Si content above the solid solubility limit of Si in ZnO, nanocrystals will precipitate. Both reports utilise co-sputtering of ZnO and Si to produce such nanocrystals, and XRD and High Resolution Transmission Electron Microscopy (HRTEM) among other techniques were used to identify the presence of Si nanocrystals. A summary of the results from [48] is presented in figure 2.10. The presence of Si nanocrystals is supported through results obtained with XRD, HRTEM, Fourier Transform Infrared Spectroscopy (FTIR), Energy-Dispersive X-Ray Spectroscopy (EDS) as shown in figure 2.10 and PL (not shown). The authors are able to control the diameter of the nanocrystals (determined by HRTEM) by changing the power on the target electrodes (hence changing the amount of Si in the films) and the crystals show quantum confinement as evidenced by PL. The density of the nanocrystals is also determined through HRTEM micrographs, and is seen to be rather constant up to a Si content of 24.9% where a sharp decrease occurs. This decrease is attributed to formation of Si-O bonds instead of Si-Si. The evidence of Si nanocrystals seems compelling, but there appears to be a discrepancy between the size of the crystals as determined by HRTEM and the XRD spectrum. From the XRD spectrum, the size of small crystallites may be established through the Scherrer equation (equation 3.22). A very crude analysis based on the (111) peak of Si in the XRD data of the report yields a crystallite size of 20-30 nm, a factor 4-6 times that of the data reported from HRTEM analysis although HRTEM usually provides larger grain sizes than XRD analysis.

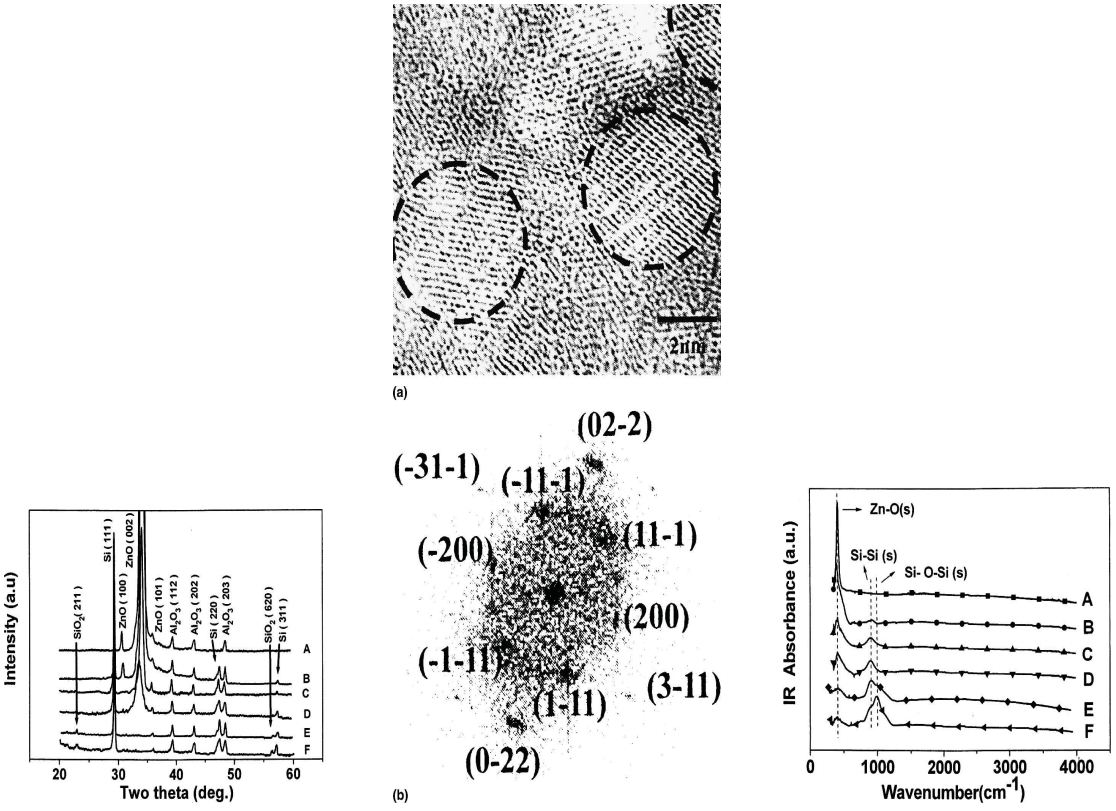

(a) (b) (c)

Figure 2.10: Selected figures from Lai et al. [48]. (a) XRD results showing the presence of an Al_2O_3-phase from the substrate, a ZnO-phase from the film and a SiO_2 and Si-phase from the Si Nanocrystals. (b) **(a)** A HRTEM micrograph of the Si nanocrystals. **(b)** An electron diffraction pattern identifying reflections from the Si nanocrystals (c) FTIR of the films, indicating that Si-Si bonds are present in the films.

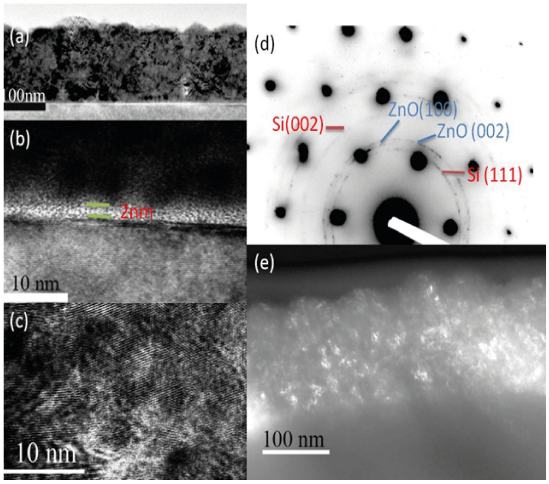

Figure 2.11: Selected figures from Schofield [49] (a) A TEM micrograph of a crossection of a ZnO:Si film. (b) A higher resolution image of the interface between the substrate and the film showing a SiO_2 layer. (c) HRTEM micrograph of the film showing Si nanocrystals. (d) SAED pattern of the film with the reflection stemming from Si indicated. (e) A dark field image of the film. The bright spots are interpreted as Si nanocrystals.

Schofield has made a similar investigation, where the sputtered films were investigated with XRD and TEM. The XRD data show no evidence of Si nanocrystals, and their presence were solely established through TEM data. Figure 2.11 shows the TEM data which the presence of Si nanocrystals were based upon. However, the interpretation of the data has been challenged by Dr. Ragnhild Sæterli who ascribed the SAED ring from Si in figure 2.11(d) to a ZnO reflection [50].

2.4.2 ZnO as a TCO

In section 2.3.2, ZnO was discussed in relation to TCO applications. ZnO is already in use as a TCO for CIGS photovoltaic cells [51], but with the improvement in electrical characteristics ZnO could replace the more expensive ITO as a TCO also in Si based photovoltaic cells. In this respect, different doping of ZnO has been attempted to lower its resistivity. ZnO doped with Ga (GZO) and Al (AZO) have exhibited resistivities close to and below $1\times10^{-4}\Omega$cm [32, 52] and are along with Indium doped ZnO the most common ways to achieve n-type doping of ZnO [12]. Magnetron sputtering of doped ZnO has been employed with success reaching resistivities of $\sim 2\times10^{-4}\Omega$cm [53]. However, in a review by Ellmer [53], it is postulated that ZnO will not reach resistivities below $\sim 1\times10^{-4}\Omega$cm as the mobility in ZnO has an upper limit of 40 $cm^2V^{-1}s^{-1}$ at high doping concentrations, due to ionized impurity scattering and a limit to the maximum carrier density of $1.5\times10^{22}cm^{-3}$. The lower limit of resisitivity proposed by Ellmer was surpassed by Park et al. [52], through breaking the limit of carrier density, though the limit of mobility was not transcended.

Al, Ga and In are not the only dopants which have successfully been introduced in ZnO to achieve low resistive n-type films. B, Y, Sc, Ge, Ti, Zr, Hf and F doping of ZnO have all reached resistivities on the order of $10^{-4}\Omega$cm [54], and since not all of these species may donate an electron, it is suggested that they promote the formation of oxygen vacancies which supply the donor action [53]. Silicon has also proven to be an effective donor in ZnO [25,26] exhibiting

resistivites around $5\times10^{-4}\Omega$cm with carrier densities of $10^{20}-10^{21}\text{cm}^{-3}$ and mobilities of $\sim$ 10 $\text{cm}^2\text{V}^{-1}\text{s}^{-1}$.

2.4.3 Annealing of ZnO

The electrical and crystal characteristics of ZnO is greatly affected by the annealing ambient. It is commonly found that annealing a polycrystalline ZnO film in air will lead to a higher crystallinity of the films as the atoms can settle into energetically more favourable positions as they gain higher mobilities at higher temperatures [55, 56], although there have also been reports of lower crystallinity with annealing [57]. Furthermore, annealing in air will also lead to a significant increase in resistivity [58, 59]. It is suggested that this increase is due to a chemisorption of oxygen at grain boundaries which increases the number of trap states [56,60]. A different explanation assumes that formation of the compensating, intrinsic acceptors O_i or V_{Zn} reduces the net carrier density [61]. When annealing in hydrogen [58] or forming gas (95% N_2, 5% H_2) [56], the opposite effect is observed with a decrease in resistivity due to desorption of oxygen at the grain boundaries [56] in addition to creation of oxygen vacancies [59]. However, as discussed in section 2.3.1, the oxygen vacancy has a deep donor level, and does not support the explanation of Tong et al. [59].

There have also been reports of a change in conductivity from n-type to p-type when films have been annealed in NH_3 [62] and air [63]. To et al. [63] prepared ZnO films doped with As by RF magnetron sputtering, and explained the change in conductivity with the formation of the $As_{Zn}(V_{Zn})_2$ complex which acts as a shallow acceptor [64]. Garces et al. showed that when annealing in air or N_2, Nitrogen is incorporated as an acceptor in ZnO [28], and a change in conductivity with annealing in air could be related to this effect.

Chapter 3

Experimental Methods

This thesis has a strong focus on experimental work, and several different experimental techniques have been utilised. The samples have been prepared by magnetron sputtering, and the theory behind this technique is presented in section 3.1. The samples have subsequently been characterised using several different techniques, and the theory behind Hall Effect measurements (section 3.2), X-ray Diffraction (section 3.3), Transmittance measurements (section 3.4), Atomic Force Microscopy (section 3.5), Transmission Electron Microscopy (section 3.6), Photoluminescence Spectroscopy (section 3.7), Rutherford Backscattering Spectrometry (section 3.8) and Stylus Profilometry (section 3.9) is introduced in the following pages.

3.1 Sputtering

This section is based on the textbook by Campbell [65] and the papers by Ellmer [66], Thornton [67], Bräuer et al. [68] and Sigmund [69]

Sputtering is a phenomenon that can be used for many applications including non-selective etching of surfaces, analysis of material composition and thin film deposition, and it is widely used in the industry for thin film deposition.

An inert gas is let into a chamber which is evacuated (for the rest of the discussion, Ar is assumed to be the inert gas). This gas will contain a small concentration of electrons and ions provided either intrinsically in the gas or from an igniter, and by applying a voltage difference in the chamber (produced by a *cathode* and an *anode*), the electrons and ions will be accelerated. The ions will be accelerated towards the negative cathode where the *target* (i.e. the material to be sputtered) is placed. The ions will then bombard the target releasing atoms and secondary electrons. The electrons on the other hand will be accelerated towards the positively charged anode and as they penetrate through the plasma, they will collide with neutral inert gas atoms and ionize them. These ions will then be accelerated towards the cathode where they will create more secondary electrons which in turn will create more ions. It is thus a self-sustaining process as long as the voltage is high enough to accelerate the electrons and ions sufficiently. The atoms emitted from the target may penetrate across the chamber due to the low pressure and the momenta received from incident ions, and will thus be deposited on the surface of the substrate (which is connected to the anode).

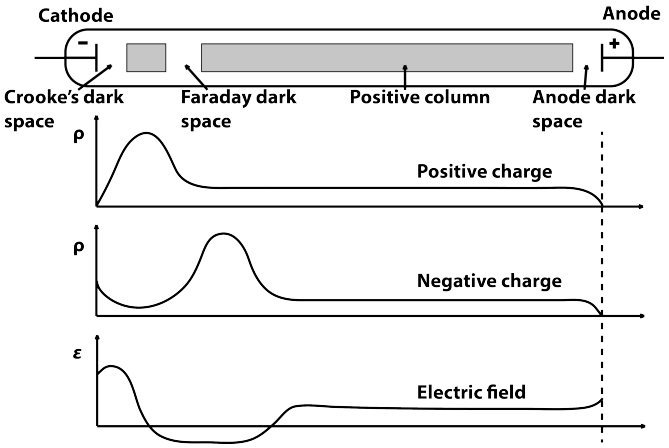

Figure 3.1: At the top, the structure of a dc plasma is shown, while the positive and negative charge densities in the plasma and the electric field is shown in the graphs below. Figure adapted from Campbell [65].

3.1.1 Plasma Characteristics

The plasma formed in the chamber exhibits many traits which are important for the sputtering action. To illustrate the plasma characteristics, let us follow an electron on its way from the cathode to the anode. When Ar^+-ions strike the surface of the cathode (target), secondary electrons are emitted. Due to the negative charge on the cathode, the electrons are quickly accelerated away from the target. The cathode also works as a sink for positive ions, thus near the cathode, the plasma has no charge. As electrons are accelerated away from the target, they gain energy and eventually obtain enough energy to excite the neutral Argon atoms creating a glow in the plasma. At even higher electron energies, the electrons may ionize the neutral Argon atoms creating Ar^+-ions. This creates a build-up of positive charge near the cathode, and the positive charge shields the rest of the plasma from the negative charge on the cathode reducing the electric field (figure 3.1). More and more electrons will at this point in the plasma have collided with Ar-atoms and because of the reduced field, they will not gain enough energy to ionize appreciable amounts of Ar-atoms. This leads to a drop in the positive charge to a constant background value throughout the remainder of the plasma. The anode will act as a sink for electrons due to the positive charge, and Ar^+-ions are repelled giving little charge in the plasma near the anode. The charge densities in the plasma are shown in figure 3.1

The energies of the electrons in the plasma will decide which collision mechanisms are predominant at a given position in the plasma. Electrons with energies greater than 15 eV will primarily ionize the neutral Ar-atoms, hence, just beyond the positive charge spike there will be a dark space, termed *Faraday dark space*, as most electrons with high energies (electrons which have not yet collided with Ar-atoms) will only ionize the atoms while the electrons with low energies (electrons which already have collided and lost their energies or electrons created from ionizing collisions) do not have enough energy to excite the atoms. In addition to the Faraday dark space, there will be a dark space near the anode, termed Anode dark space, since there is very little charge due to the anode being a sink for electrons, and a dark space near the cathode, termed *Crooke's dark space*. Crooke's dark space will have a quite high concentration of electrons due to emitted secondary electrons from the target, but the electrons have not

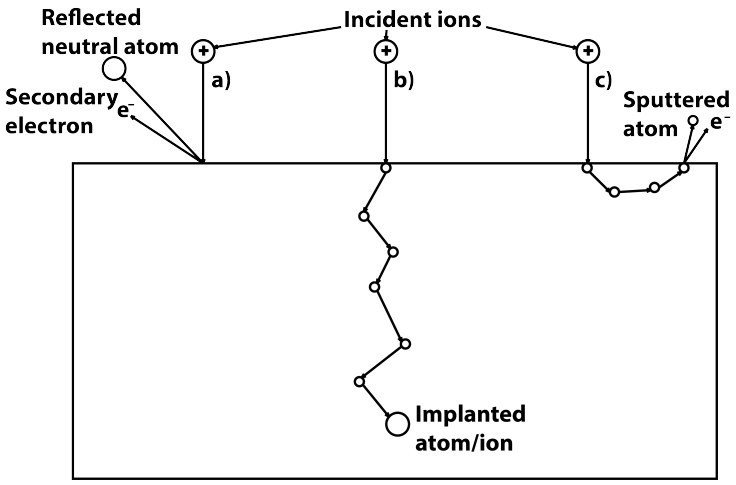

Figure 3.2: Different scenarios which can occur when an ion impinges on a solid material. a) On the left, a low energy ion is reflected at the surface picking up a neutralising electron and releasing a secondary electron from the material in the process. b) In the middle, a high energy ion is implanted into the material creating significant damage to the lattice. c) On the right, an ion with a intermediate energy mediates a sputtering event.

gained enough energy from the electric field in the plasma to excite Ar-atoms. In figure 3.1, the position of the dark spaces are indicated.

It is in Crooke's dark space that the critical process in a sputtering system occurs. In Crooke's dark space, there is a large electrical field due to the small separation of the negative charge on the cathode and the positive charge spike in the plasma on the edge of Crooke's dark space. This large electric field will accelerate Ar^+-ions towards the target and depending on the energy of the incoming ions, several different scenarios may occur, one them being a sputtering event.

3.1.2 Ion Bombardment

The target situated on top of the cathode will be bombarded by ions since Crooke's dark space provides a large electric field. Depending on the voltage applied to the cathode, the distance the ions travel and the pressure inside the chamber, the ions striking the surface will have varying energies. Ions colliding with the target will only remove target atoms if the energy of the incoming ions are of the correct magnitude. At energies of 10s of eV, the ions will be reflected off the surface without removing any target atoms, possibly with an electron transfer from the target neutralizing the inert gas ion as seen on the left of figure 3.2. With a sufficiently low energy ($E \leq 10$ eV), the ions may also be adsorbed to the surface. At the other end of the scale ($E \geq 10$ keV), the ion can penetrate the surface of the target and be embedded in the matrix several atomic layers into the target (ion implantation) (the middle of figure 3.2). If an ion with an energy in a range in between these two extremes ($E \sim 30 - 1000$ eV) hits the surface of the target, several large-angle collisions will occur in the first few atomic layers of the target since nuclear stopping is effective in this energy range. If an atom or ion with a velocity parallel to the surface of the target collides with an atom near the surface, this atom can be removed from the surface with a velocity normal to the surface and with an energy of about 10-50 eV (the right of figure 3.2). This atom will then travel across the

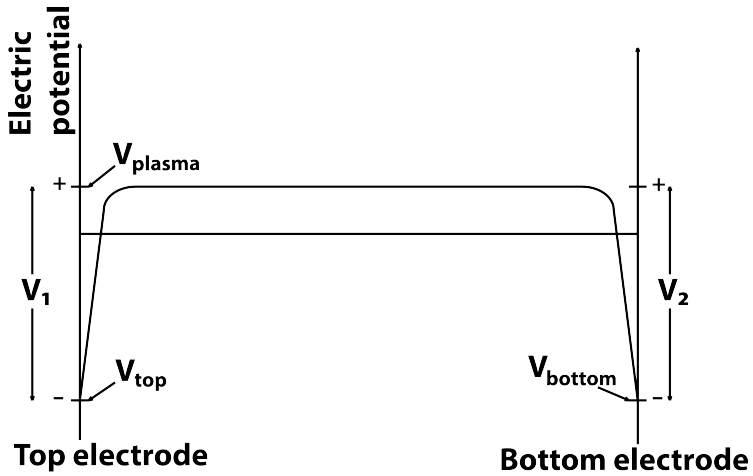

Figure 3.3: The potential in the plasma will stay constant throughout much of the glow discharge, but will experience a significant drop near the electrodes. Figure adapted from Campbell [65].

plasma and be deposited on the substrate situated on the anode.

The energy the target atoms have when they reach the substrate will determine the quality of the deposited film as more energetic atoms are more likely to find an energetically favorable location on the surface (higher surface mobility). The energy that atoms gain during sputtering is about 100 times that gained during evaporation, and this gives sputtering an advantage over evaporation in regards to crystal quality of the film. However, energetic atoms incident on the surface of the deposited material will also introduce damage to the surface if the energy of the atoms is high enough.

3.1.3 RF Sputtering

If the target is insulating, the collisions generating secondary electrons will charge the surface of the target. Similarly, if the substrate is insulating, the sink action of the anode will charge the substrate. This will eventually lead to the plasma being extinguished through a reduced electric field in the plasma. To overcome this problem with insulating materials, an ac signal is used to drive the plasma. This ac signal is in the radio frequency (RF) range, typically 13.56 MHz, and this type of sputtering is thus labelled *RF sputtering*. The electrons in the plasma can easily follow the excitations of the ac signal, and will strike both electrodes alternately giving a net negative charge on both the cathode and anode compared to the plasma. The ions in the plasma however, have a too large inertia to be able to follow the excitations and only the electrons will contribute significantly to the charging of the electrodes. Since the plasma is conductive, there will be a negligible voltage drop in the glow discharge, but near the electrodes electron depletion will lead to a significant voltage drop from the bulk of the plasma. Following the nomenclature from figure 3.3 , the voltages are labelled as:

$$\begin{aligned} V_1 &\equiv V_{plasma} - V_{top} \\ V_2 &\equiv V_{plasma} - V_{bottom} \end{aligned} \tag{3.1}$$

By changing the area of one of the electrodes, the potential differences V_1 and V_2 may differ according to

$$\frac{V_1}{V_2} = \left[\frac{A_2}{A_1}\right]^4 \tag{3.2}$$

where A_1 is the area of the top electrode and A_2 is the area of the bottom electrode. The sputtering action of a set-up relies on the voltage difference between the target and the plasma (since this decides the field where the ions are accelerated), and a large difference in area between target and substrate is thus needed. Practically, the difference in area between the two electrodes is done by connecting one of them to the walls of the chamber.

3.1.4 Magnetron Sputtering

The rate of sputtering depends on several aspects in the sputtering process, but certainly one of the most important parameters is how many ions hit the surface of the target per unit time. This is directly related to how many ions there are in the plasma all together, and by increasing the number of ions in the chamber, a higher rate can be achieved. In a regular parallel plate set-up, the ion concentration in the gas is 0.001%, and this can be increased 30 times by using different techniques. Collectively, all plasmas that are enriched in ion content are called *High Density Plasmas* and one way of obtaining a High Density Plasma is through setting up a magnetic field in the chamber, and by way of the Lorentz force,

$$\vec{F} = q\vec{v} \times \vec{B} \tag{3.3}$$

to increase the pathlength of electrons in the plasma by inducing a helical motion on the electrons. This will lead to more collisions between gas atoms and electrons, and more ions will be produced, giving a higher bombardment rate. The magnetic field is tuned in such a way that electrons will move in a circle, while the heavy ions will not be affected significantly. In *Magnetron sputtering*, the magnetic field comes from fixed bar magnets arranged in such a manner that the radius of the circle the electrons travel,

$$r = \frac{mv}{qB} \tag{3.4}$$

is less than the cathode dark space, and the electrons are contained within the dark space.

3.1.5 Deposition Rate

The *deposition rate* of a sputtering system depends on several factors, and the most important ones are:

- The ion flux impinging on the target
- The probability that an atom is ejected by an incident ion
- The transport of the atom across the plasma to the substrate

The flux of ions incident on the surface of the target will depend most importantly on the mass of the ion, the voltage difference between the target and the substrate and the thickness of the cathode dark space. In a dc plasma, the *Langmuir-Child relation* is valid [70]:

$$J_{ion} \propto \sqrt{\frac{1}{m_{ion}}} \frac{V^{3/2}}{d^2} \tag{3.5}$$

J_{ion} is the ion flux, m_{ion} is the mass of the ion, V is the voltage difference between the target and the substrate and d is the thickness of the cathode dark space.

When an ion does arrive to the surface of the target, there is a certain probability that this ion will eject a target atom, and this probability is expressed as the sputter yield.

$$S = \frac{Z_e}{Z_i} \tag{3.6}$$

where S is the *sputter yield*, Z_e is number of ejected target atoms and Z_i is number of incoming ions, and S depends on many parameters in both the target and in the plasma, notably the incident ion mass, angle and energy as well as the target crystallinity.

As an atom is ejected from the target, this atom needs to travel across the plasma to be deposited on the substrate, and this process is adequately described by computational fluid dynamics where ion diffusion and drift are taken into account. The details of such dynamics will not be elaborated on here.

The deposition rate is an important parameter to control when producing thin films. For sputtering, such control is achieved through the discharge power ($P = I|V_{top}|$ where I is the discharge current, and V_{top} is as defined in figure 3.3) which the deposition rate depends linearly on. This linearity is maintained for ion energies below the ion implantation regime ($\sim$ 750 eV).

3.1.6 Thin Film Morphology

The mechanisms governing the thin film growth and morhpology are largely decided by the surface mobility or energy of the sputtered atoms. The ejected species of the target are generally atomic or diatomic [71], and they arrive at the surface of the substrate with considerable energy. As they reach the surface, part of this energy will be used for them to adsorb, while the remaining energy is translated as surface mobility. This surface mobility will depend on the binding energy of the adatom to the surface, the kinetic energy of the incoming atom, the temperature of the substrate and of course which type of substrate. In the energy landscape of the surface, the adatoms will settle in energetic minimas, and the more surface mobility they have, the higher probability they have of reaching favorable minima (i.e. the lowest possible). This diffusion is followed by nucleation of several adatoms, and islands will form when stable nuclei are established. If the surface mobility is high, these islands will then merge and a continuous film results.

The morphology of this film depends on the mobility of the adatom, and this in turn is decided by the kinetic energy of the incoming atoms and the substrate temperature. The substrate temperature is a parameter which is relatively easy to measure and control, while the kinetic energy of the incoming atoms are harder to predict and control. However, the kinetic energy will depend on the pressure in the chamber since this effectively decides how many collisions an atom will experience on its way from the target to the substrate (and thus how much energy is lost). Hence it decides how much time an adatom can diffuse before the energetically favorable positions are taken. Thus will the substrate temperature and the chamber pressure be important parameters to control in order to obtain the desired characteristics of a thin film. The relationship between the morphology, the substrate temperature and the chamber pressure is described in the *zone model* proposed by Movchan and Demchishin [72] and modified by Thornton [67].

The model is valid for most crystallising materials, and as seen in fig 3.4 the temperature

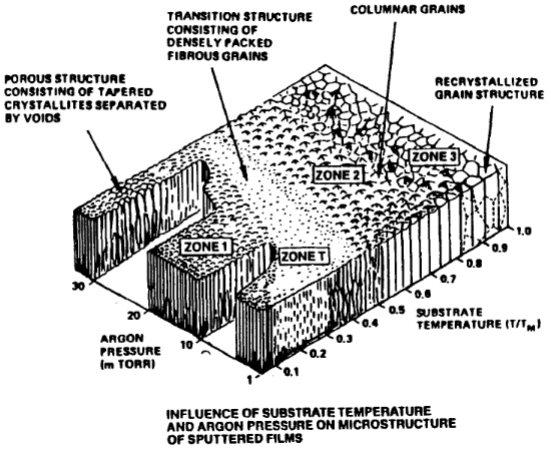

Figure 3.4: The zone model of thin film deposition. Figure taken from Thornton [67].

is normalized to the melting temperature of the film. At low temperatures and moderate pressure, the mobility of the adatoms will be low and they will not settle in the most favorable spots leading to an amorphous, porous and rough film, and this is the type of film seen in zone 1. At lower chamber pressures or at higher temperatures, the adatoms will experience a higher mobility, and the film will move into zone T. Zone T will be dominated by small grains giving a smooth surface, and it is the zone desirable for microelectronics. A further increase in temperature (into zone 2) will lead to even higher surface mobility and thus, the grain size will increase. The grains are columnar in shape, extending from the substrate towards the surface of the film. The surface in zone 2 will be quite rough compared to zone T. In zone 3 at the highest temperature and lowest pressure, the film will be dominated by large 3D grains and a rather rough surface.

Thus, the pressure inside the chamber and the substrate temperature are important parameters in order to improve the mechanical stability, surface morphology and electrical properties of the deposited film.

3.2 Hall Effect Measurements

This section is based on the textbooks by Kittel [7], Hemmer [8] and Lillestøl et al. [73].

Hall effect measurements are electrical measurements which can extract the *resistivity*, the *carrier density* and the *carrier mobility* in a sample. A Hall effect measurement set up applies a magnetic field, $\mathbf{B}$, to a current inside a material and exploits the *Lorenz force* experienced by electrons passing through the material:

$$\mathbf{F} = -e(\mathbf{E} + \mathbf{v} \times \mathbf{B}) \tag{3.7}$$

$\mathbf{F}$ is the Lorenz force acting on an electron, $\mathbf{E}$ is the field inside the material, e is the elementary charge (with a minus sign since electrons are in question) and $\mathbf{v}$ is the velocity of the electron. If a magnetic field, B_z, is applied perpendicular to the direction of the current as shown in figure 3.5, electrons will be deflected perpendicular to both B_z and the current density in the x-direction, J_x. No electrons are allowed to escape in the y-direction (cf. fig 3.5), the electrons will be accumulated and a field will build up. This field is termed the *Hall field*, E_y, and it

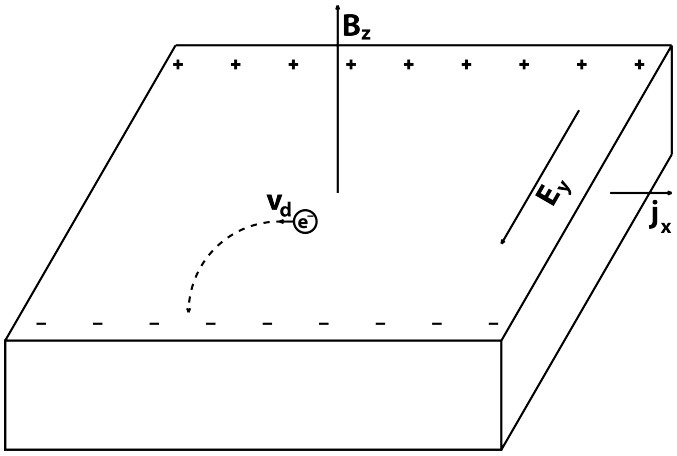

Figure 3.5: A magnetic field, B_z, present in a material containing moving charge carriers will deflect the charges and an electric field, E_y, will be established perpendicular to both B_z and the direction of the current density, j_x. Figure adapted from Hemmer [8].

counteracts the force experienced by electrons from the magnetic field. The build up of such a field is known as the *Hall effect*. The force in y-direction balances, and equation 3.7 can be written as

$$E_y = v_x B_z \tag{3.8}$$

v_x is the velocity of electrons in the material and can be written as a function of current density, J_x, and electron density, n:

$$v_x = -\frac{J_x}{en} \tag{3.9}$$

By combining and rearranging equations 3.8 and 3.9, we arrive at the formula for the *Hall coefficient*, R_H

$$E_y = -\frac{J_x}{en} B_z = R_H J_x B_z, \;\; R_H \equiv -\frac{1}{en} \tag{3.10}$$

From this it is evident that the Hall coefficient can be determined by passing a known current density, J_x, through the material while applying a known magnetic field, B_z, and measuring the field which builds up transverse to J_x and B_z. By such a measurement, the electron density, n, of the material may be determined.

The majority carrier in the material may be positive, as it is in p-type semiconductors where holes are dominant. The previous equations are still valid, although with a different sign in equations 3.7, 3.9 and 3.10 and with p in stead of n in equations 3.9 and 3.10. This means that by viewing the sign of the Hall coefficient, the material can be classified as being dominated by either negative or positive charge carriers. In semiconductors this will translate to n-type or p-type.

With information on the concentration of charge carriers, the mobility of the majority carriers in a sample may also be decided. In a specimen where electrons are the dominant carriers, the *conductivity*, σ, can be expressed as a function of the electron density and the *mobility* of the electrons in the material, μ_n:

$$\sigma = -en\mu_n \Leftrightarrow \mu_n = \frac{\sigma}{-en} = \frac{R_H}{\rho} \tag{3.11}$$

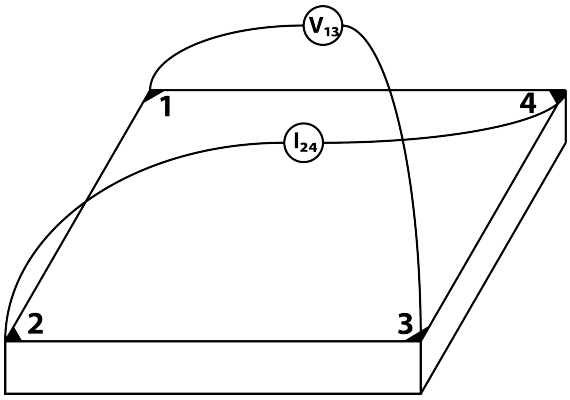

Figure 3.6: In a van der Pauw set up, four contacts (labelled 1-4 in the figure) are made to the sample. Current is passed through two of the contacts while the voltage is measured through the remaining two.

where $\rho = \sigma^{-1}$ is the resistivity of the material. The mobility, μ, of a sample can accordingly be resolved through a measurement of the resistivity, ρ, and the Hall coefficient, R_H. If the material is p-type, the hole mobility, μ_p, rather than the electron mobility is found.

3.2.1 Van der Pauw Method

The *van der Pauw method* is a measurement technique for determining the resistivity, the carrier concentration and the mobility of a sample as devised by L.J. van der Pauw in 1958 [74]. The method dictates that a sample of arbitrary shape can be measured to find the Hall coefficient and the resistivity if the following five points are fulfilled:

1. The sample must be flat and have a uniform thickness
2. The sample must not have any isolated holes
3. The sample must be homogeneous and isotropic
4. The contacts must be at the edges of the sample
5. The contacts must be sufficiently small

Four contacts labelled from 1 to 4 are made to the sample, current is passed through two of them, while the voltage is measured through the remaining two (figure 3.6). By varying which contacts current is passed through and between which contacts voltage is measured, an average resistance can be found [65]:

$$R = \frac{1}{4}\left[\frac{V_{12}}{I_{34}} + \frac{V_{23}}{I_{41}} + \frac{V_{34}}{I_{12}} + \frac{V_{41}}{I_{23}}\right] \tag{3.12}$$

where V_{12} is the voltage measured between contact 1 and 2 while I_{34} is the current passed from contact 3 to contact 4. From this average resistance, the *resistivity* can be found through

$$\rho = R_s t = \frac{\pi t}{\ln(2)} F(Q) R \tag{3.13}$$

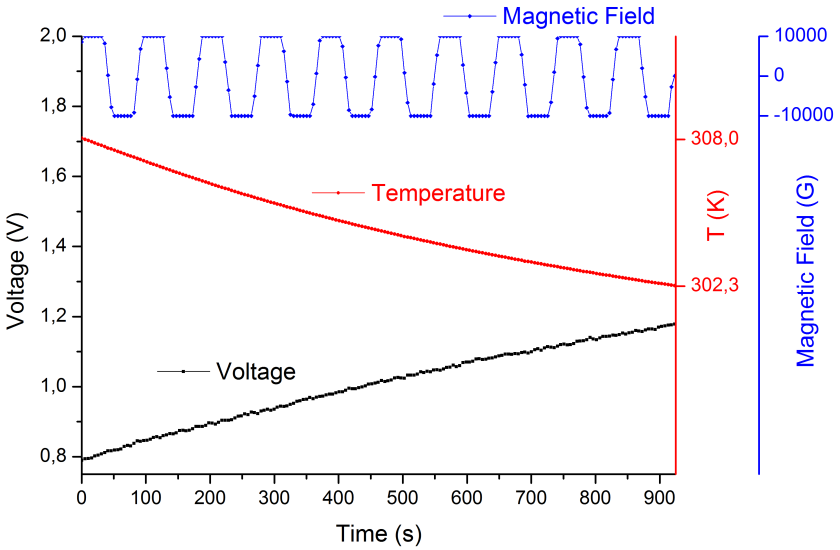

Figure 3.7: The voltage response (bottom line) of a highly resistive material when a current of 1 nA is passed through it. The magnetic field is varied from -10 kG to +10kG, but the voltage measured is not affected by the field. A Hall voltage extracted from this will not contain real information from the sample.

where F(Q) is a correction factor dependent on the probe geometry and t is the thickness of the sample. If the sample is homogeneous, have a uniform thickness, is square and is symmetric with respect to the contact positions, $F(Q) = 1$. Note that these measurements of resistivity does not require a magnetic field present.

When the Hall coefficient is to be decided however, a magnetic field needs to be applied perpendicular to the sample. By applying a magnetic field in both positive and negative z-direction while measuring voltage between two terminals (and passing current between the other two), an average *Hall voltage*, V_H, can be found. Different combinations of terminals is done to get a larger ensemble. From the Hall voltage, the current density can be found through equation 3.10, and by realizing that $V_H = E_y w$, where w is the width of the sample. When the resistivity and the carrier concentration is known, the mobility can easily be extracted through equation 3.11. The Hall coefficient is thus readily obtained, and through simple electrical measurements, the resistivity, the carrier concentration, the mobility and the type of conductivity of the material (n-, or p-type) can be deduced with the van der Pauw method.

Although the van der Pauw method is an easy and precise way of obtaining the electrical characteristics of a material, it has some limitations. To extract the carrier density from a material, a Hall voltage must be measured when a magnetic field is applied. However, if the material has a high resistivity, the Hall voltage is difficult to determine. This can be seen in figure 3.7 where the magnetic field was varied while the voltage was monitored for a highly resistive sample. The voltage exhibits no dependence on the magnetic field, and no Hall voltage can be extracted. A carrier density determined from such a material will not reflect any real properties of the material. The resistivity however, does not rely on a magnetic field excitation to get reliable results and the resistivities determined from the set up can be trusted at higher resistivity values than the carrier densities can. For the set up used in the present study, carrier densities determined from materials with a resistivity higher than 100Ωcm can

not be trusted while the resistivites can be trusted up to a value of $1\times10^7\Omega$cm. At higher resistivity values, the resistance of the samples increases above 1 GΩ, and a resistance bridge connected in parallel with the sample in the set up will start to conduct a significant part of the current. Since mobility values are extracted through the combination of the carrier density and the resistivity, only the samples which give reliable carrier density values provide trustworthy mobility results.

3.3 X-Ray Diffraction

This section is based on the textbook by Birkholz [75].

X-ray Diffraction (XRD) is a powerful technique in which several of the crystal characteristics of a material may be determined. The technique relies on the scattering of X-rays by certain crystal planes in a material.

X-rays incident on a material will interact with the atoms in different ways. The X-rays may transfer their energy to an electron which is liberated from the host atom. This is the famous *photoelectric effect* described by Albert Einstein in 1905, which lead (among other achievements) to him receiving the Nobel Prize in Physics in 1921. The X-rays may also be scattered inelastically by the electrons transferring part of their energy and momentum to the electrons. This type of interaction is termed *Compton scattering* after Arthur Compton. A third way the X-rays can scatter in a material is if the electron cloud is excited by the wave of X-rays and resonates with the frequency of the incoming X-rays. This oscillation leads to an emission of electromagnetic radiation with the same energy as the incoming X-rays, and thus an elastic scattering of the X-rays. This type of elastic scattering of electromagnetic radiation is named *Thomson scattering* after J.J. Thomson. XRD relies on Thomson scattering of X-rays to get structural information on a sample. Since the intensity of the emitted radiation from an oscillating charged species depends inversely on the square of the mass of the species, the scattering from the nuclei of the atoms may be neglected and only the scattering from electrons in the material needs to be considered.

To illustrate the mechanisms of the elastic scattering of X-rays, consider a wave with wave vector $\mathbf{K_0}$ incident on a simple cubic, crystalline material. This wave will be scattered by several of the crystal planes in the material, and the scattered wave will have a wave vector $\mathbf{K}$. The difference between the incoming and scattered wave vector is termed the scattering vector, $\mathbf{Q}$:

$$\mathbf{Q} = \mathbf{K} - \mathbf{K_0} \tag{3.14}$$

as seen in figure 3.8. The intensity of the scattered wave will depend on whether the reflections of the different crystal planes will interfere constructively or destructively, and the Laue equations give the conditions of maximum intensity of the scattered wave:

$$\begin{aligned} a\mathbf{Q}\mathbf{a_1} &= 2\pi h \\ a\mathbf{Q}\mathbf{a_2} &= 2\pi k \\ a\mathbf{Q}\mathbf{a_3} &= 2\pi l \end{aligned} \tag{3.15}$$

where a is the lattice constant of the cubic lattice, $\mathbf{a_{1,2,3}}$ is the unit vectors of the crystal coordinate system and h, k and l is the *Miller indices* of the crystal planes contributing to the reflection. The magnitude of $\mathbf{Q}$ at maximum intensity can then be found by taking the

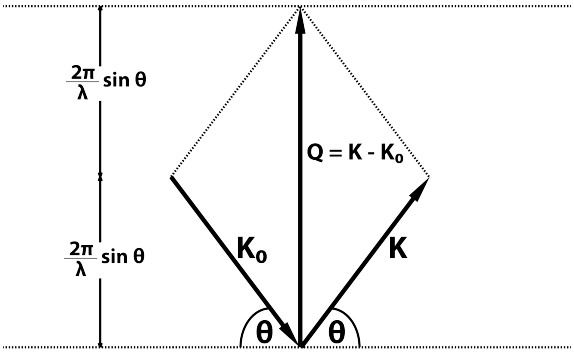

Figure 3.8: An incoming wave with wave vector **K** will be scattered on a crystal plane with a scattered wave vector of $\mathbf{K_0}$. The difference between these vectors is known as the scattering vector, **Q**. Figure adapted from Birkholz [75].

absolute value of the sum of the three crystal directions in equation 3.15.

$$\frac{|\mathbf{Q}|}{2\pi} = \frac{\sqrt{h^2+k^2+l^2}}{a} \tag{3.16}$$

and by using the geometry of figure 3.8, the equation

$$2\frac{a}{\sqrt{h^2+k^2+l^2}}\sin\theta = \lambda \tag{3.17}$$

can be realized. Here θ is as defined in figure 3.8 and λ is the wavelength of the incoming (and outgoing) wave. By making use of

$$\frac{a}{\sqrt{h^2+k^2+l^2}} = d_{hkl} \tag{3.18}$$

where d_{hkl} is the distance between two adjacent lattice planes with Miller Indices h, k and l, equation 3.17 can be written as

$$2d_{hkl}\sin\theta_B = \lambda \tag{3.19}$$

where θ_B is the angle at which maximum intensity is achieved for a reflection. Equation 3.19 is the well known *Bragg equation* and relates the angles at which the scattering intensity reaches a maximum to the distance between lattice planes. When a XRD spectrum is acquired, peaks will appear at the angles satisfying the Bragg equation, and they are labelled *Bragg reflections*. Equation 3.19 can also be deduced by using that in order for constructive interference to occur, the path difference between two parallel beams needs to be an integral multiple of the wavelength. Through geometrical considerations of figure 3.9, equation 3.19 is obtained.

The equations derived above assumes a simple cubic crystal lattice with only one atom per unit cell, but it does apply to other crystal structures also (with different relationships between d_{hkl} and a, i.e. equation 3.18 changes). However, due to destructive interference stemming from atoms in the same unit cell, certain reflections disappear for more complex structures. For instance, for a fcc crystal, the crystal planes with Miller Indices all even or all odd will give constructive interference, while crystal planes with mixed Miller Indices will give destructive interference. For a bcc crystal, reflections will appear if $h+k+l = 2n$, where n is an integer, and there will be no reflections otherwise. Because of differences in lattice constants between different materials and the constraints presented above, an XRD

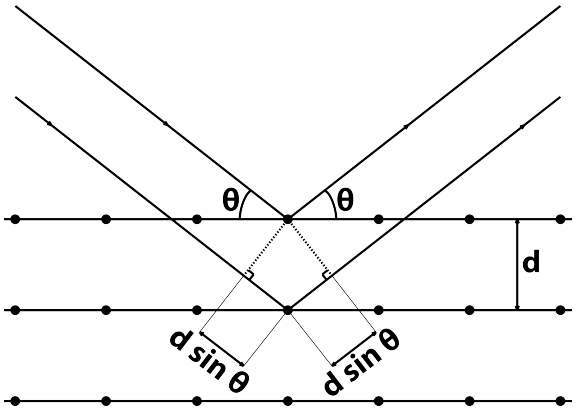

Figure 3.9: Bragg's equation can be derived through geometrical considerations. The difference in path between two waves scattered by two parallel crystal planes is $d \sin\theta$. For constructive intereference to occur, this distance must be an integral multiple of the wavelength of the incoming wave.

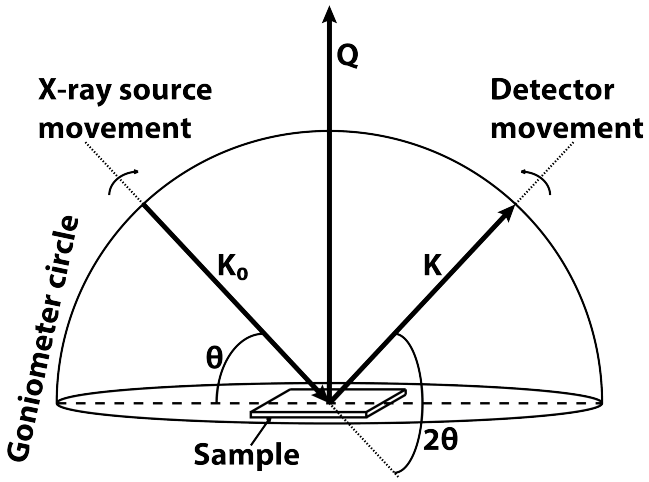

Figure 3.10: The basic set up of a $\theta/2\theta$ scan. Figure adapted from Birkholz [75].

spectrum of a certain material will give peaks at specific (and predictable through equation 3.19) angles, and the material will exhibit a fingerprint pattern which can be used to determine which phases are present.

3.3.1 $\theta/2\theta$ Scan

A $\theta/2\theta$ scan can be used to acquire a fingerprint pattern as mentioned above to determine the phase of the film. The basic set up of a $\theta/2\theta$ scan is as shown in figure 3.10. The sample is placed in the center of a circle traced by the X-ray source and the detector, and when the source moves an angle θ, so does the detector. To reduce the degrees of freedom in a measurement, the distance from source to sample and from sample to detector is always kept constant at the radius of the circle (termed the *Goniometer circle*) traced by the source and the detector. By examining figure 3.10, it can be seen that the angle between the extended incoming beam, $\mathbf{K_0}$, and the exiting beam, $\mathbf{K}$, is 2θ, hence the name of the technique. The exiting beam will have an intensity profile dependent on angle, and maximum intensity will be

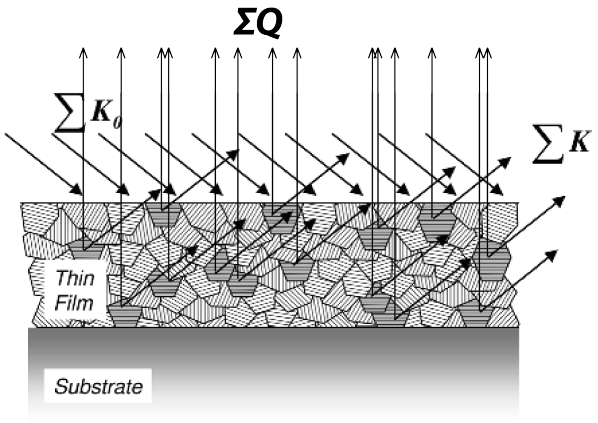

Figure 3.11: A $\theta/2\theta$ scan of a thin film sample, will only record reflections originating from grains with lattice planes parallel to the surface. Figure adapted from Birkholz [75]

determined by equation 3.19. By using accurate lattice constants and the constraints placed on the Bragg equation due to interference, a $\theta/2\theta$ spectrum can be used to determine the elemental composition of the film. Databases of peak positions (and relative intensities) are excellent tools for fast determination of the chemical phases.

If a thin film with differently oriented grains is investigated, then only certain grains will give significant contributions to the intensity peaks in the spectrum. This is evident by viewing the scattering vector, **Q**, in a polycrystalline thin film as illustrated in figure 3.11. The scattering vector in a $\theta/2\theta$ scan is always perpendicular to the surface normal, and only the lattice planes oriented parallel to the surface will scatter **K** into the detector, thus will only grains with lattice planes parallel to the surface contribute to the acquired spectrum. This places further constraint on the planes which will scatter into the detector, and makes it harder to determine the chemical phase of a thin film. However, taking this into account several other parameters can be discerned from a $\theta/2\theta$ scan of a thin film, including the average lattice constant, the in plane stress (the stress parallel to the scattering vector) of the film and the average grain size in the direction parallel to the scattering vector.

If instrumental aberration is neglected, the lattice constant, a, can be calculated directly from the Bragg equation and the peak position of a reflection with Miller indices hkl. The in plane stress of the film, σ_{film}, can further be deduced by using the formula relating absolute stress and lattice constant in the c-direction of a hexagonal lattice, like ZnO, presented by Cebulla et al. in [76].

$$\sigma_{film} = \frac{2c_{13}^2 - c_{33}(c_{11} - c_{12})}{2c_{13}} \left(\frac{c_{film} - c_{bulk}}{c_{bulk}} \right) \tag{3.20}$$

where c_{11}, c_{12}, c_{13} and c_{33} are the elastic constants of ZnO, c_{film} is the measured c lattice constant of the film and c_{bulk} is the the reference lattice parameter. Cebulla et al. used values obtained from [77] and combined the elastic constants to get

$$\sigma_{film} = -233\epsilon \tag{3.21}$$

where ϵ is the strain in the c direction equal to the term in parentheses in equation 3.20 and σ_{film} is given units of GPa.

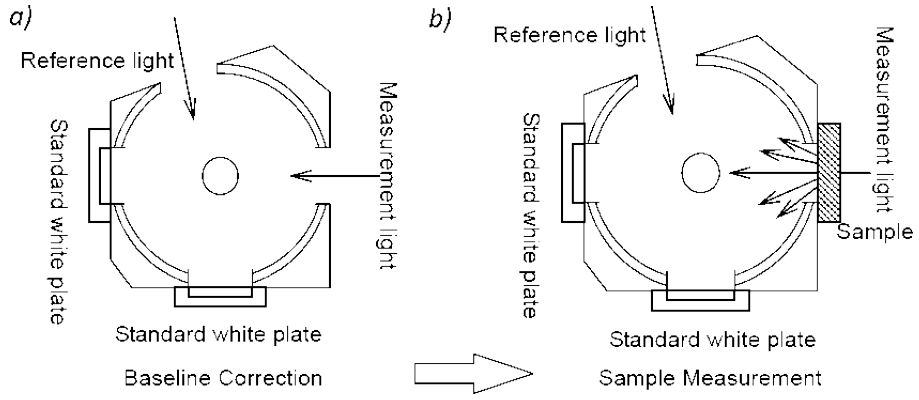

Figure 3.12: A transmittance measurement as seen in b) is preceded by a baseline correction seen in a). Figure taken from the Shimadzu "Traning Course for Analysis of Solid Samples" document, for UV/VIS spectrophotometers.

The average grain size in the growth direction of the film can also be determined from a $\theta/2\theta$ spectrum through the Scherrer equation [78] and the Full Width at Half Maximum (FWHM) of a peak with Miller indices hkl.

$$D_{cube,mono} = 2\sqrt{\frac{ln2}{\pi}}\frac{\lambda}{\beta_{2\theta}\cos\theta_B} \tag{3.22}$$

Here, $D_{cube,mono}$ denotes the grain size of the film, the subscript $cube, mono$ indicates that the formula is valid for monodisperse grains of cubic shape, λ is the wavelength of the incoming radiation, $\beta_{2\theta}$ is the FWHM and θ_B is the Bragg angle. Equation 3.22 assumes that the broadening of the peak only stems from small crystallites and that no microstrain is present in the sample. This is not a real situation as there will always be some microstrain in a sample, and $D_{cube,mono}$ is thus associated with a certain inaccuracy. Furthermore, the peak is broadened by the small crystallite size, but also by an instrumental broadening. If the probing beam assumes a Cauchy type shape, the FWHM needs to be adjusted according to:

$$\beta_{2\theta} = \beta_{2\theta m} - \beta_{2\theta i} \tag{3.23}$$

where, $\beta_{2\theta m}$ is the measured FWHM and $\beta_{2\theta i}$ is the instrumental broadening of the FWHM. In this work, $\beta_{2\theta i}$ is determined to be 0.008°.

3.4 Transmittance Measurements

To measure the *transmittance* of a film, light is passed through a sample and detected. The transmittance can be resolved with respect to wavelength when the incoming light is monochromatic and the wavelength can be varied.

Figure 3.12 shows a set up where a sample is placed immediately outside a reflecting sphere. The sample is illuminated with monochromatic light, and the transmitted light is detected inside the sphere. The purpose of the reflecting sphere is to detect both the directly transmitted and the diffusely transmitted light. The transmittance, $T_{film}(E)$, through a free standing thin film sample in such a measurement configuration can be approximated by

$$T_{film}(E) = (1-R)^2 \mathrm{e}^{-\alpha(E)d} \tag{3.24}$$

if interference effects and multiple reflections are disregarded. This is a form of the *Beer-Lambert law* where R is the reflectivity of the two surfaces of the sample, d is the thickness of the film and $\alpha(E)$ is the absorption coefficient of the sample. A free standing thin film is not a realistic case, and the film is usually deposited on a thick substrate. The measured transmittance of a thin film sample deposited on a substrate is therefore influenced by both the substrate and the film. A simple relationship is assumed ($T_{film} = \frac{T_{film+substrate}}{T_{substrate}}$), and if the transmittance of the substrate, $T_{substrate}$, is measured separately, the absorption coefficient of the film can be extracted as:

$$\alpha(E) = -\frac{1}{d} \ln \left(\frac{T_{film+substrate}}{T_{substrate}} \right) \tag{3.25}$$

$T_{film+substrate}$ is the transmittance through the thin film deposited on a substrate. The absorption coefficient in a semiconductor is dependent on the band structure of the material, and in a direct band gap semiconductor, the relation

$$\alpha(E) \propto (E - E_g)^{1/2} \tag{3.26}$$

is valid. Plotting $\alpha(E)^2$ versus photon energy will yield a straight line in the region where there is high absorption. Extrapolating the line to the energy axis will give an approximation of the band gap, E_g, as the interception with the axis.

Transmittance measurements can thus be used to estimate the band gap of a material and to measure the transmittance of a film.

3.5 Atomic Force Microscopy

This section is based on the textbooks of Kittel [7], Brandon and Kaplan [79], Mironov [80] and the paper by Binnig [81].

Atomic Force Microscopy (AFM) is a surface investigation technique where a sharp tip attached to a thin *cantilever* (figure 3.13) is brought in close contact with the surface of the sample to be investigated. The tip is then scanned across the surface, and will experience both attractive forces such as van der Waals forces and repulsive forces such as Pauli repulsion. These forces deviate the cantilever from its equilibrium position, the changes can be detected and an image of the surface topography is formed.

One principle of detecting the deflections of the cantilever is optical detection and this is what is used in contact mode. A laser is focused on to the end of the cantilever and the reflection of this laser is detected by split photodiodes (figure 3.13). The diodes generate a photocurrent depending on how large a part of their area is illuminated, and by monitoring the photocurrent, the position of the cantilever can be deduced. A feedback system ensures that the photocurrent stays constant. This adjustment is made through a piezoelectric transducer connected to the cantilever: The change in current from the photocurrents is transferred to a different voltage applied to the piezo, which in turn will change its shape and adjust the position of the cantilever. The voltage response of the piezo is known, and by monitoring the voltage on the piezo as a function of position in the plane, a map of deflections in the direction normal to the surface can be formed: A map of the topography of the sample.

Several modes of operation are possible with an AFM, with the most fundamental ones being *contact mode* where the tip of the cantilever is in contact with the sample, *non-contact mode* where the cantilever is oscillated outside the surface of the sample and *tapping mode*

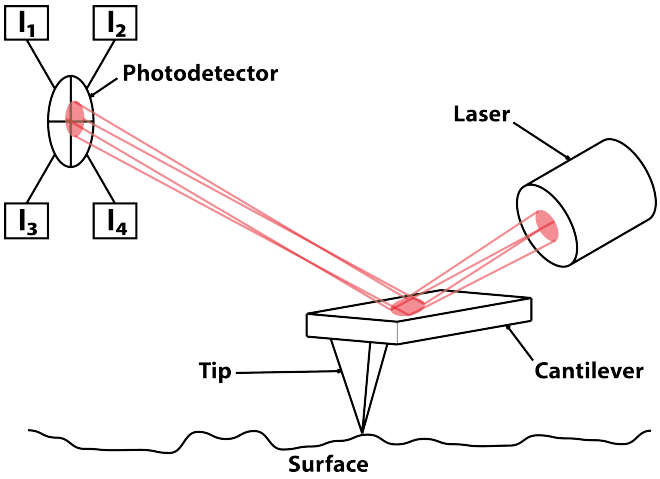

Figure 3.13: An optical detection system for contact AFM. A laser is focused on the cantilever, and the cantilever reflects the beam. The reflection is picked up by a photodetector. The photodetector consists of four diodes where the current generated from each is proportional to the illuminated area. As the tip scans the surface, the cantilever changes position, the reflection on the photodiodes changes, the illuminated area of each diode changes and the current from each diode changes. This is recorded and used for mapping the surface. Figure adapted from Mironov [80].

where the cantilever is oscillated closer to the surface, and the tip is in contact with the surface in the lower extreme of the movement. In this work, only tapping mode was applied.

3.5.1 Tapping Mode

In tapping mode, the cantilever is oscillated at an amplitude of $\sim$ 10-100 nm, and in the lower part of the oscillation, the tip will touch the surface of the sample. The oscillation occurs at a frequency as close as possible to the resonant frequency of the "free" cantilever far from the surface. When the tip is closer to the surface, attractive and repulsive forces are present. These forces can be approximated by a Lennard-Jones potential as seen in figure 3.14. The position of the tip during a few cycles of the oscillation is shown in the same diagram. The amplitude of the oscillation is such that the tip experiences forces dominated by repulsive contributions and forces dominated by attractive contributions during a cycle. As these forces act on the tip, the frequency and amplitude that the cantilever oscillates with is changed. A change in amplitude is related to a change in position of the cantilever with respect to the surface. Again, the signal from the cantilever is changed into a voltage applied to the piezoelectric transducer which counteracts the amplitude shift and by monitoring the voltage, an image of the topography of the surface can be obtained.

3.6 Transmission Electron Microscopy

This section is based on the textbook by Brandon and Kaplan [79].

Transmission Electron Microscopy (TEM) is a characterisation technique in which electrons are accelerated through a column and allowed to pass through a sample. The transmitted the electrons are detected by a phosphorous screen or a CCD camera and an image or a diffrac-

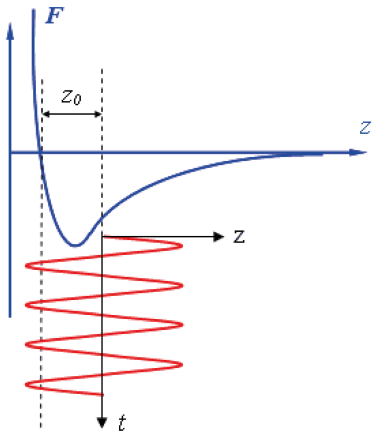

Figure 3.14: As the tip in an AFM approaches the surface, it will first experience Coulombic attraction and as it gets closer, a repulsion due to overlapping wave functions (Pauli repulsion). This potential is approximated by the Lennard-Jones potential seen in blue in the figure. The position of the tip in AFM tapping mode is also seen in red. The tip oscillates between the repulsive and attractive regions above the surface. Figure taken from Mironov [80]

tion pattern of the sample can be formed.

As with light in a light microscope, the electrons in a electron microscope need to be focused on to the sample. This is achieved with electromagnetic lenses where an electromagnetic field bends the path of electrons. When the electrons hit the sample, they can interact elastically or inelastically with the atoms. The inelastic collisions contain information on the chemical composition and band gap of the sample and are exploited in *Electron Energy Loss Spectroscopy* (EELS), while the elastic collisions are taken advantage of in TEM. The elastic collisions can give rise to contrast in the TEM image in three different ways:

1. Mass-thickness contrast
2. Diffraction contrast
3. Phase contrast

The *mass-thickness contrast* arises from electrons which are scattered on their way through the material. The probability that a scattering event occurs increases with the thickness and the density of the sample. Thus will thicker and denser areas of the sample transmit fewer electrons than thinner and less dense areas and a contrast depending on these two factors can be achieved.

The scattered electrons will be spread randomly if the sample is amorphous, but in a crystalline sample, the scattering directions which fulfill Bragg's law are preferred, and the contrast which arises from this scattering is known as *diffraction contrast*. The modes of operation when exploiting diffraction contrast and mass-thickness contrast is *Bright Field* imaging. In Bright Field imaging, the directly transmitted beam is registered, and Bright Field imaging thus utilises both mass-thickness contrast and diffraction contrast. In Dark Field imaging, the beam which is scattered along a certain crystal direction is imaged, and only diffraction contrast is exploited.

If the directly transmitted beam and one or more of the diffracted beams can be collected by

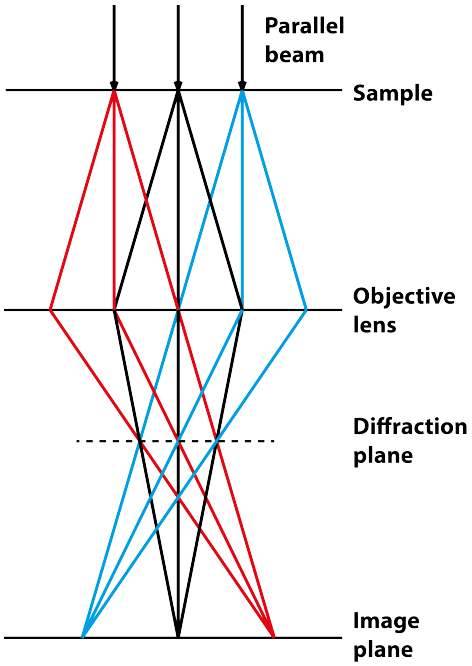

Figure 3.15: A simplified ray diagram in a TEM. The sample will scatter the beams, while the objective lens focuses the beams to the image plane. At the diffraction plane, information on the lattice of the sample can be found.

introducing a larger objective under the sample, the different length the various beams need to travel leads to a phase difference. This phase difference will give the contrast exploited in *phase contrast* imaging. The imaging technique is commonly called *High Resolution Transmission Electron Microscopy* (HRTEM). As the name implies, small objects can be seen, and objects below 50 pm have been resolved [82].

The imaging techniques mentioned here all rely on the camera or the viewing screen being positioned at the image plane (see figure 3.15). If the electrons are detected in the diffraction plane instead, a diffraction pattern can be obtained. The image formed in the diffraction plane is a projection of the reciprocal space of the material and information on the lattice of crystalline materials can be acquired.

3.7 Photoluminescence Spectroscopy

This section is based on the review by Gilliland [83].

Photoluminescence (PL) *spectroscopy* is a technique where the radiative relaxation of carriers is measured. It is useful for characterising the optical properties of a semiconductor, and through these optical properties, characterising defect species and estimating defect concentrations in a material.

The technique utilises a monochromatic laser to excite electrons across the band gap of the semiconductor in question. These electrons will quickly thermalise to the band edge of the conduction band and will through different pathways, relax to their equilibrium state in the valence band through the recombination with a hole. Several recombination mechanisms will occur when an electron population relaxes and examples of such mechanisms are presented in

figure 3.16. Through defect levels in the band gap, the electrons may relax in two or more steps. Each relaxation step can have the potential for emitting a photon. By registering the photons which are emitted by a sample, the position of defect energy levels inside the band gap and their concentrations can be deduced. PL spectroscopy measures the radiative recombination of carriers, but non-radiative recombination where a phonon is emitted is also a prominent pathway complicating the detection of defect energy levels.

3.8 Rutherford Backscattering Spectrometry

This section is based on the papers by Chu et al. [84] and Perriere [85] as well as the Evans Analytical Group RBS tutorial [86].

Rutherford Backscattering Spectrometry (RBS) is an analytical tool useful in establishing the concentration and distribution of an element in a sample. The principle of RBS is based on bombarding a sample with energetic ions (typically He^{2+}-ions) and registering the energy loss the ions experience when interacting with the sample.

Consider a He^{2+}-ion accelerated to an energy of 2 MeV incident on a sample surface. One of the possible interaction the ion can have with the sample is elastic scattering and in RBS the elastic *backscattering* is exploited and the energy of the backscattered ion is measured (figure 3.17). The energy of the backscattered ion depends on many factors including the incoming energy of the ion, the type of atoms which are involved in the scattering event and how far inside the sample the ion has penetrated. If the ion collides with a stationary atom at the surface, the ion will be backscattered if the atom has a higher mass than the ion and part of the energy of the ion will be transferred to the atom. If the energy, E_1, of the backscattered ion is registered, it is possible to deduce which atom the ion collided with through:

$$E_1 = K_M E_0 \tag{3.27}$$

where E_0 is the energy of the incident ion and K_M is the kinematic factor of the collision given by:

$$K_M = \left(\frac{m \cos\theta + \sqrt{M^2 - m^2 \sin^2\theta}}{m + M} \right)^2 \tag{3.28}$$

where m is the mass of the incoming ion, M is the mass of the scattering atom and θ is the scattering angle. m is known in the experiment, and θ is known through the position of the detector, which means that the mass of the scattering atom, M, can be deduced.

However, the ion can also penetrate the surface and be backscattered by atoms below the surface. On its way through the material, the ion will lose energy due to friction from the electron clouds of the atoms in the material (figure 3.17), the energy which is registered at the detector is lower than that for an ion scattered at the surface and the spectrum will exhibit an energy spread, ΔE. This energy spread is related to the elements present in the sample (through the stopping power of the electron clouds) and the thickness of the sample, t.

$$\Delta E = [S]t \tag{3.29}$$

[S] is the energy loss factor dependent on the elements present in the material. This means that the thickness and the constituents of the material can be extracted quite easily from the spectrum.

The ratio of concentration between the different elements present in the sample can also

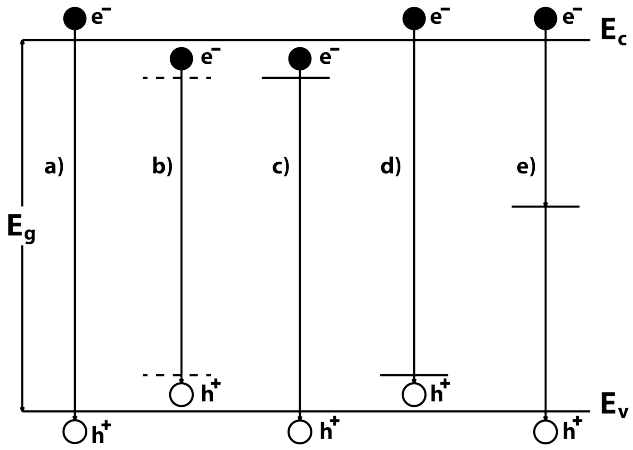

Figure 3.16: Examples of recombination mechanisms in a semiconductor. a) Band to band, b) Exciton recombination[1] , c) Defect state to valence band, d) Conduction band to defect state, e) Via a deep trap state.

[1]An exciton is a conduction band electron and a valence band hole bound together by Coulombic attraction. It is regarded as a quasiparticle that can move through the material. The quasiparticle has a lower energy than an unbound electron and hole and thus has an energy state in the band gap.

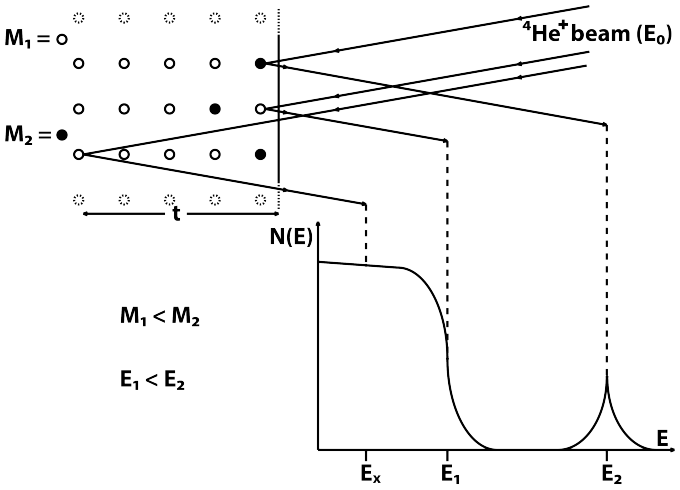

Figure 3.17: In Rutherford Backscattering Spectrometry, a beam of He-ions is incident on a material. Ions scattered at the surface by heavy atoms will have a high energy (E_2), while ions scattered at the surface by lighter elements will have a lower energy (E_1). When the He-ion moves thorugh the material through electron stopping, and an ion scattered within the material will have an even lower energy (E_x). Adapted from Perriere [85]

be extracted by considering the integrated area of the peaks of the individual elements. If elements A and B are present in the material, the ratio between the concentrations, $\frac{N_a}{N_b}$, is:

$$\frac{N_a}{N_b} = \frac{A_a \sigma_b}{A_b \sigma_a} \tag{3.30}$$

Here, $\sigma_{a,b}$ is the differential scattering cross section of species A or B, and $A_{a,b}$ is the integrated peak area related to either element A or B. The ratio in 3.30 is also easily realised from the energy spectrum of the backscattered ions, but absolute concentration measurements are not so easily obtained. To get a reliable value for N_a or N_b, careful calibration and measurement of the set up is required as the integrated charge of the ion beam and the exact active area of the detector is needed.

RBS is thus a useful technique for determining the stoichiometry and thickness of a sample, and it can also be used for establishing the absolute concentrations of constituents if the set up is properly calibrated.

3.9 Stylus Profilometry

This section is based on the paper by Krüger-Sehm [87].

Profilometry is a surface measuring technique which can be used to obtain a image of the topography of a surface or to measure the film thickness of a sample. Profilometry can be divided into contact profilometry and non-contact profilometry where the latter utilizes the different interactions light has with the surface of a sample [88]. Contact profilometry or *stylus profilometry* is a technique similar to AFM where a sharp tip is scanned across a surface.

Unlike AFM, the tip does not require atomic sharpness, rather it needs to be wear resistant and the tip radius is usually between $0.1 - 50\mu m$. The tip is kept in contact with the surface and follows its contours. As the tip moves across the surface and moves vertically and laterally,

this movement is detected by a sensor (such as an inductive, capacitive or piezoelectric sensor) and transduced to a electrical signal. This signal is used by a feedback system which adjusts the force exerted on the tip. The transduced signal is recorded and converted to a height distribution diagram. If the tip is scanned in rasters across the surface, then the height distributions can be combined into a surface topography map much like how an image is formed in AFM.

Thin film thickness can be measured if the film has an abrupt edge. The tip is then scanned across this edge, and the height distribution diagram will provide a measure of the thickness of the film.

Chapter 4

Results

This study was initially undertaken to verify the presence of Si Nanocrystals embedded in a ZnO matrix deposited by RF magnetron co-sputtering as shown by Lai et al. [48] and to confirm the work of Schofield [49]. The thesis work has also investigated the effects of annealing temperature and different substrates on the electrical, optical and structural characteristics of the sputtered films. The electrical characteristics as a function of Si content, substrate used and annealing temperature were examined by Hall effect measurements, while the optical characteristics of the films were inspected by transmittance measurements and photoluminescence (PL) spectroscopy. The structural characteristics were studied by X-ray diffraction (XRD), transmission electron microscopy (TEM) and atomic force microscopy (AFM). The data treatment was done using the Origin (version 8.6, OriginLab, Northampton, MA) and the WSxM (version 3.1, Nanotec Electronica S.L. [89]) software packages.

4.1 Experimental Equipment and Procedures

4.1.1 Equipment

Sputtering Deposition of the films was done with a Semicore Tri-Axis balanced field magnetron sputtering system. Both DC and RF sputtering are available in the system, and co-sputtering is possible as three target cathodes facing the substrate can be operated individually and simultaneously. The distance between the target and substrate was kept at $\sim 10.5 - 11.5$ cm. The targets used were a 99.99% pure ZnO target, a 99.999% pure Al target and a p-type Si wafer.
Hall Effect Measurements For determining the electrical properties of the films, a Lakeshore 7704A Hall effect measurement system was utilised.
XRD X-ray diffraction of the films was realised with a Bruker D8 Discover system with a Cu x-ray source. The x-ray source had characteristic peaks with wavelengths $k_{\alpha 1} = 1.5406$ Å and $k_{\alpha 2} = 1.54444$ Å. A Göbel mirror is implemented to filter out the $k_{\alpha 2}$ signal.
Transmittance Measurements A Shimadzu Solidspec 3700 DUV spectrophotometer was used for transmittance measurements. The set up utilises an integrating sphere for measurements and the wavelength range of the system is 175 - 3300 nm.
AFM Atomic force microscopy was done with a Veeco Dimension 3100 Atomic Force Microscope. The measurements were done in tapping mode. The lateral resolution of the equipment is <1 nm.
TEM Transmission Electron Microscopy was done in Trondheim at the Norwegian Univer-

sity of Science and Technology by Dr. Ragnhild Sæterli. She used a JEOL2010F with an acceleration voltage of 200 kV to investigate the films.
PL Photoluminescence (PL) was investigated by employing a 325 nm wavelength continuous wave He-Cd laser with an output power of 10 mW as an excitation source. The emission was collected by a microscope and directed to a fiber optic spectrometer (Ocean Optics USB4000, spectral resolution 2 nm).
RBS RBS analysis was done using a 1 MV Tandem ion accelerator (National Electrostatics Corporation). The probing beam consisted of 1.836 MeV $^7Li^+$ ions incident along the [0001] direction. The beam was backscattered into a detector at 170 degrees relative to the incident beam direction. Simulations were performed with SIMNRA code (http://home.rzg.mpg.de/ mam/).
Stylus Profilometry To measure the thickness of the films, a masked etching and a subsequent profilometry was done. The profilometry was done with a Veeco Dektak 8 while HCl:H_2O_2:H_2O (1:1:20 volume ratio) was used as an etchant of the films.

4.1.2 Sample Preparation

Glass, Si, Si + SiO_2, amorphous ZnO and quartz have been used as substrates for the films, and different preparations apply for the different substrates. The glass substrates were cut from microscope slides, ultrasonically cleaned in acetone for 5 minutes, ethanol for 5 minutes and water for 5 minutes and then dried in N_2 flow. The (100) p-type (B-doped) Si substrates were cleaned by the RCA cleaning process. RCA cleaning was also used for the Si + SiO_2 substrates as the SiO_2 layer was thermally grown on a (100) p-type (B-doped) Si substrate which was cleaned with the RCA process before thermal oxidation in a tube furnace at 1100°C was performed. The amorphous ZnO was deposited on glass substrates by magnetron RF co-sputtering with a Si content high enough to produce an amorphous layer of ZnO:Si, and this layer was then used as the substrate for a polycrystalline film of doped ZnO. The glass substrates was cleaned as described above. Finally, the quartz substrates were cut from a 3 inch crystalline quartz wafer by laser ablation and then ultrasonically cleaned in HCl for 5 minutes, isopropanol for 5 minutes and water for 5 minutes. The substrates were dried in N_2 flow.

Deposition of the films on the substrates was done with the sputtering equipment described above with the power applied to the ZnO target kept constant at 50 W for all the films and the target power of Al in the Al-doped films at 7W. The Si content of the Si-doped films was varied through varying the power applied to the Si target (the values used being 7W, 10W, 12 W, 15 W and 25 W). The Ar gas flow was kept at 70 Standard Cubic Centimeters per Minute (SCCM), the base pressure was $<2\times10^{-6}$ Torr, the working pressure was $\sim$ 17 mTorr, the substrate temperature was 400°C and the rotation speed of the substrate to ensure a uniform thickness of the films was 12 rpm.

Post-depostion annealing was done in a tube furnace for 1 h in air at temperatures of 550, 650, 800, 950 and 1050 °C respectively.

4.1.3 Treatment of Errors

4.1.3.1 Hall Effect Measurements Data

Hall effect measurements were used to determine the resistivity, mobility and carrier density of the samples. For each sample, a minimum of two measurements (mostly three) with different excitation currents were made, and an error estimate is made for each sample from these

measurements. With the van der Pauw geometry used however, an instrumental error is introduced when the contacts to the sample are not point contacts. For the resistivity, this error scales as $\sim \left(\frac{d}{l}\right)^2$, where d is the diameter of the contact, while l is the length of the sample. The contacts had an average size of approximately 1.2 mm in diameter while the square samples were 10-15 mm long (depending on substrate). This gives a maximum error margin of 1.4%. For the carrier density and the mobility however, the error scales as $\sim \left(\frac{d}{l}\right)$ and the maximum error margin is 12%. The different error margins are added for each sample to yield a total error margin.

4.1.3.2 XRD Data

The grain size of the samples as well as the stress and the c lattice constant in the films was calculated using the (002) reflection of ZnO. To determine the c lattice constant, the *Bragg equation* (equation 3.19) was used, while the stress is calculated from equation 3.20. In both these equations, the position of the peak is needed. The grain size is extracted from the Scherrer formula (equation 3.22) and this equation utilises the FWHM of the peak as well as the c lattice constant. To estimate an appropriate error range, the same sample was measured five times with removal of the sample from the sample holder between each measurements, and the stress and grain size was estimated for each of these measurements. The stress calculation also utilises a standard value of the c lattice constant of ZnO. The value of this varies between different studies, and this spread in values also leads to an error. From the experimental values given in table II by Özgür et al. [11] and the difference between the measurements, an error of 0.15 GPa is estimated for the samples deposited on amorphous ZnO and Si + SiO_2 while an error range of 0.11 GPa is estimated for the samples deposited on glass, Si and quartz. Grain size error estimates of 2.4 nm for the samples on amorphous ZnO and Si + SiO_2 and 0.5 nm for the samples on glass, Si and quartz are collected from the variation between different measurements.

4.1.3.3 AFM Data

An AFM image is formed when a tip is scanned across the surface of the sample. For each measurement point at the surface, a pixel is created on an image formed of the surface. As an image is formed, the mean roughness and of the surface is calculated by a software (WSxM, version 3.1, Nanotec Electronica S.L. [89]) using the vertical positions of the pixels of the image. Scans on different parts of the sample is made, and the error margins of the AFM data are taken from the variation of the roughness between the different scans.

4.1.3.4 RBS Data

To determine the relative content of Zn, O and Si in the Si doped films, RBS was performed. The RBS spectra was done by Dr. Alexander Azarov at MiNaLab in Oslo, and the data analysis and error margins are both provided by him. The measurement is more sensitive to error when light elements are in question, and Oxygen has a higher error margin (5%) than Zn and Si (0.5%).

4.1.3.5 Stylus Profilometry Data

To determine the thickness of the films, a mask and an etch were applied to get a well defined edge to the film. This edge was then scanned by a stylus profilometer, and a height profile of the edge was obtained. 5 different measurement points were chosen and the mean and the standard deviation of these 5 measurements are used for error estimation.

4.2 Power Series

To produce films with good electrical and structural properties, the sputtering parameters need to be optimised. As ZnO is a material commonly used as a transparent conductive electrode, crucial properties are resistivity and transmittance in the visible range. Optimisation of the sputtering parameters thus means finding the values producing the lowest resistivity and highest transmittance. These properties were determined by transmittance measurements and Hall effect measurements (which also revealed the mobility and carrier density). To further understand the mechanisms governing the resistivity and the transmittance, the crystal quality was investigated with XRD and TEM, while AFM was employed to examine the surface topography. TEM was also employed to confirm the presence of Si nanocrystals.

Previously, Schofield [49] has shown that the best films of ZnO:Si using co-sputtering with the set up at MiNalab in Oslo was produced at a substrate temperature of 400°C-450°C, a ZnO target power of 50 W, an Ar flow of 70 SCCM, a rotation speed of the substrate of 12 rpm and a Si target power of 12 W. These values have been used in this study also, but the Si target power was varied to verify the optimum value. Films with different Si content was thus sputtered on glass substrates and characterised with XRD, Hall Effect Measurements, AFM, Transmittance Measurements, TEM and RBS. A Si target power of 0 W, 7 W, 10 W, 12 W, 15 W and 25 W was used. The sample sputtered with a 0 W Si target power is referred to as the ZnO reference. The deposition time was 70 minutes, and the thickness was measured by etching and subsequent Stylus Profilometry and determined to be 140±10 nm for all the samples except the samples deposited with a 25 W Si target power which had a thickness of 51±10 nm. The ZnO was sputtered from a 99.99% pure ZnO target, while the Si was sputtered from a p-type Si wafer. Both the electrical and structural properties were predicted to improve with Si content up to a certain concentration and then start to degrade. Si nanocrystals were expected to precipitate around a Si power of 12 W.

4.2.1 RBS Results

Rutherford Backscattering Spectrometry was used to determine the relative concentration of the three main elements of the films, namely Zn, O and Si as a function of Si power. In table 4.1, the relative content of Zn, O and Si in the films are presented. The concentration of Si increases as expected with Si target power, although it seems to reach a plateau between 7 W and 12 W Si target power. This is consistent with previous work (figure 2 of Schifano et al. [90]), where this saturation of Si content was presented as a possible indication of Si nanocrystal incorporation in the ZnO film. A detailed study to determine the presence of Si nanocrystals in the ZnO lattice has thus been undertaken in the present work. Parameteres such as Si target power and annealing temperature have been varied, while TEM, XRD and PL spectroscopy have been utilised for characterisation of the nanocrystals. However, characterisation of the samples provided no evidence of Si precipitation, and the plateau of Si

Sample	% Zn	% O	% Si
0 W	42.0±0.5	58±5	0.0±0.5
7 W	42.0±0.5	57±5	1.0±0.5
10 W	44.0±0.5	54±5	1.8±0.5
12 W	47.0±0.5	52±5	1.5±0.5
15 W	42.0±0.5	56±5	2.0±0.5
25 W	30.0±0.5	60±5	10.0±0.5

Table 4.1: The relative content of the three main constituents (Zn, O and Si) in the films for different Si target powers as determined by RBS.

content indicates a true saturation of Si incorporation. Incorporation of Si nanocrystals in a ZnO lattice is further discussed in section 5.1.

From the RBS measurements, it is also evident that there is a large discrepancy between the Zn and the O content in the films. Although the numbers can not be entirely trusted, it is certain that the films are O-rich and that the non-stoichiometry decreases with Si doping up to a Si target power of 12 W and then increases again. This would suggest that Si doping up to a certain concentration is favourable for the stoichiometry of the films. A better stoichiometry implies less defects and better structural and electrical properties.

4.2.2 XRD Results

To investigate the grain size and the stress of the films, a $\theta/2\theta$ scan was performed on the samples. The peak position and FWHM of the (002) reflection of the films was used to determine these parameters. An example of a $\theta/2\theta$ spectrum of the films is presented in figure 4.1. The (002) peak and its replica are the only prominent peaks in the spectrum indicating that the film is preferentially oriented with the c axis perpendicular to the substrate. The crystal quality of the film with 25 W Si power is poor (close to amorphous), and no reflections can be seen in the spectrum (figure 4.2), and data on the grain size and stress are not obtainable from this film.

As can be seen in figure 4.3, the stress in the films decreases with Si doping (note that the stress in the figure is negative indicating a compressive strain). The stress is also increased when the target power of Si reaches 15 W, and a plateau of low stress is formed at low to intermediate doping concentrations. The grain size of the films remains constant for most the films, but the sample deposited with 12 W Si power on glass shows a significantly larger grain size than the other films. A larger grain size and lower stress are indicative of a better crystal quality, and the results thus suggest that the films improve their structural properties when increasing the Si content up to a certain point (12 W in this study) and then the crystal quality degrades again. This is further supported by the intensity of the (002) peaks for the samples as the (002) peak for the 12 W Si sample exhibits more than twice the intensity of the other samples. The intensity of a crystal reflection is an indication of the crystal quality of a material. Although the peak intensity may be somewhat affected by the samples being deposited in different runs (but with the the same sputtering conditions), such a big difference in intensityl reflects real variations in crystal quality.

The films were not only deposited on glass, but Si + SiO_2 was also used as a substrate. However, as seen in figure 4.4, the intensity of the (002) reflection of ZnO is low for the sample on Si + SiO_2 compared to the samples on glass. This indicates that the crystal quality of the

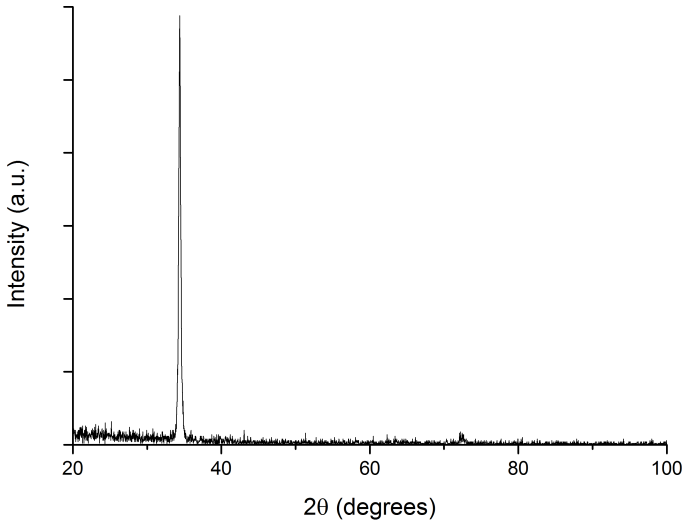

Figure 4.1: A $\theta/2\theta$ spectrum of a film deposited with 12 W Si target power. The (002) reflection can clearly be seen around 34 degrees. No other significant peaks are present suggesting that the material is preferentially grown along the c axis.

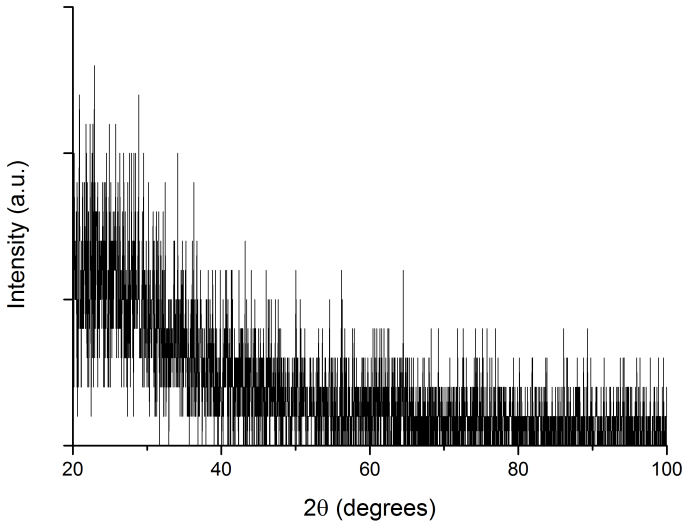

Figure 4.2: A $\theta/2\theta$ spectrum of a film deposited with 25 W Si target power. No discernible reflections can be seen since the crystal quality is poor, and information on grain size and stress is not possible to extract.

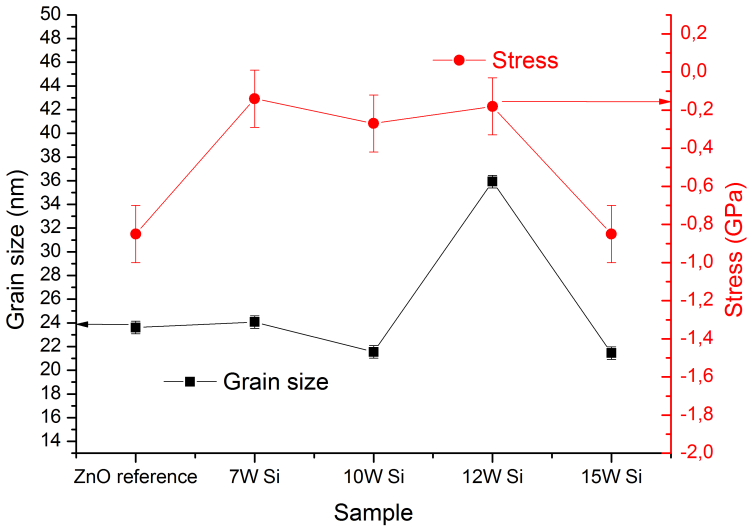

Figure 4.3: The grain size and the stress of the films are shown as a function of Si target power. The grain size is similar for almost all the films except the film deposited with a Si target power of 12 W. The stress is decreased by doping the films with Si, and the stress reaches a low absolute value (note that the stress is negative) with a 12 W Si target power. At 15 W Si target power, the stress increases again.

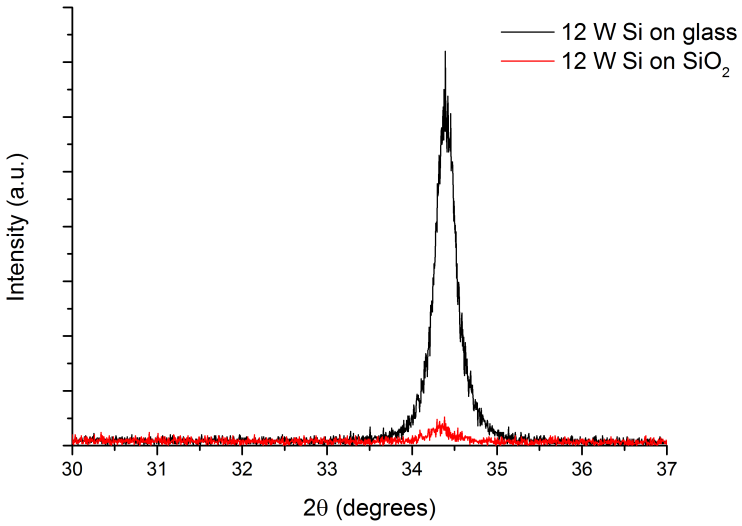

Figure 4.4: XRD spectra around the (002) reflection of ZnO of a sample deposited with 12 W Si target power on glass and on SiO_2

films on Si + SiO_2 is poor compared to the films on glass. Due to the low signal, the analysis results for the samples on Si + SiO_2 are omitted.

The XRD data show that the crystal quality of the films improves with Si doping as the stress of the films is decreased when Si is incorporated in the film. The crystal quality improves with Si target power and at a Si target power of 12 W, the material exhibits the highest grain size and (002) peak intensity. At higher target powers, these parameters are seen to degrade, indicating that a 12 W Si target power is optimum for the crystal characteristics of the material. This result is consistent with those of Schifano et al. [90].

4.2.3 AFM Results

To investigate the topography and roughness of the samples, AFM was employed. The transmittance of the films can be linked to the surface topography as different surfaces will scatter the light differently. From the AFM images, the horizontal grain size can be assessed (note that this is different from the vertical grain size obtained in the XRD). In table 4.2, the average roughness of the different films is displayed. The roughness is around 5 nm for most of the samples, but the ZnO reference has a roughness of almost 9 nm. By examining figure 4.5, it can be seen that the lateral grain size of the undoped film is also larger than that in the Si doped ones, indicating that grain growth of in the lateral direction is easier for the undoped film. The vertical grain size as determined by XRD of Si doped ZnO is highest for the film deposited with a 12 W Si target power, and it seems as if the presence of Si in the material produces a material with less defects along the c-axis (the presence of structural defects is what limits the vertical grain size of the material). This suggests that the surface mobility of the elements of the films are inhibited by the presence of Si. Since an inhibition of adatom surface mobility promotes growth of smaller islands which will create less defects in the material [91], this points to a surfactant action of Si. At lower Si target powers, the surface roughness is higher, suggesting that the surfactant action is maintained and amplified with higher Si content. A very rough estimate from figure 4.5 (b), yields a lateral grain size of $10^1 - 10^2$nm. The roughness of the sample deposited with 25 W Si target power appears to be similar to the rest of the films, but by examining figure 4.5 it is evident that the film is structurally considerably different, and the roughness of the 25 W Si sample can not be compared to the rest of the films.

The AFM results show that doping the films with Si may inhibit the surface mobility of the elements in the films since the lateral grain size seems to be larger for the undoped than the doped films. Furthermore, the 25 W sample is structurally different from the other samples, underlining the difference of this sample compared to the other films, as also unveiled by

Sample	Roughness (nm)
ZnO reference on glass	8.9 ± 1.2
7 W Si on glass	4.5 ± 0.1
10 W Si on glass	5.3 ± 0.2
12 W Si on glass	3.9 ± 0.2
15 W Si on glass	4.1 ± 0.1
25 W Si on glass	5.0 ± 0.4

Table 4.2: The average roughness of the samples.

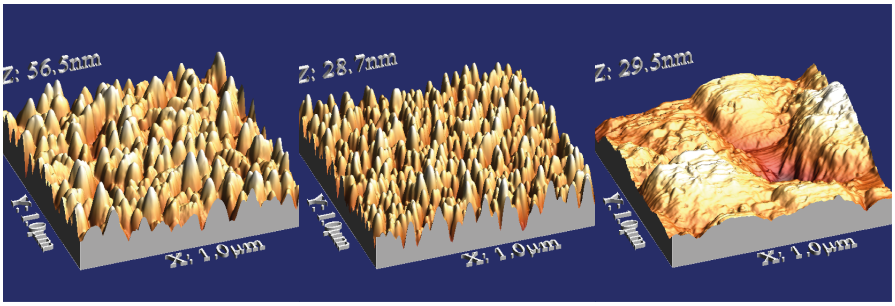

(a) (b) (c)

Figure 4.5: AFM images of (a) the ZnO reference sample, (b) the 12 W Si sample and (c) the 25 W Si sample. The lateral grain size of the undoped sample is larger than the sample with a 12 W Si target power. The 25 W Si sample is seen to be structurally different than the other samples.

XRD.

4.2.4 Hall Effect Measurement Results

The electrical properties (carrier density, mobility and resistivity) of the films as a function of Si target power was determined using Hall effect measurements. Contacts to the samples were made by soldering In onto the corners of the samples using Ag wires. The size of the In contacts varied from 0.7-2.1 mm in diameter.

In figure 4.6, the resistivity, carrier density and mobility of the samples as a function of Si target power are shown. Only the samples with 7 W, 10 W, 12 W, 15 W and 25 W Si target power are displayed, since the undoped sample was too resistive and yielded inconsistent data. Doping with Si increases the electron density suggesting that Si acts as a donor or promotes the formation of intrinsic or extrinsic defects that act as donors. This increase in carrier density leads to a dramatic decrease of resistivity from the highly resistive, undoped film to the $10^{-3}\Omega$cm-range for the doped samples. At high Si concentration (25 W Si target power), the resistivity increases significantly, probably due to both a lower carrier density and a lower mobility. This suggests that the high Si content in the sample with a 25 W Si target power leads to a degradation of the lattice through the formation of defects. As seen in section 4.2.2, the 25 W Si sample has a low crystal quality, and the Hall effect measurements thus support the result obtained by XRD. In figure 4.6, the resistivity is seen to decrease with higher target power up to 12 W where the resistivity reaches its lowest point. At higher target powers, the resistivity increases again. In the figure, the carrier density and the mobility are also shown and the decreasing resistivity is due both to a higher carrier concentration as more dopants are added to the films and to a higher mobility indicating a better crystal quality. Above 15 W, both the carrier density and the mobility decrease, most likely due to a degraded crystal quality as observed by XRD.

In summary, the minimum resistivity is obtained at intermediate Si concentrations, and a target power on Si of 12 W seems to yield the best results. This is consistent with the XRD data of section 4.2.2 and the previous work of Schofield [49] and Schifano et al. [90].

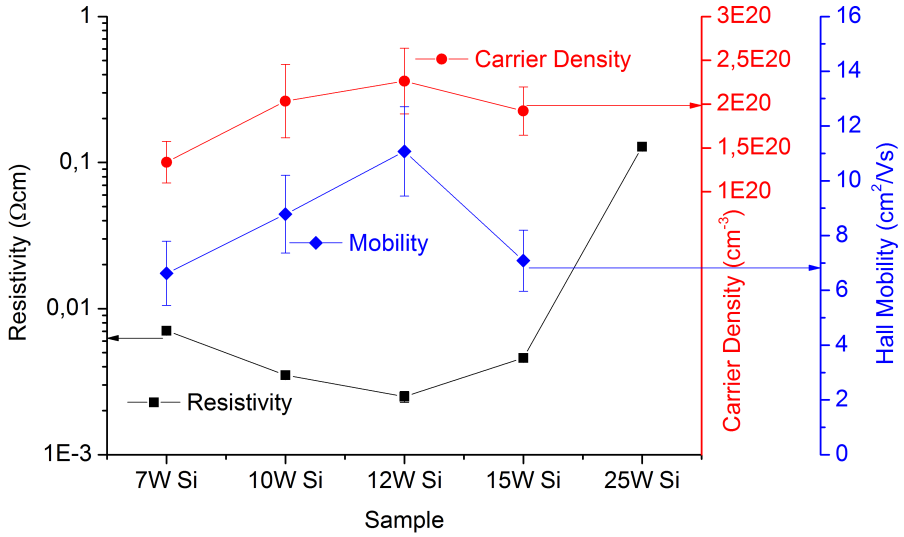

Figure 4.6: The electrical properties as a function of Si target power. The resistivity decreases with higher Si target power up to 12 W and then increases at yet higher powers. The decrease is due to a higher mobility and carrier density, while the higher resistivity at high powers is due to a decrease of carrier density and mobility.

4.2.5 Transmittance Measurement Results

As a TCO, Si doped ZnO needs to be transmittive in the visible range, and to investigate this property, transmittance measurements were employed. Figure 4.7 shows the transmittance of the different films as a function of wavelength of the probing light. The glass substrate is shown in the figure and the measured transmittance of the deposited films are naturally affected by the substrate, since the light must travel through both the film and the substrate to reach the detector. All the films except the one deposited with 25 W Si target power show similar transmittance in the visible range with more than 80% transmittance above 460 nm, even reaching a transmittance of 91% in the 540-600 nm wavelength range. This is comparable to values reported in literature for the more studied Al doped ZnO (AZO) [92]. The film deposited with 25 W Si target power has a transmittance below 80% in the visible range, and the low values may be related to its surface topography as seen by AFM or its amorphous nature. In the near infrared (NIR) range (750-1400 nm), the 12 W Si sample shows the highest transmittance, and this may reflect the crystal quality of the sample. In the short wavelength IR wavelength (SWIR) range (1400-3000 nm), the films show a lower transmittance, and a trend can be seen; the transmittance decreases with Si target power from the undoped reference film to the 12 W Si sample and then increases again with the 15 W and 25 W Si sample. The low transmittance in this region occurs when photons are reflected due to plasmon interference. Plasmons are quantizations of plasma oscillations (in this case, the plasma is due to the conduction band electron gas), and with more electrons in the material, the plasmon frequency is shifted to lower wavelengths [93]. The observed transmittances are therefore a direct confirmation of the carrier densities extracted from the Hall effect measurements since it can be seen that the region of low transmittance due to plasmon interference is shifted to lower wavelengths for the samples with a high carrier density.

Below 460 nm, the transmittance drops dramatically as this is the onset of band to band

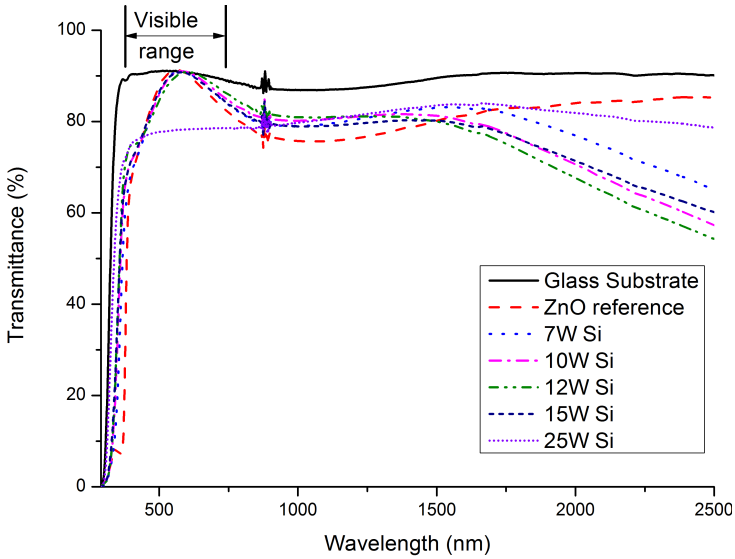

Figure 4.7: The transmittance of the different films. The gradual decrease of transmittance in the infrared from the ZnO reference to a Si target power of 12 W is due to plasmon interference. This plasmon interference is shifted to lower wavelengths as more carriers are added to the material. The blue-shift seen at $\sim$ 300 nm from the ZnO reference to the doped samples is the Burstein-Moss effect where the optical band gap is increased as the semiconductor becomes degenerate.

excitations and absorption is high. A blue-shift can be seen from the undoped ZnO sample to the doped films. Degenerate semiconductors have occupied electron levels at the band edge, and an electron excited radiatively across the band gap needs more energy to find the lowest available state than in a non-degenerate semiconductor where there are available states at the band edge. This will increase the optical band gap and cause a blue-shift in the transmittance spectra. The increase is known as the Burstein-Moss effect. Using the method outlined in section 3.4, the band gap for the undoped sample is estimated to 3.3 eV$\pm$0.2 eV while the 12 W Si sample has an estimated band gap of 3.5 eV$\pm$0.1 eV and this difference indicates that the doped samples are degenerate. The error margins were obtained from the standard deviations of the curve fitting.

In summary, a high transmittance occurs in the visible region, and features in the SWIR and near UV regions confirm the Hall effect results. The XRD data are also supported as the 12 W Si sample exhibits the highest transmittance in the visible and NIR regions, while the 25 W Si sample has a significantly different optical behaviour than the other films.

4.2.6 TEM Results

The structural characteristics of the samples were also investigated by TEM. The TEM examination was performed at NTNU in Trondheim by Dr. Ragnhild Sæterli, and only a 12 W Si film deposited on Si + SiO_2 was investigated.

Figure 4.8 shows a micrograph and a Selected Area Diffraction (SAD) pattern of the film. From the micrograph, the polycrystalline nature of the film can be seen. The lateral size of the grains can be estimated, and appears to be somewhere between 20-50 nm, and this result is comparable to the lateral grain size obtained from the AFM analysis of the 12 W Si sample

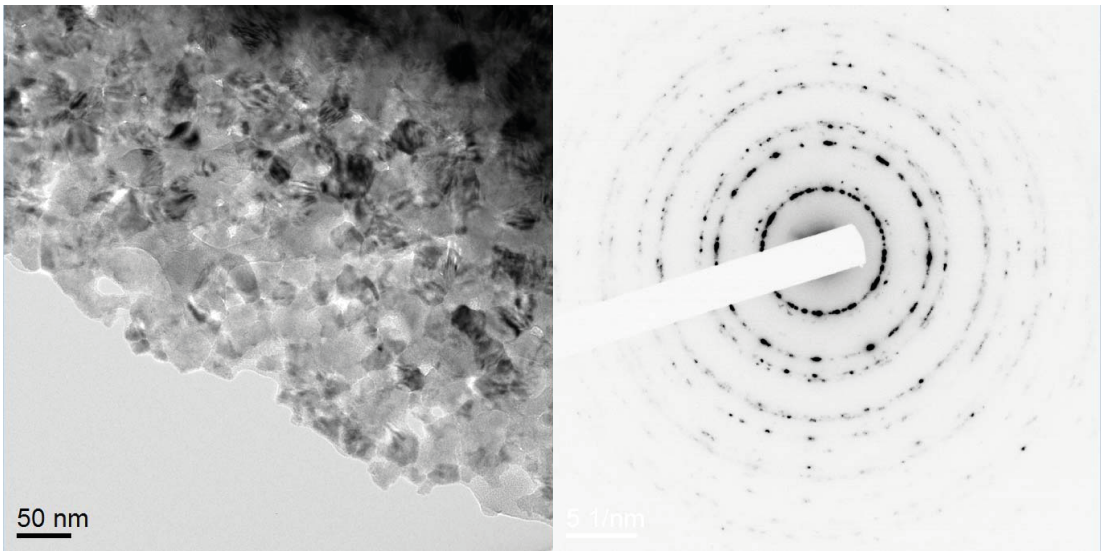

(a) (b)

Figure 4.8: (a) A transmission electron micrograph of a 12 W Si sample on Si + SiO_2. (b) SAD pattern of a 12 W Si sample on Si + SiO_2.

deposited on glass. It confirms the result stating that the lateral grain size is larger than the vertical grain size supporting the surfactant action of Si. The analysis by Dr. Sæterli states that the films are polycrystalline with a significant number of grains being amorphous and this explains the low XRD signal exhibited by the films deposited on Si + SiO_2. It can only be speculated as to the origin of this amorphous nature of the grains, but different nucleation mechanisms for different grains could lead to such a film, keeping in mind that the SiO_2 substrate is amorphous.

4.2.7 Summary

To determine the Si target power yielding the optimum characteristics of the Si doped ZnO films, Hall effect measurements, XRD, transmittance measurements, AFM and TEM were utilised. XRD, AFM and TEM investigations provided evidence that Si acts as an surfactant limiting the surface mobility of adatoms during film growth. Hall effect measurements indicated that the best electrical characteristics were achieved with a 12 W Si target power. The same target power also gave the largest grain size and among the lowest stress. Transmittance of the films were high, and AFM proved that a Si target power of 12 W produced the best films in terms of surface roughness. This is a similar result as previously obtained by Schofield [49] and Schifano et al. [90]. The TEM data for a 12 W Si sample on Si + SiO_2 revealed that the sample was polycrystalline, but also that some grains were amorphous.

4.3 Temperature Series

For ZnO to be successfully employed as a TCO, it needs to match the resistivity exhibited by ITO, and although the optimum sputtering parameters determined in section 4.2 produce low resistive films, they are inferior to ITO [31]. The resistivity can be reduced in two ways,

either by increasing the carrier density or the mobility. The doping density can not be raised significantly from the 1.5 at.% of the 12 W Si sample as the crystal quality degrades at higher powers. A 1.5 at.% content of Si suggests a carrier density above 10^{21}cm^{-3} (i.e., in reality only around 20% of the Si atoms effectively contribute to the doping) and a higher concentration of dopants needs to be activated electrically or the concentration of compensating defects must be decreased. Furthermore, the mobility in a polycrystalline sample (like the sputtered films in question) is significantly limited by the grain boundaries and crystal defects. By increasing the grain sizes and restoring the lattice a higher mobility could thus be achieved.

Thus, to realise a higher carrier density and mobility, post-deposition annealing was utilised. By heat treating the samples, the atoms in the material will gain a higher mobility and can move through the lattice more easily and settle in more energetically favourable positions possibly reducing the number of compensating and structural defects. Si atoms can thus settle in lattice positions where they will donate electrons and the number of electrically active dopants will increase. Zn and O atoms can also move through the lattice and settle in correct lattice positions resulting in crystal defects being annealed out. This will improve the crystal quality, increase the grain size and ultimately increase the electron mobility. Furthermore, by increasing the mobility of the atoms, Si atoms would have a greater probability of clustering and creating Si nanocrystals. To this end, films deposited with different sputtering parameters were annealed at 550°C, 650°C, 800°C, 950°C, 1050°C, 1100°C and 1200°C in air. Several different sputtering parameters and substrates were combined, and an overview of the prepared samples are presented in table 4.3. All the samples were deposited at 400°C with 70 SCCM Ar flow, 50 W ZnO target power and 12 rpm rotation speed. The Si + SiO_2 substrate was chosen because of the high thermal stability compared to glass, but also a Si substrate was used due to the low crystal quality of the films deposited on Si + SiO_2. However, it proved difficult to get reliable Hall measurements with Si as a substrate since the resistivity of the substrate was comparable to the resistivity of sputtered films (leading to a significant contribution to the measured signal from the substrate), and quartz was used for samples # 15 - # 32. The as-deposited samples listed in table 4.3 were not heat treated and were characterised together with the annealed samples.

4.3.1 Surfactant Action of Si and Al

4.3.1.1 XRD Results

As in section 4.2, the structural characteristics of the samples were investigated by XRD. Generally, by annealing, the grain size and the stress in the films increased.

This is the case for the films displayed in figure 4.9 where the grain size of samples # 15 - # 32 (samples on quartz) are seen. The doped samples have little increase in grain size at low annealing temperatures (below 800°C) and significant increase at high temperatures (above and at 800°C). The undoped samples however, have an increase in grain size already at 550°C. The presence of Al and Si in the films thus inhibits grain growth at low annealing temperatures, and this provides further evidence that Si and Al act as surfactants and lower the mobility of Zn and O. It is consistent with the model of Kandel and Kaxiras [91] where the surfactant action is maintained up to a critical temperature, above which the surfactant action is lost. However, the grain size of the undoped as-deposited film is higher compared to the doped as-deposited samples and this result contrasts the data from section 4.2.2 where the grain size of the 12 W Si sample is higher than the reference ZnO sample. The films

Sample identity	Substrate	Si target power	Al target power	Annealing temperature	Thickness	Notes
# 1	Si + SiO_2	12 W	0 W	As-deposited	143±2 nm	–
# 2	Si + SiO_2	12 W	0 W	650°C	143±2 nm	–
# 3	Si + SiO_2	12 W	0 W	950°C	143±2 nm	–
# 4	Si + SiO_2	12 W	0 W	As-deposited	143±2 nm	–
# 5	Si + SiO_2	12 W	0 W	1100°C	143±2 nm	–
# 6	Si + SiO_2	12 W	0 W	1100°C	143±2 nm	$\sim$ 240 nm of SiO_2 was deposited on top of the sample to prevent the exchange of oxygen with the ambient
# 7	Si + SiO_2	12 W	0 W	1200°C	143±2 nm	–
# 8	Si + SiO_2	12 W	0 W	1200°C	143±2 nm	$\sim$ 240 nm of SiO_2 was deposited on top of the sample to prevent the exchange of oxygen with the ambient
# 9	Si + SiO_2	15 W	0 W	As-deposited	283±5 nm	–
# 10	Si + SiO_2	15 W	0 W	650°C	283±5 nm	–
# 11	Si + SiO_2	15 W	0 W	950°C	283±5 nm	–
# 12	Si	12 W	0 W	As-deposited	–	–
# 13	Si	12 W	0 W	650°C	–	–
# 14	Si	12 W	0 W	950°C	–	–
# 15	Quartz	12 W	0 W	As-deposited	569±2 nm	–
# 16	Quartz	12 W	0 W	550°C	569±2 nm	–
# 17	Quartz	12 W	0 W	650°C	569±2 nm	–
# 18	Quartz	12 W	0 W	800°C	569±2 nm	–
# 19	Quartz	12 W	0 W	950°C	569±2 nm	–
# 20	Quartz	12 W	0 W	1050°C	569±2 nm	–
# 21	Quartz	0 W	7 W	As-deposited	568±5 nm	–
# 22	Quartz	0 W	7 W	550°C	568±5 nm	–
# 23	Quartz	0 W	7 W	650°C	568±5 nm	–
# 24	Quartz	0 W	7 W	800°C	568±5 nm	–
# 25	Quartz	0 W	7 W	950°C	568±5 nm	–
# 26	Quartz	0 W	7 W	1050°C	568±5 nm	–
# 27	Quartz	0 W	0 W	As-deposited	550±13 nm	Undoped ZnO reference sample
# 28	Quartz	0 W	0 W	550°C	550±13 nm	Undoped ZnO reference sample
# 29	Quartz	0 W	0 W	650°C	550±13 nm	Undoped ZnO reference sample
# 30	Quartz	0 W	0 W	800°C	550±13 nm	Undoped ZnO reference sample
# 31	Quartz	0 W	0 W	950°C	550±13 nm	Undoped ZnO reference sample
# 32	Quartz	0 W	0 W	1050°C	550±13 nm	Undoped ZnO reference sample

Table 4.3: An overview of the different annealed samples. Note that the thickness measurements were made prior to annealing, and that the films may have changed upon annealing.

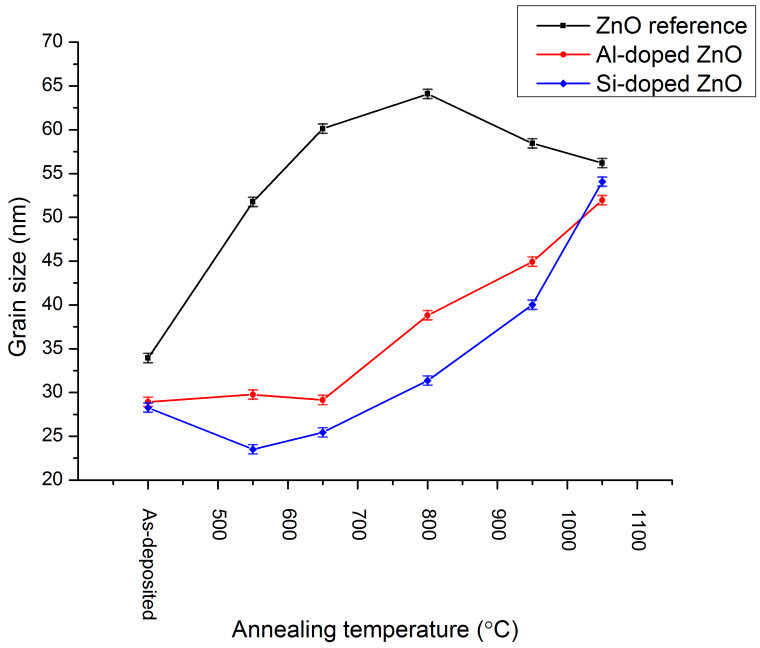

Figure 4.9: The grain size of samples # 15 - # 32. The grain size of the doped samples has little change at low temperatures and increases at higher temperatures. The undoped sample exhibits an increase already at 550°C.

deposited on quartz are significantly thicker (by a factor 4), and this is likely the cause of the discrepancy (suggesting that the number of structural defects decreases with film thickness).

4.3.1.2 AFM Results

The surfactant action of Si and Al is reflected in the AFM results of these films. In table 4.4, the roughness of the annealed films deposited on quartz is shown. An interesting feature of the data is the large roughness discrepancy between the undoped and the doped samples. This difference is again seen in the horizontal grain size of the samples as displayed in figure 4.10. This difference in horizontal grain size can probably be linked to the explanation of the lower grain size determined by XRD for the doped samples in section 4.3.1.1 and the lower lateral grain size of the undoped samples in section 4.2.3 where the mobility of Zn and O is suggested to be suppressed by the presence of Si and Al.

4.3.1.3 PL Results

Photoluminescence (PL) Spectroscopy supports the results obtained by XRD, as PL Spectroscopy gives evidence that the crystal quality improves directly for the undoped samples, while the doped samples have a delayed "response" to the annealing.

Samples # 15 - # 32 were investigated, and the spectra for the undoped samples are shown in figure 4.11. Around 375 nm, the near band edge emission occurs (emission due to band-to-band relaxation), and the intensity of the peak increases with annealing temperature up to 800°C and then decreases again. A high intensity of the near band edge emission is indicative of a higher crystal quality since more band-to-band relaxation implies less defect

Sample	Roughness (nm)
Si doped as-deposited	8.7 ± 0.1
Si doped annealed at 550°C	8.6 ± 0.1
Si doped annealed at 650°C	8.9 ± 0.1
Si doped annealed at 800°C	9.0 ± 0.3
Si doped annealed at 950°C	11.9 ± 0.2
Si doped annealed at 1050°C	20.1 ± 1.7
Al doped as-deposited	8.6 ± 0.2
Al doped annealed at 550°C	8.5 ± 0.3
Al doped annealed at 650°C	9.1 ± 0.3
Al doped annealed at 800°C	9.9 ± 0.3
Al doped annealed at 950°C	14.2 ± 1.3
Al doped annealed at 1050°C	13.7 ± 0.4
Undoped as-deposited	15.1 ± 0.3
Undoped annealed at 550°C	15.4 ± 1.1
Undoped annealed at 650°C	14.5 ± 1.9
Undoped annealed at 800°C	15.8 ± 1.7
Undoped annealed at 950°C	20.5 ± 2.0
Undoped annealed at 1050°C	28.3 ± 2.7

Table 4.4: The average roughness of the annealed samples on quartz.

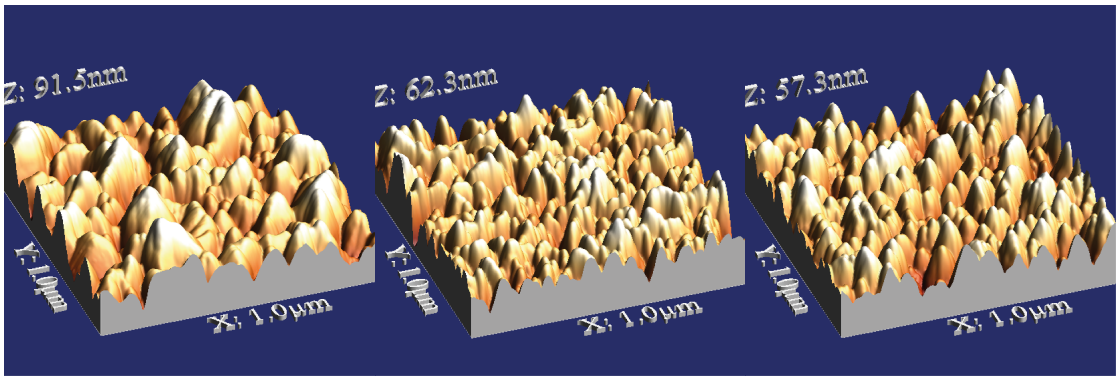

(a) (b) (c)

Figure 4.10: The different surface topography of the as-deposited samples on quartz. (a) Undoped, (b) Si doped, (c) Al doped.

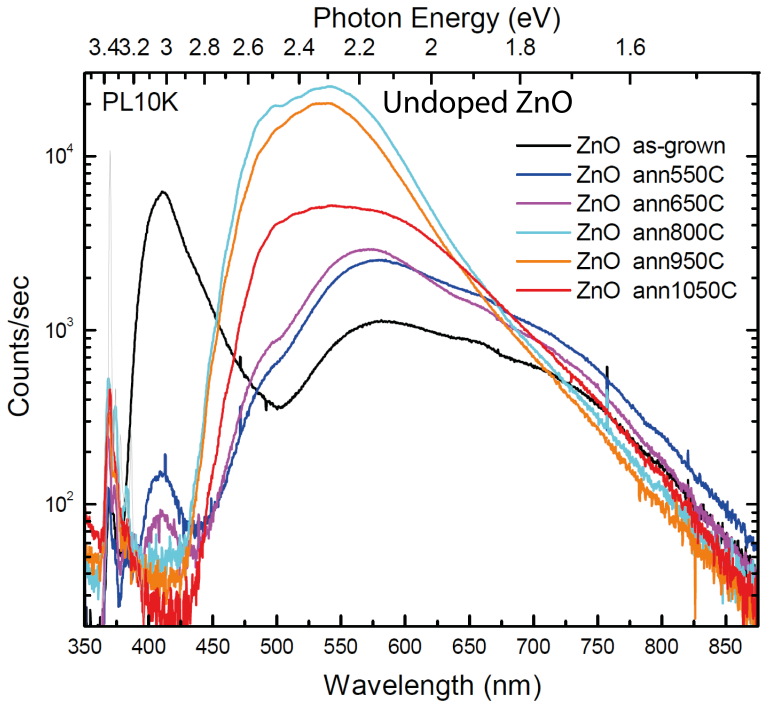

Figure 4.11: The PL spectra of the undoped, annealed samples on quartz. The peak around 375 nm is due to near band edge emission.

mediated relaxation and thus less defects. The evolution of the intensity of the 375 nm peak confirms the XRD data from section 4.3.1.1 where the grain size (which indicates the crystal quality of a material) increases up to 800°C. The near band edge emission intensity shows a maximum at 800°C indicating a higher crystal quality for this film than the others.

As seen in figure 4.12, both the Si doped and Al doped films have a maximum intensity of the near band edge emission peak at 1050°C. This is in accordance with the grain size and (002) peak intensity which both reach their maximum at 1050°C. Further, the near band edge emission is very low for the samples annealed below 800°C while it gradually increases with annealing temperature above this point. The PL spectra thus directly confirm the XRD results of section 4.3.1.1 and support the surfactant action of Si and Al.

The total integrated photoluminescence intensity is possibly also a measure of the crystal quality of the samples since more PL intensity means less non-radiative recombination and possibly less defects. Under this assumption, it is clear that the total integrated PL intensity conforms with the XRD data since the samples giving the highest total intensity also give the best signals and largest grain sizes in the XRD spectra, although the difference between the total integrated PL intensity of the as-deposited, doped samples and the annealed, doped samples in figure 4.13 is large (a difference not seen in XRD). The doped films have their highest total integrated PL intensity after annealing at 1050°C, and the undoped material for the film annealed at 800°C. The trend in figure 4.13 mostly follows the grain size of the XRD data, and confirms the data of the XRD analysis.

The results from XRD, AFM and PL analysis of the annealed samples as well as the results from the power series thus all support that Si and Al inhibit the mobility of Zn and O and this is consistent with the predictions of Kandel and Kaxiras [91].

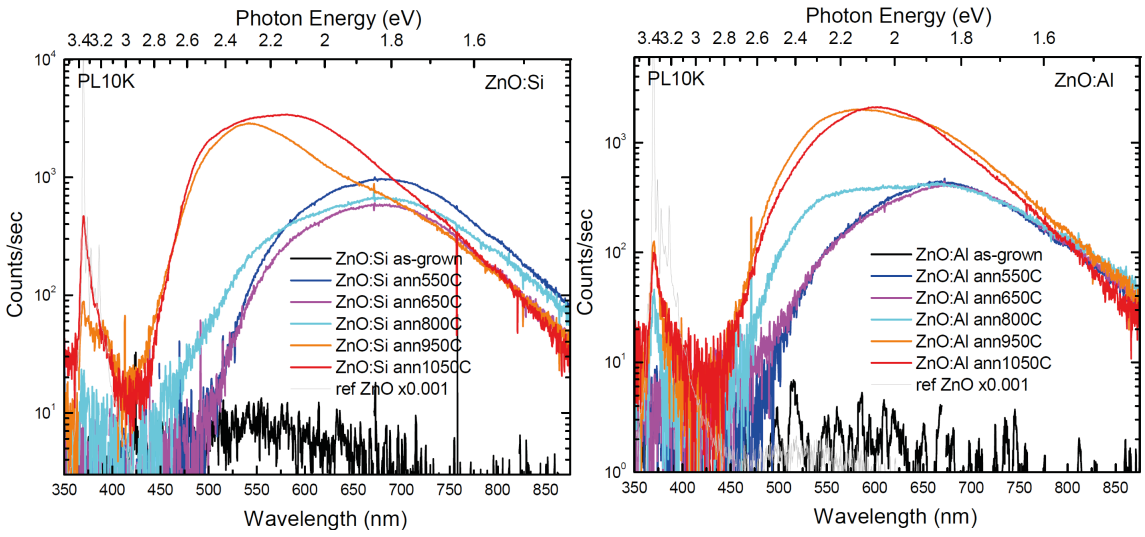

Figure 4.12: (a) The PL spectra of the Si doped, annealed samples on quartz. (b) The PL spectra of the Al doped, annealed samples on quartz. The ref ZnO×0.001 spectrum is that of monocrystalline, bulk ZnO.

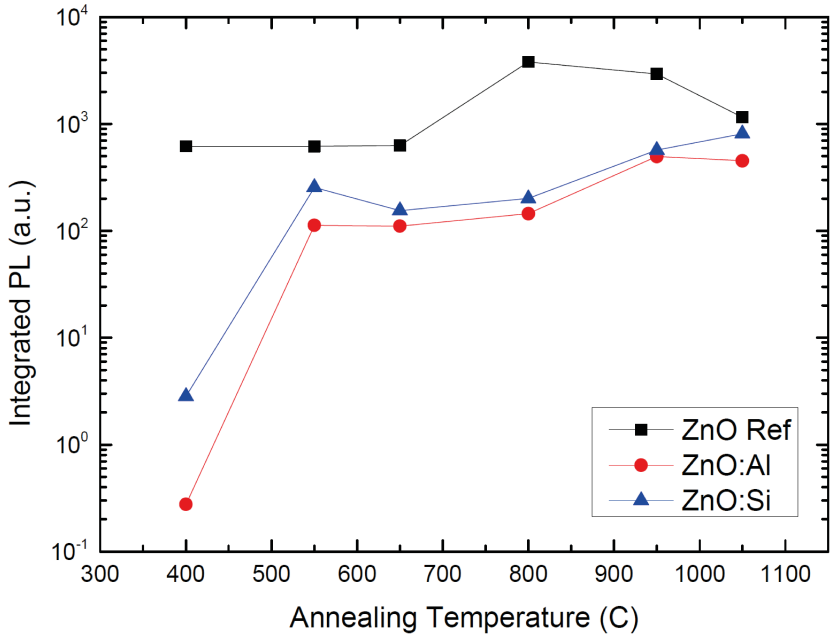

Figure 4.13: The total integrated photoluminescence intensity of samples # 15 - # 32. The highest total integrated intensity possibly indicates the film with the highest crystal quality.

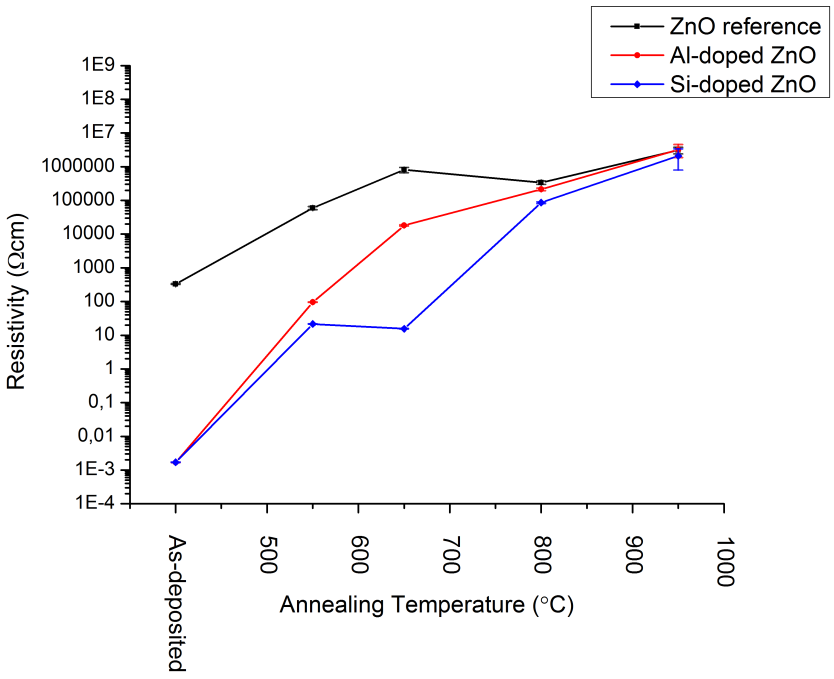

Figure 4.14: The resistivity of the samples annealed on quartz. The resistivity increases upon annealing, possibly due to chemisorption of oxygen at the grain boundaries and formation of V_{Zn} and O_i.

4.3.2 Resistivity of Annealed ZnO Films

4.3.2.1 Hall Effect Measurement Results

One of the aims of post-deposition annealing was to increase the mobility and raise the concentration of electrically active dopants in the samples. To determine these two quantities as well as the resistivity, Hall effect measurements were employed on the samples with an exception of samples # 12, # 13 and # 14 as well as samples # 6 and # 8 which had a SiO_2 layer on top of the films, making contacting challenging. With no exceptions, the resistivity of the films significantly increased when annealing, and this increase seems to come from a lower carrier density.

Samples # 15 - # 32 were all deposited on quartz. Si doped, Al doped and undoped samples were produced to investigate the effect of doping on the samples. In figure 4.14, the resistivity of the samples are shown.

Upon examining the figure, it can be seen that the resistivity increases significantly when annealing. Although few of the the samples give reliable carrier density values (hence the few data points in figures 4.15 and 4.16), at least the Si doped and Al doped samples increase in resistivity from the as-deposited state to the annealed state at 550°C through a lower carrier density. The decrease in carrier density is most likely due to a chemisorption of Oxygen at the grain boundaries increasing the number of electron traps and reducing the number of conduction band electrons (cf. section 2.4.3) and through the compensating, intrinsic acceptors V_{Zn} and O_i [15, 61]. Although no data on the carrier density of the samples annealed above 650°C can be trusted, it can be speculated that the large increase in resistivity for all the

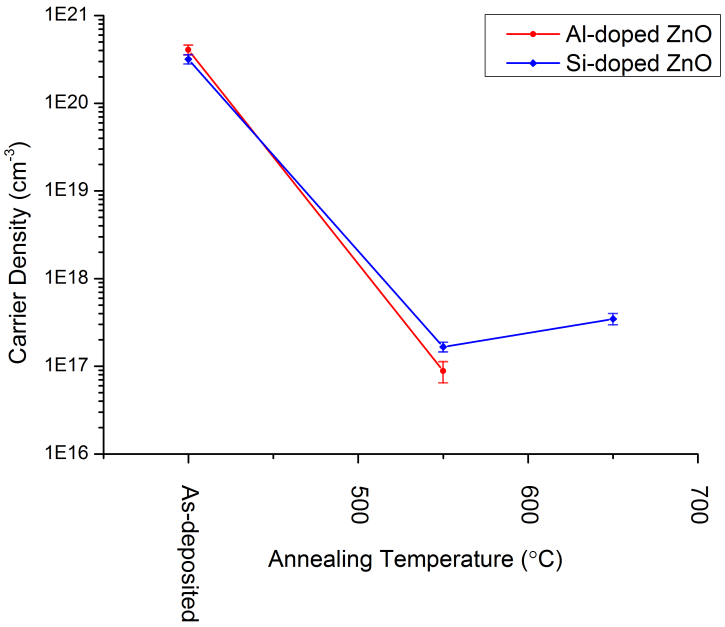

Figure 4.15: The carrier density of the samples annealed on quartz. The carrier density decreases when annealing.

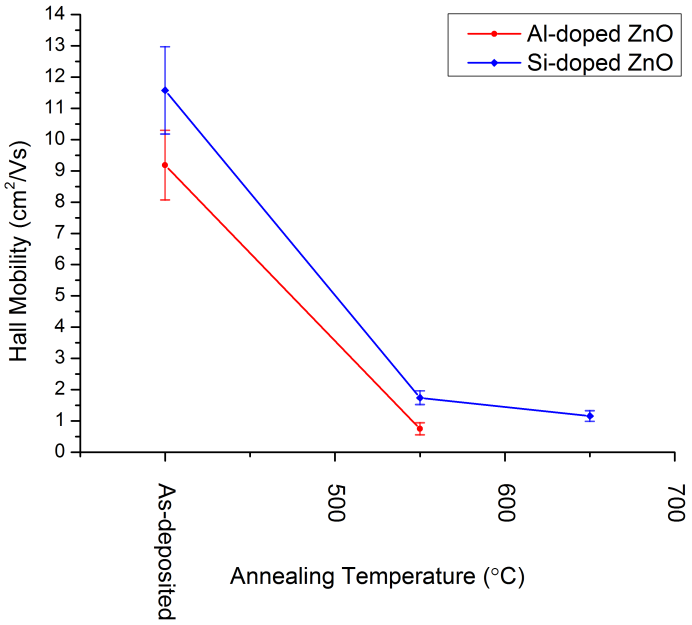

Figure 4.16: The mobility of the samples annealed on quartz. The mobility is decreased when annealing, possibly due to more charge at the grain boundaries leading to more scattering of electrons.

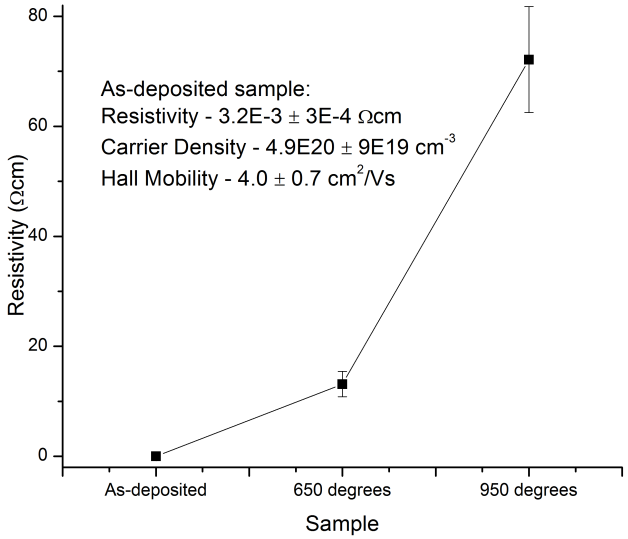

Figure 4.17: The resistivity of the samples deposited on Si + SiO_2 with a 12 W Si power (samples # 1, # 2 and # 3) with the carrier density and mobility of sample # 1 displayed. The samples get an increase in resistivity most likely due to a decrease in carrier density when annealing them.

samples stems from a decrease in carrier density (as a decrease of 9 orders of magnitude in the mobility is rather unlikely). Assuming this, the carrier density is steadily decreased for all the samples, but between 550°C and 650°C for the Si doped sample, there is little change in carrier density contrasting the undoped and Al doped samples which both have an increase in resistivity. The reason for this behaviour is not clear, but it is evident that the response of ZnO to annealing is affected by the doping.

The mobility decrease when annealing at low temperatures (figure 4.16) for the doped samples can be explained as a higher grain boundary charge density with more Oxygen chemisorption leading to more scattering at the grain boundaries as well as an increase of the bulk charge density from the compensating V_{Zn} and O_i defects leading to more impurity scattering. The decrease provides strong evidence that the decrease in carrier density is due to compensating defects (Oxygen chemisorption, formation of V_{Zn} and O_i) and not due to passivation of existing defects. The Si doped samples do not show a change in mobility from 550°C to 650∘C and looking at figure 4.15, a possible explanation can be put forward; the Si doped samples have no reduction in carrier density between 550°C and 650°C, and following the explanation of higher defect density at the grain boundary, no change in carrier density indicates no change in chemisorbed Oxygen and no change in mobility.

Interestingly, several of the annealed films exhibit p-type conductivity in the Hall effect measurements, and this result is further discussed in section 5.2

Figure 4.17 displays a summary of the electrical properties of samples # 1, # 2 and # 3. The samples exhibit increased resistivity by annealing, and this is consistent with the data from the samples on quartz.

Samples # 10 and # 11 were deposited on Si + SiO_2 with a higher Si target power, but the same resistivity trends are observed (cf. figure 4.18). The carrier density decreases with annealing as for the samples deposited on quartz, and the mobility is reduced. This follows

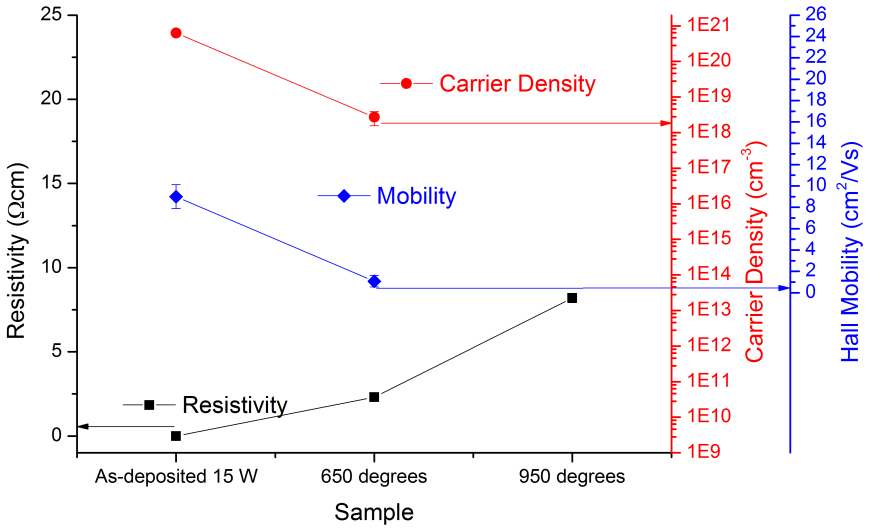

Figure 4.18: The resistivity, carrier density and mobility of the samples deposited on Si + SiO_2 with a 15 W Si power (samples # 9, # 10 and # 11). The same resistivity and carrier density trends are seen as in samples #1, # 2 and # 3. The mobility, however, is reduced. This could be due to a higher defect density at the grain boundaries. The as-deposited sample has a resistivity of $1.1\times10^{-3}\Omega$cm.

the explanation of more interface charge from chemisorbed Oxygen and more bulk charge from compensating defects. Another interesting feature of the results is the low resistivity of the as-deposited sample. The resistivity is $1.1\times10^{-3}\Omega$cm, a factor 7 lower than for a corresponding sample deposited 8 months prior, and comparable to the resistivities achieved for the best samples on glass and quartz. The reason for the discrepancy between the different depositions is not evident, but Secondary Ion Mass Spectrometry (SIMS)[1] measurements show that the Si content in the as-deposited sample is a factor 4 lower than the corresponding sample in section 4.2. The higher Si content of the sample deposited in January 2012 (section 4.2) does not lead to a higher carrier concentration, and the difference in resistivity seems to be related to structural properties.

Although few samples give reliable carrier densities and mobilities, it is clear that the resistivity increases upon annealing. This is most likely due to a decrease in carrier density through Oxygen chemisorption at the grain boundaries creating electron traps and through increased formation of the compensating V_{Zn} and O_i defects. The mobility is also decreased by annealing, possibly through a higher charge density at the grain boundaries when Oxygen chemisorbs to the interface and a higher charge density in the bulk from the compensating V_{Zn} and O_i defects.

4.3.2.2 XRD Results

The effect of annealing on the structural characteristics has already been partly discussed in section 4.3.1.1 where annealing leads to an increase in grain size for samples #15 - # 32. This

[1]SIMS is an analysis technique where atoms are sputtered off the surface of a sample. These sputtered atoms are separated and measured in a mass spectrometer, and the concentration of different elements in a sample can be detected.

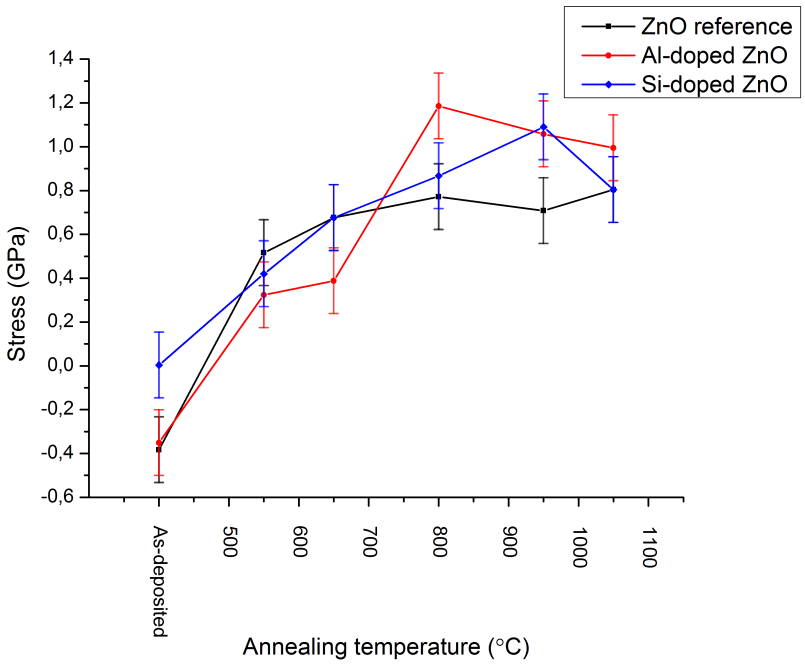

Figure 4.19: The stress of samples # 15 - # 32 (the samples deposited on quartz). The stress increases with annealing temperature and seems to saturate at around 1 GPa.

is indicative of an improvement of the crystal quality of the films, and this improvement is further supported by the intensity of the (002) peak of ZnO which increases with annealing temperature for both the doped and undoped samples.

The stress increases with annealing for all the films, although it seems to stabilise at around 1 GPa and changes from compressive to tensile (figure 4.19). The stress increase may be related to a recrystallisation/rearranging of the lattice. The crystal quality is seen to improve for all the samples of table 4.3 with increasing temperature with the highest intensity of the XRD signal from the 1050°C samples. This is interesting since samples # 6 - # 8 give no discernible (002) ZnO peak in the $\theta/2\theta$ spectra (cf. figure 4.20). Only sample # 5 of the ones deposited on Si + SiO_2 and annealed at a temperature above 1050°C exhibits a peak. This sample gives a large grain size of 70±2 nm and a stress of 0.85±0.15 GPa. The spectra of sample # 6 - # 8 can not be used for extraction of these properties as the (002) peak is absent. Instead of a strong (002) ZnO reflection, the Grazing Incidence XRD[2] spectra show several peaks which can not be related to ZnO, and the films seem to have changed phase from ZnO to Zinc Silicate (most likely). This means that the Si-doped films has a change of phase upon annealing somewhere in the temperature range 1050°C−1200°C.

The grain size and stress trends seen for the Si doped samples on quartz are also reflected in the samples on SiO_2 and Si. In figure 4.21, the grain size and stress of samples # 1, # 2, # 3, # 12 # 13 and # 14 are shown. The absolute value of the stress increases by annealing, and the stress changes from compressive to tensile for the films deposited on Si + SiO_2 (samples # 1, # 2 and # 3). The grain size also increases, although primarily only for the 950°C samples,

[2]Grazing Incidence XRD is a technique where the probing beam is incident at a very low angle. The X-ray source is kept constant at this low angle, while the detector is rotated. This will allow for detection of crystal planes not perpendicular to the surface, and more peaks can be gathered.

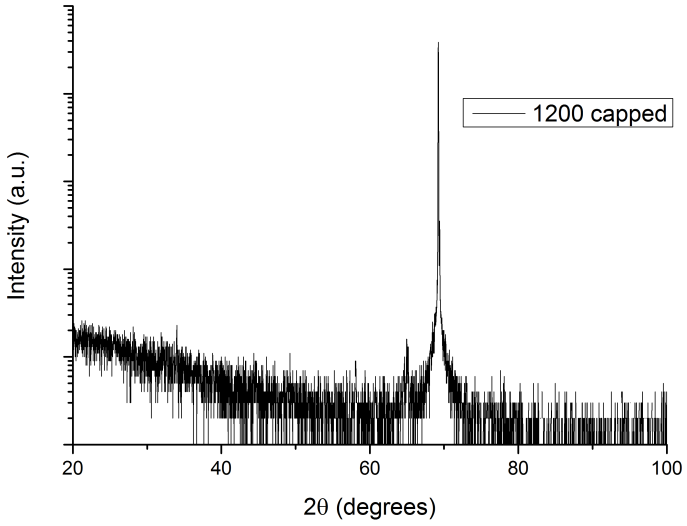

Figure 4.20: The $\theta/2\theta$ spectrum of sample # 8. No (002) ZnO peak is visible. The intensity follows a logarithmic scale.

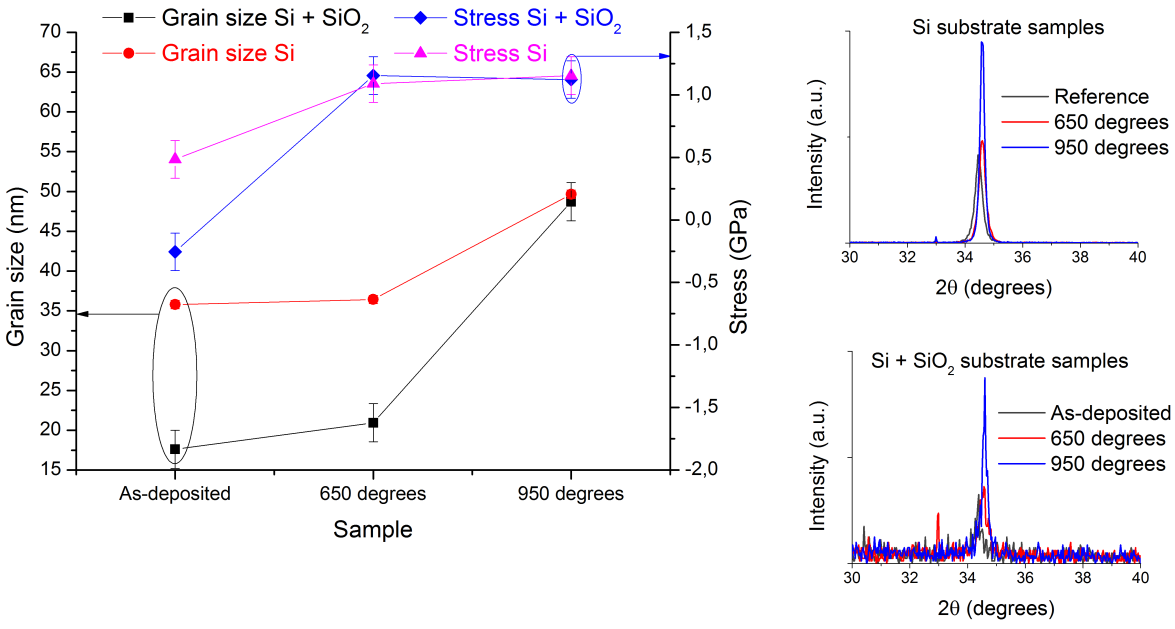

Figure 4.21: The grain size and stress of samples # 1, # 2, # 3, # 12, # 13 and # 14. Both the stress and grain size of the samples increase when annealing. All the annealed films have a tensile stress greater in absolute value compared to the as-deposited films. The figures to the right of the panel show the XRD spectrum around the (002) peak of the samples. The two figures are not directly comparable, while the intensities within each figure are.

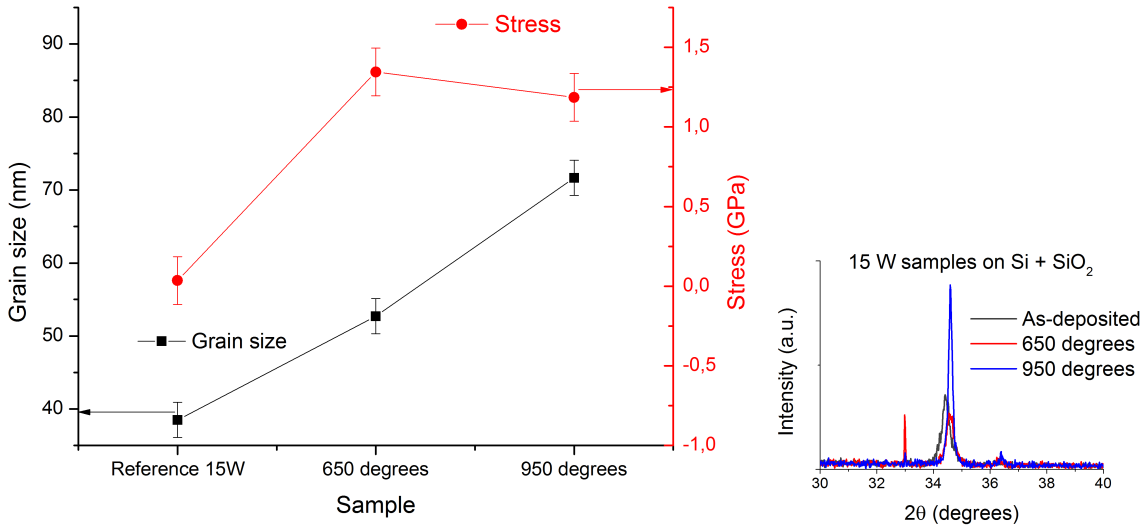

Figure 4.22: The grain size and stress of samples # 9, # 10 and # 11. The grain size increases gradually and reaches a very high value of 70 nm at 950°C. The stress increases from a low value around 0 GPa for the as-deposited sample to a value of around 1.3 GPa for the annealed samples. A (101) ZnO reflection can be seen in the right figure indicating that the films are not as higly texturised as the other annealed films.

where the grain size is close to 50 nm. This follows the trend of figure 4.9 where the grain size does not increase significantly at temperatures lower than 800°C and supports the mobility inhibiting action of Si in the films. The figures to the right of the panel show the intensities of the (002) peak of ZnO. The lower, right figure displays the peak of the samples on Si + SiO_2. The peak increases in intensity with annealing evidencing an improved crystal quality. Samples # 12, # 13 and # 14 (films deposited on Si) follow the usual trend of increased grain size and stress while the crystal quality improves.

The XRD data from samples # 9, # 10 and # 11 (films deposited on Si + SiO_2 with a 15 W Si target power) present a similar trend for the grain size and the stress as seen in figure 4.22. The stress increases with annealing and the crystal quality improves as previously, but the grain size is increased already at 650°C differing from samples # 2 and # 13 which show a grain size similar to the corresponding as-deposited samples. This implies that the critical temperature proposed by Kandel and Kaxiras [91] is lower for these particular films. Notice also that the grain size for the as-deposited sample in figure 4.22 is much higher than the grain size of the 15 W Si target power samples of section 4.2 as well as all other as-deposited samples on Si + SiO_2. Furthermore, the stress is very low compared to both the annealed samples in the figure and other as-deposited samples (such as the ones in section 4.2). This supports the low resistivity value given in figure 4.18 for the same sample, and the low resistivity may in fact be due to better structural properties. Comparing figures 4.18 and 4.22 further reveals that the mobility in these samples decreases upon annealing and is probably more affected by the higher defect density at the grain boundaries through Oxygen chemisorption than the better crystal quality achieved when annealing. This is consistent with the samples deposited on quartz.

XRD investigations of the structural characteristics of the annealed films reveal that the stress invariably increases while the crystal quality, as evidenced by grain size and (002) ZnO

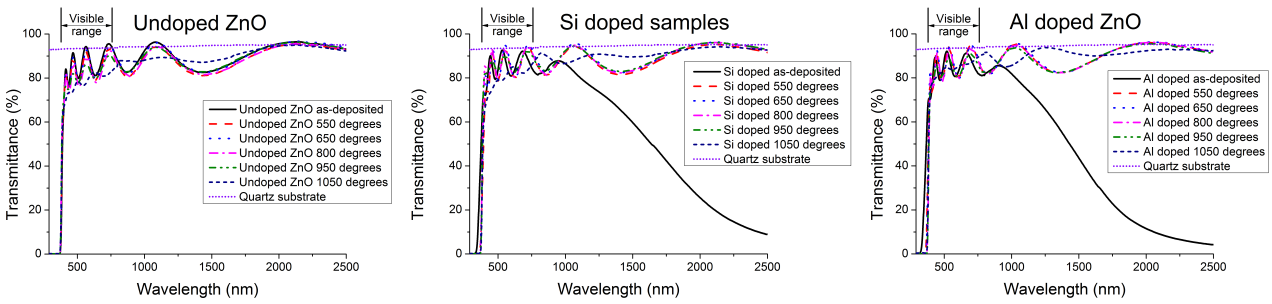

(a) (b) (c)

Figure 4.23: (a) The transmittance of the undoped, annealed samples on quartz. (b) The transmittance of the Si doped, annealed samples on quartz. Plasmonic interference and a Burstein-Moss shift can be seen for the as-deposited sample. (c) The transmittance of the Al doped, annealed samples on quartz. Plasmonic interference and a Burstein-Moss shift can be seen for the as-deposited sample. The oscillation of the transmittance in the visible and infrared range is due to destructive and constructive interference of reflected beams.

peak intensity, improves upon annealing. This improvement prevails up to a temperature of 1050°C−1200°C where the films undergo a phase change.

4.3.2.3 Transmittance Measurement Results

Due to the substrates used, the transmittance was only measured for samples # 15 - # 32 (films deposited on quartz). These samples on quartz reflect the properties of the samples on glass shown in section 4.7 in their high transmittance in the visible spectrum, plasmonic interference in the SWIR range for the samples with a high carrier density and Burstein-Moss shift around 300 nm.

The transmittance of the undoped, Si doped and Al doped films is displayed in figure 4.23 Except the film annealed at 1050°C, all the undoped films in figure 4.23 (a) show a similar behaviour. These films have a transmittance of above 80 % in the visible range with the as-deposited film exhibiting the highest. The difference between the 1050°C sample and the others are most likely due to a "collapse" of the film at 1050°C. This collapse could be brought on by a desorption of Zn from the films. The transmittance is seen to oscillate between around 80 % and 90 %, and this effect comes from a higher and lower reflectance at the surface of the film: When the film thickness is equal to $\frac{\lambda}{4}$, waves reflected at the film substrate interface interfere destructively with waves reflected at the air film surface reducing the reflectance and increasing the transmittance. When the film thickness is equal to $\frac{\lambda}{2}$, the waves interfere contructively increasing the reflectance and reducing the transmittance. The oscillation is due to the film thickness being equal to different modes of the incoming light.

The doped samples resemble the undoped samples with a high transmittance in the visible and NIR range and a lower transmittance for the 1050°C sample. However, the as-deposited samples have a low transmittance in the SWIR range and a blue shift around 300 nm. These features were explained in section 4.7 as plasmonic interference and the Burstein-Moss shift. In figure 4.23 (b) and (c), it is seen that all the doped, annealed films except the 1050°C films are similar with the 650°C samples narrowly having the best transmittance. In figure 4.24, the as-deposited samples are compared. Here, the Burstein-Moss shift from the undoped

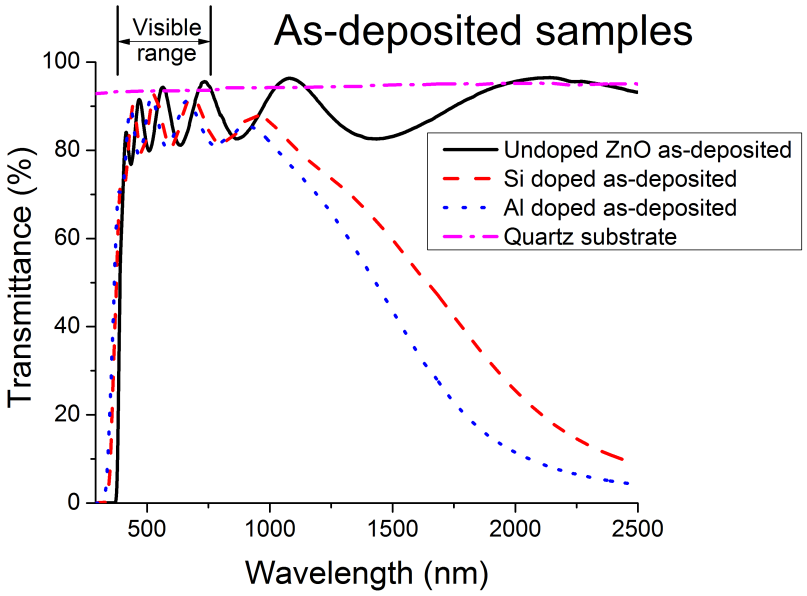

Figure 4.24: The transmittance of the as-deposited samples on quartz. The doped samples are degenerate which leads to a Burstein-Moss shift and plasmonic interference in the SWIR range.

sample to the doped samples is clearly seen. From the figure, the band gap of the material is estimated using the method outlined in section 3.4. The undoped, as-deposited sample has a band gap of 3.3±0.2 eV, the Si doped, as-deposited a band gap of 3.7±0.2 eV and the Al doped, as-deposited sample has a band gap of 3.8±0.1 eV. The doped, as-deposited films are thus degenerate, and the Al doped one has a higher carrier density than the Si doped one (cf. the larger band gap and more shifted plasmonic interference) and this confirms the data from figure 4.15 where the Al doped sample is seen to have a higher carrier density. The degeneracy of the as-deposited doped samples is further supported by temperature dependent Hall effect measurements in the temperature range 10-300K. In this range, the carrier density of the doped as-deposited samples does not change significantly and the samples are degenerate[3]. The undoped sample has furthermore a higher transmittance than the doped samples.

In conclusion, with the exception of the 1050°C samples, all the annealed samples show similar transmittance. The doped, as-deposited samples are degenerate, and the transmittance measurements support the Hall effect measurements of section 4.3.2.1.

4.3.2.4 AFM Results

The data in table 4.4 are difficult to link to the transmittance of the films, since almost all the films show a similar transmittance. Only the samples annealed at 1050° have a different transmittance than the other films, and the Si doped and undoped samples annealed at 1050°C do have a higher roughness compared to the other samples. This difference is reflected when

[3]A sample which is degenerate has available electron states through infinitesemal excitation, and the thermal energy at 10 K is enough to excite an appreciable amount of electrons into conductive energy states. Increasing the temperature does not increase the number of conduction electrons, just their energies and a degenerate semiconductor has no temperature dependence on its carrier density. This contrasts non-degenerate semiconductors in which the carrier density has a temperature dependence since only electrons with a certain amount of energy can be thermally excited to a conductive energy state.

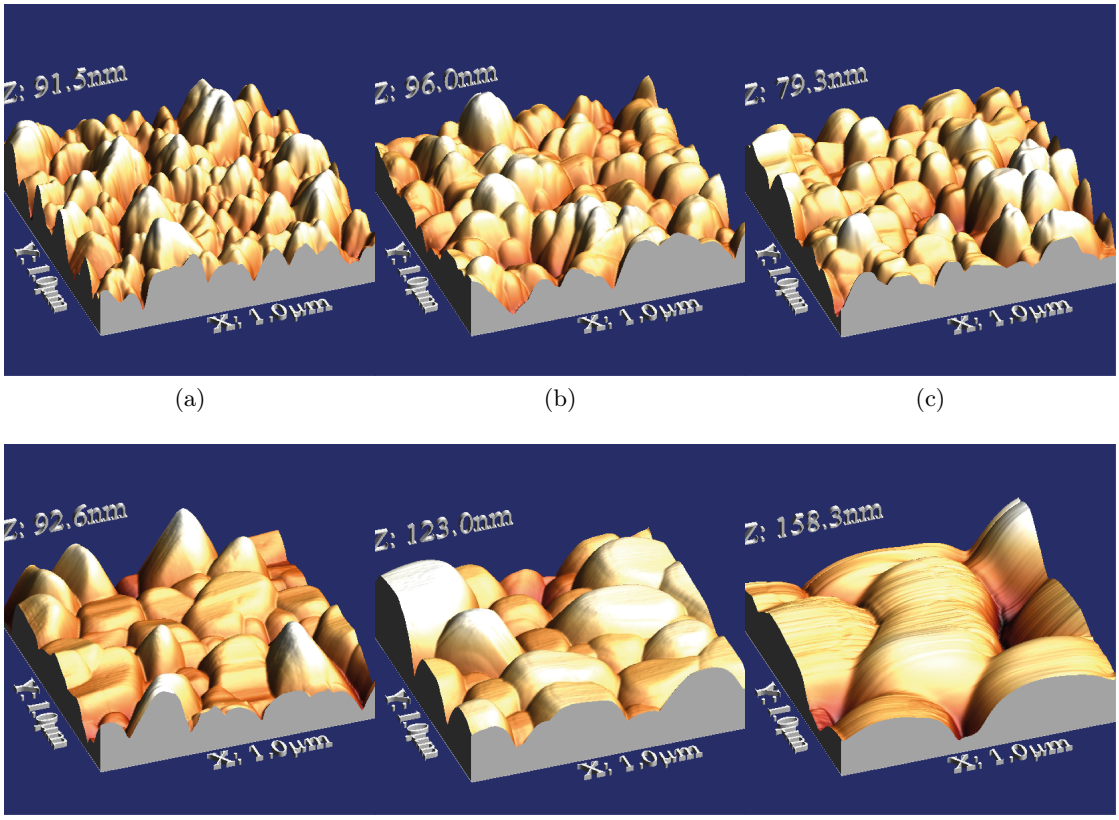

(a) (b) (c)

(d) (e) (f)

Figure 4.25: The evolution of the surface topography of the undoped samples with annealing temperature. (a) As-deposited sample, (b) sample annealed at 550°C, (c) sample annealed at 650°C, (d) sample annealed at 800°C, (e) sample annealed at 950°C, (f) sample annealed at 1050°C. The horizontal grain size increases with increasing annealing temperature

viewing the atomic force micrographs of the films also (figure 4.25). The 1050°C samples have surface features comparable to the wavelength of the probing light in the transmittance measurements, and this is likely the reason for their lower transmittance as compared to the rest of the films. In figure 4.25, the evolution of the surface topography of the undoped samples with annealing temperature is shown. The horizontal grain size increases when annealing, but no significant increase is seen before 800°C. This is representative for the doped samples as well. However, the roughness does not seem to increase significantly below an annealing temperature of 1000°C. The roughness of the samples in table 4.4 is significantly larger than the roughness determined in section 4.2.3, and this can be explained by thicker films for the samples deposited on quartz.

The Atomic Force Micrographs of samples # 1 - # 14 (not shown) do not reveal any big trends other than a slight increase in the apparent lateral grain size as seen on the surface after annealing. The micrographs validate the XRD measurements stating that the films annealed at 1100°C and 1200°C are significantly different than the other films. The roughness of the high temperature samples is higher, and the images show no similarities to the samples annealed below 1000°C. From the micrographs, the lateral size of the grains can be estimated, and for the sample annealed at 650°C deposited on Si + SiO_2, the lateral grain size is in the

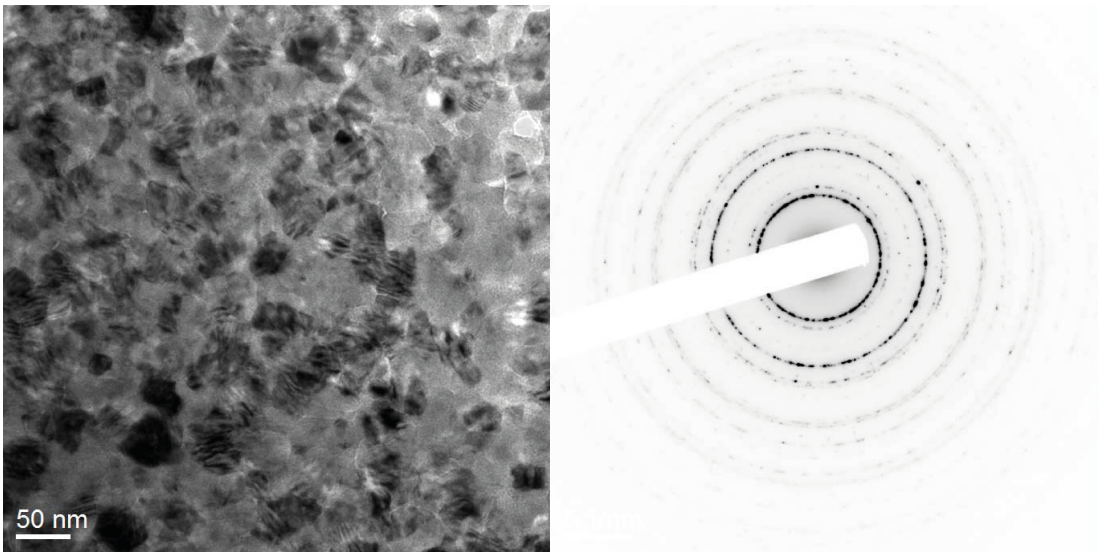

(a) (b)

Figure 4.26: (a) A transmission electron micrograph of sample # 2. (b) A SAD pattern of sample # 2.

range 10^1-10^2 nm, showing that annealing at 650°C of the films on Si + SiO_2 has little effect on the surface topography.

In conclusion, the AFM data of the samples on quartz support the transmittance results stating that the 1050°C films are significantly different than the other films. The roughness and horizontal grain size of the samples increases with annealing temperature, significantly after an annealing temperature of 650°C, but the transmittance is very similar for all films except the films annealed at 1050°C.

4.3.2.5 TEM Results

TEM analysis was due to logistic issues only performed on sample # 2. The investigation revealed that the samples were polycrystalline, and as in section 4.2.6, the sample showed certain grains that were amorphous and some that were crystalline. The lateral size of the grains in the material can be estimated from figure 4.26 (a), and is mostly in the range 20-50 nm as was the case for the as-deposited 12 W Si sample on Si + SiO_2 and is consistent with the grain size estimation from AFM of section 4.3.2.4.

4.3.2.6 PL Results

In section 4.3.1.3, the total integrated PL and the peak at 375 nm of samples # 15 - # 32 (samples deposited on quartz) was discussed in relation to the surfactant action of Si and Al. The peak at 375 nm is however not the only peak in the spectra. From figure 4.12 (a) it is seen that a broad peak emerges around 650 nm when annealing the Si doped samples at 550°C. This peak remains, but another even more prominent, broad peak appears around 500 nm when annealing at 950°C and 1050°C providing evidence that different defects dominate at different annealing temperatures. Annealing at 550°C, 650°C and 800°C produces defects

which promote radiative recombination around 1.8 eV (or around 650 nm). When the Si doped material is annealed at 950°C and 1050°C, a new type of defect which promotes radiative recombination around 2.3 eV (or around 500 nm) is prominent. The same applies for the Al doped material (cf. figure 4.12 (b)), although it seems as if the defect type at 2.3 eV has an onset at a lower annealing temperature since the spectrum from the Al doped sample annealed at 800°C has a certain element of the 2.3 eV peak. It can also be argued that the defects contributing to the large peak around 2.3 eV (evident in the samples annealed at 950°C and 1050°C) are different in the Al doped and Si doped films. In the Si doped films, the peak has a maximum around 2.3 eV, while for the Al doped sample the peak is centered around 2.1 eV.

A similar behaviour is evident in the spectra for the undoped sample, but in these samples the emission is more centered around 2.3 eV (cf. figure 4.11) and little emission is seen around 1.8 eV. The 2.3 eV emission reaches its maximum for the sample annealed at 800°C. This can probably be explained by the higher grain size and better crystal quality for the 800°C sample since there will be more radiative recombination when the bulk-interface ratio is larger and the crystal quality is better. A further difference between the doped and undoped samples is the presence of this peak already in the as-deposited sample. By viewing the spectrum for the as-deposited, undoped sample, it is evident that another defect is also prominent. The spectrum exhibits a peak around 400 nm. The peak gradually vanishes with annealing temperature, and anneals out at 800°C. Examining the total integrated photoluminescence intensity as seen in figure 4.13, it can be argued that the defect that is annealed out changes into a new defect which also emits radiatively since the integrated photoluminescence remains the same until the defect is annealed out at 800°C. The doped samples also have a large increase in total integrated PL intensity from the as-deposited state to annealing at 550°C, and this is due to the emergence of the defects promoting radiative recombination around 1.8 eV

In conclusion, with annealing, defects that promote radiative radiation between 1.8 eV and 2.3 eV appear. For the undoped sample a defect is also present which promotes radiative recombination around 3.0 eV, but this changes into new radiative defects with annealing. The spectra also show a difference between different doping of ZnO supporting the data from sections 4.3.2.1 and 4.3.1.1.

4.3.3 Summary

To improve the mobility, increase the concentration of electrically active dopants in the films and promote precipiation of Si nanocrystals, annealing of Si doped films on Si + SiO_2, Si and quartz substrates as well as annealing of Al doped and undoped films on quartz substrates were done. The crystal quality and grain size of the samples were extracted through XRD and PL and both these properties increased upon annealing, but doping with Si and Al inhibited the grain growth at temperatures below 800°C (as evidenced by XRD, PL and AFM), likely due to a lower mobility of the atoms in the films when Si and Al are present in high concentration. The carrier density of the samples decreased significantly after annealing, in accordance with literature stating that the electron density is decreased when Oxygen chemisorbs on the grain boundaries of the polycrystalline material and/or when V_{Zn} and O_i are formed. These defects can also be related to the mobility. As more Oxygen chemisorbs on the grain boundaries, a higher charge density at the interface results. This leads to more scattering at the grain boundaries, and the mobility is lowered. The compensating V_{Zn} and O_i defects also increase the charge density in the bulk of the grains and this leads to more impurity

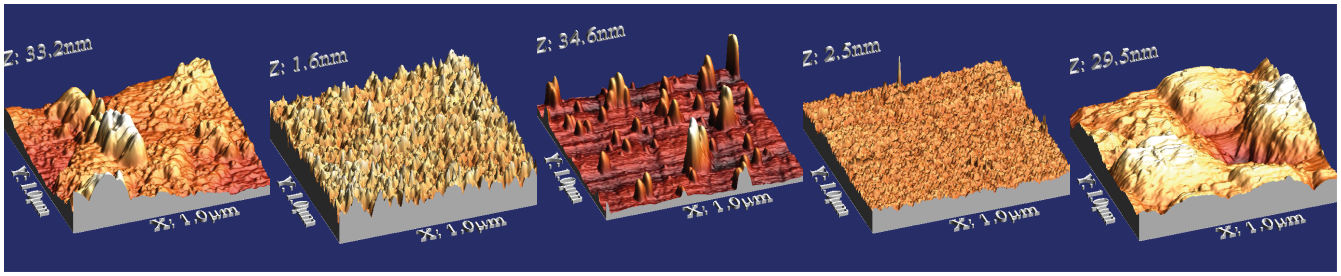

(a) (b) (c) (d) (e)

Figure 4.27: AFM images of the different substrates used in the study. (a) Glass, (b) Thermally grown SiO_2, (c) Quartz, (d) Si, (e) Amorphous ZnO.

scattering. Annealing also increases the horizontal grain size and the surface roughness of the samples as evidenced by AFM. The transmittance of the films is high, and the transmittance in the visible spectrum is not affected by annealing below 1050°C.

4.4 Substrate Series

If ZnO is to be a applicable material in PV applications, it needs to be suitable for different substrates. An understanding of how ZnO behaves on different substrates is therefore important. As already seen in sections 4.2 and 4.3, the substrate used has large impact on the structural characteristics of the material. In these sections, glass, Si + SiO_2, Si and quartz were used as substrates for the films. In addition to these substrates, films were also deposited on amorphous ZnO which was expected to act as a buffer layer promoting crystalline growth of ZnO. Amorphous ZnO was realised by sputtering a film with a 50 W ZnO target power and 25 W Si power on glass. This amorphous layer has a highly rough surface as seen in figure 4.27 (e) and was expected to lead to a better wetting of the surface upon crystalline ZnO growth. In the figure, it can also be seen that the Si and Si + SiO_2 substrates have by far the smoothest surfaces. The Si substrate is crystalline while the Si + SiO_2 substrate is amorphous, and while their surfaces look rather similar, the effect of the crystal nature of the substrates leads to quite different ZnO films. Both quartz and glass consist of SiO_2, but they have a significant different surface topography than thermally grown SiO_2. Quartz has a rough surface on account of sharp protrusions while glass has rather rounded surface features. Glass is a cheap substrate, but contains more impurities than quartz which also has a higher thermal stability.

The films deposited on top of the amorphous ZnO substrate were deposited with a ZnO target power of 50 W and Si target power of 12 W for 35, 70 and 140 minutes. The film thicknesses were not measured since measurement of the thickness using Stylus Profilometry requires etching of the films, and an etch of the films would also remove the substrate. Using deposition rates determined from measured films, the films are expected to have a thickness of around 70, 140 and 280 nm.

Five different substrates were investigated, and although films with different Si target powers were deposited on glass and Si + SiO_2, only films deposited with a 12 W target power (all with a 50 W ZnO target power) are compared in the following sections.

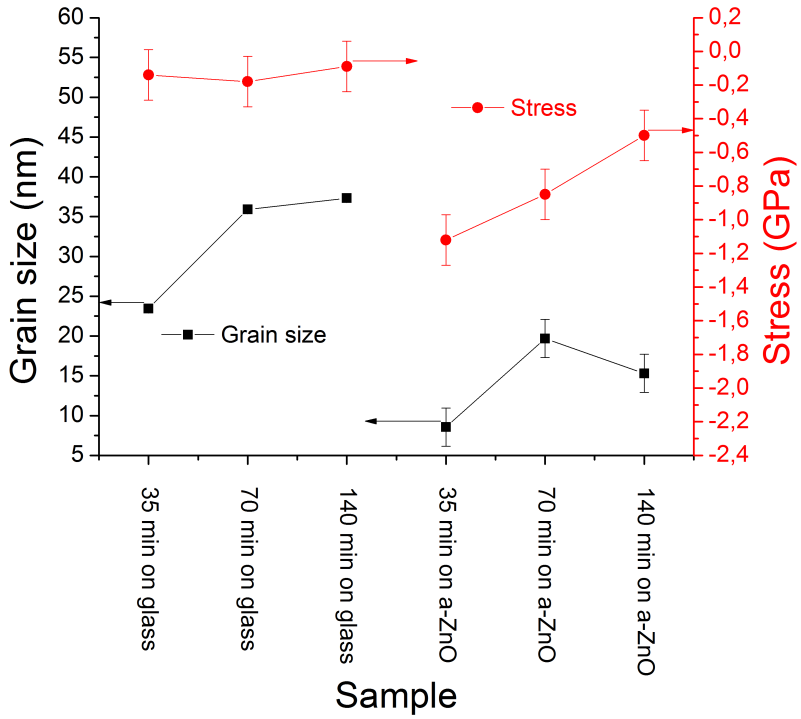

Figure 4.28: The stress and grain size of the samples on glass and amorphous ZnO.

4.4.1 XRD Results

A very important parameter when comparing different substrates is naturally the structural characteristics of the film. To investigate this, XRD measurements were employed.

The films on amorphous ZnO had a deposition time of 35, 70 and 140 minutes. For comparison, films were deposited on glass with the same deposition times, and the stress and the grain size of the films on glass and amorphous ZnO are compared in figure 4.28. The stress decreases when the films on amorphous ZnO get thicker, and seems to approach the values of the samples on glass. This is an indication that the crystallinity is poor for the thin films and that the quality improves as the film gets thicker. The grain size values indicate a similar effect, although it is not as pronounced since the grain size seems to reach a maximum for the film with a 70 minute deposition time. Comparing the intensities of the spectra would provide further evidence that the quality improves, however, the thicknesses of the films are different and the spectra can therefore not be directly compared. Further evidence of a crystallinity improvement with thickness can be found by comparing the films deposited on glass and Si + SiO_2 for 70 min and 220 min respectively. In figure 4.29, the stress and grain size of the four samples are shown. Although the stress does not seem to be affected by the thickness of the films, the grain size for both substrates increases when the films get thicker indicating a better crystal quality. Again, because of different thicknesses of the films, the intensity of the (002) peaks can not be directly compared.

The intensities of the samples on different substrates may not be directly compared neither since the film on amorphous ZnO has a deposition time of 70 minutes while the other films have a deposition time of 220 min. However, as seen in figure 4.30, the difference between the samples is so significant that certain conclusions can be made. Firstly, the intensity of the

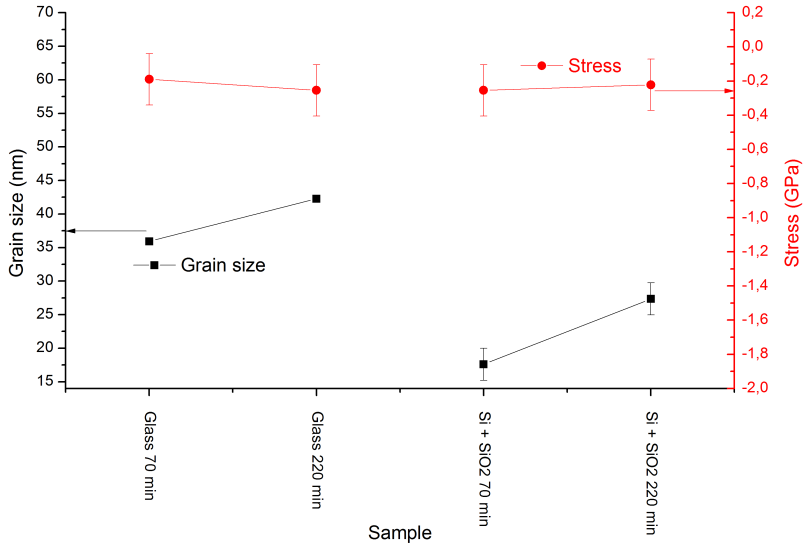

Figure 4.29: The grain size and stress of films with different thicknesses deposited on glass and Si + SiO_2. The crystal quality seems to improve (evidenced by the larger grain size).

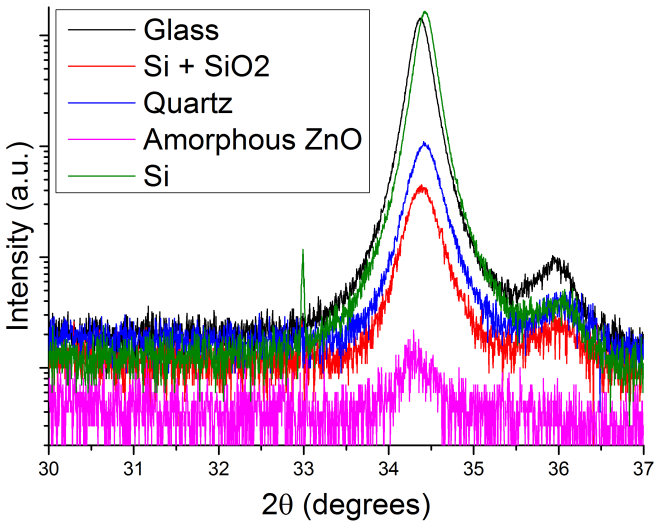

Figure 4.30: The (002) peak of the films on different substrates. The intensity scale is logarithmic. The peak around 36 degrees is the (101) peak of ZnO indicating that the crystal growth is not as highly texturised when the film gets thicker.

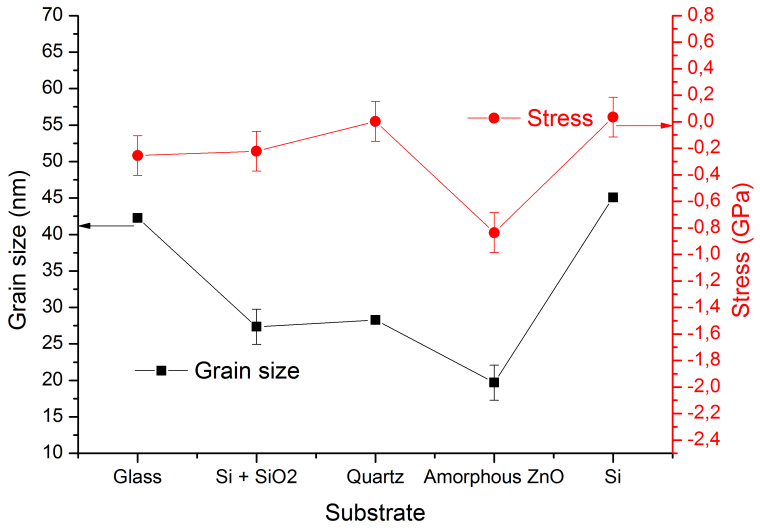

Figure 4.31: The stress and grain size for the samples on different substrates.

(002) peak of the samples on amorphous ZnO is much lower than for all the other samples. This is a strong indication that the crystal quality of the sample is poor, and that crystalline growth on amorhpous ZnO is not favoured and may in fact lead to a close to amorphous layer of ZnO (on top of the amorphous substrate). Secondly, there is a difference between the samples deposited on quartz and Si + SiO_2 since the quartz sample has twice the intensity of the Si + SiO_2 sample. This is reflected in the mobility of these samples, where the sample on quartz has a higher mobility than the sample on Si + SiO_2 (figure 4.33). Thirdly, the intensity of the samples on glass and Si is higher than both the sample on Si + SiO_2 and on quartz, suggesting that the crystal quality of the ZnO films on Si and glass are superior to the other films. Si and glass thus seem to be the most suitable substrates for crystalline growth of Si doped ZnO. The peak around 36 degrees is the (101) peak of ZnO indicating that the crystal growth is not as highly texturised when the film gets thicker. The superior crystal quality provided by the Si and glass substrates is also seen in the grain size in figure 4.31. Here, the grain size is highest for the samples on glass and Si, while the sample on amorpous ZnO has a lower grain size with quartz and Si + SiO_2 somewhere in between. A similar trend can be seen for the stress where the same sample on amorphous ZnO has the highest compressive stress, contradicting the initial motivation for using such a substrate (a bufferlayer was supposed to reduce the stress in the films and improve the crystallinity).

In conclusion, the XRD measurements of samples of different thickness show that the ZnO crystallinity on amorphous ZnO, glass and Si + SiO_2 probably improves as the films get thicker. Comparing different substrates, it is evident that using amorphous ZnO as a substrate is not beneficial to crystal growth of Si doped ZnO, and may in fact lead to close to amorphous ZnO films. Growing films on glass or Si however yields a good crystal quality, while films on Si + SiO_2 or quartz display intermediate crystal quality.

4.4.2 Hall Effect Measurement Results

As previously, the electrical characteristics were investigated using Hall effect measurements. As in section4.4.1 the samples of different thicknesses deposited on glass and amorphous ZnO

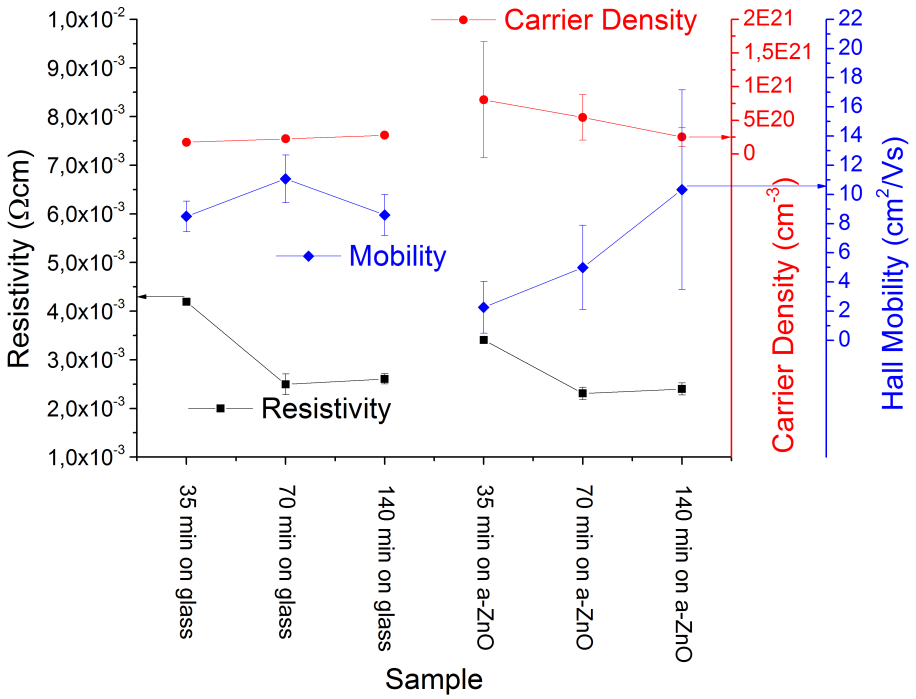

Figure 4.32: The resistivity, carrier density and mobility of the samples on amorphous ZnO with samples on glass for comparison. The mobility and carrier density seems to approach the values of the samples on glass.

are compared, and the resistivity, carrier density and mobility of these 6 samples are shown in figure 4.32. Since the substrate of amorphous ZnO has a resistivity of $\sim 10^{-1}\Omega$cm, corrections to the measured total resistivity and total mobility must be made in order to extract the correct film resistivity and mobility. Such a correction is made through the formulas in equation 4.1.

$$\rho_{film} = \frac{d_{film}}{\frac{d_{tot}}{\rho_{tot}} - \frac{d_{sub}t}{\rho_{sub}}}$$
$$\mu_{film} = \frac{\frac{\mu_{tot}d_{tot}}{\rho_{tot}} - \frac{\mu_{sub}d_{sub}t^2}{\rho_{sub}}}{\frac{d_{film}}{\rho_{film}}} \tag{4.1}$$

Here, d is the thickness of either the film, the substrate or the total, ρ is the resistivity, μ is the mobility while t is a correction factor taking into account that the current must pass through the film to reach the substrate. t is taken to be 1 in this case. An issue with obtaining reliable data by using equation 4.1 is the mobility of the substrate, as the values are very small and not completely reliable. With such low mobility values of the substrate, the correction to the film mobility has little effect.

The carrier density is higher for the films on amorphous ZnO than on glass. The thin sample with a 35 min deposition time has the highest carrier density and as the films gets thicker, the carrier density approaches the value of the films on glass. SIMS measurements revealed that the Si content of the samples on amorphous ZnO and glass is quite similar and differences in carrier density of the samples are thus not related to Si content. Since the 35 min film has

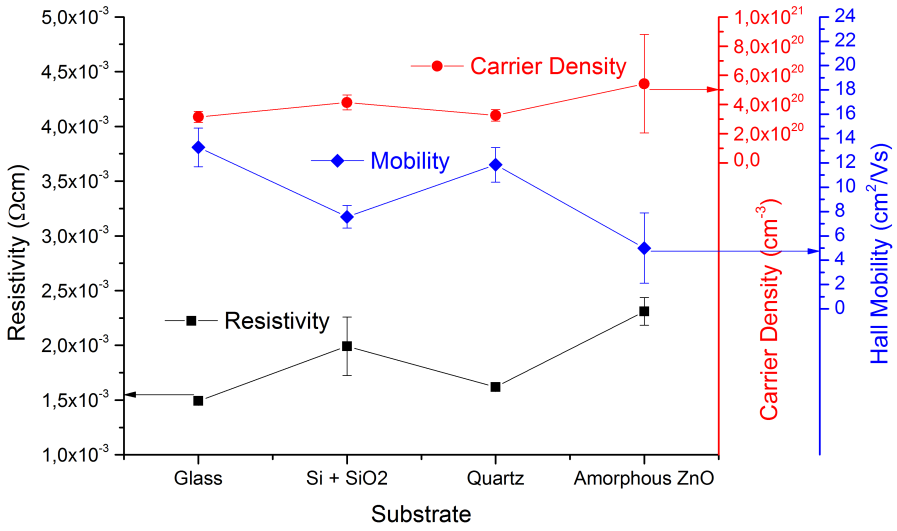

Figure 4.33: The electrical characteristics for films on different substrates. The mobility is highest for the samples on quartz and glass, while the carrier density is highest for the samples on Si + SiO_2 and amorphous ZnO.

a lower crystal quality than the 140 min film, it can be suspected that the amorphous nature of the film is responsible for the high carrier density. The mobility increases with deposition time and approaches the values achieved on glass. As mobility is affected by the density of defects and crystal quality of a material, this may suggest that the material has an improved crystal quality for thicker films. This would imply that the films have a high density of defects near the interface and that they improve with thickness. The amorphous ZnO substrate thus seems to have an adverse effect on the crystal quality of the films. However, compared to the mobility of amorphous Si:H ($\sim$1 $cm^2V^{-1}s^{-1}$), the close to amorphous layers of ZnO exhibit a high mobility, and has rather good electrical properties. As discussed by Nomura et al. [94], the carrier transport in oxide semiconductors occurs between the large and isotropic s orbitals of the metal atoms and is rather insensitive to the crystallinity of the films. This contrasts metal semiconductors, where the directional sp^3 orbitals facilitate the transport. Structural randomness thus greatly affects the bond overlap, and the carrier transport is significantly affected by the crystallinity of the material. This means that the mobility in amorphous oxide semiconductors is superiour to the mobility of metal semiconductors, and this is reflected by the results obtained here.

Comparing the films deposited for 220 minutes (except for the sample on amorphous ZnO with a deposition time of 70 minutes) on different substrates in figure 4.33, it can be seen that the mobility of the films on quartz and glass are the highest. This would suggest a higher crystal quality for these films. The carrier density shows the opposite trend with the samples on amorphous ZnO and Si + SiO_2 showing the highest carrier densities. As discussed previously, the amorphous nature of the films deposited on amorphous ZnO leads to an increased carrier density, and comparing the carrier density of the sample on Si + SiO_2 with the TEM analysis of section 4.2.6 stating that the film contains grains of amorphous nature, supports this claim. Combining the carrier density and the mobility yields the resistivity, and it is seen that the resistivity follows the inverse of the mobility trends and the samples on quartz

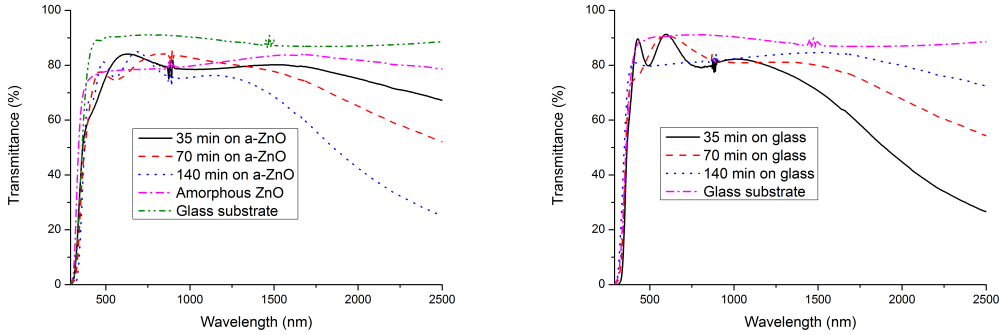

(a) (b)

Figure 4.34: The transmittance of (a) ZnO films with different deposition times on amorphous ZnO and (b) ZnO films with different deposition times on glass.

and glass have the lowest resistivity. The samples on Si substrate are not shown, since the substrate conducted a large part of the current, and limited information on the film could be extracted.

In summary, the electrical characteristics of the films deposited on amorphous ZnO seem to approach the those for films on glass. This suggests that the crystallinity improves and approaches the quality on glass. Although the films deposited on amorphous ZnO are close to amorphous (as seen in section4.4.1 they still exhibit good electrical characteristics. Comparing different substrates, it is clear that the mobility is highest for the samples on glass and quartz indicating that these samples have the best crystal quality. The carrier density shows the opposite behaviour with the films on amorphous ZnO and Si + SiO_2 giving the highest densities, and it is suggested that the amorphous nature of these films leads to an enhanced carrier density.

4.4.3 Transmittance Measurement Results

Transmittance measurements of the samples can provide important information on the electrical and structural characteristics as seen previously. Furthermore, a high transmittance is important when considering the utilisation of ZnO as a transparent conductive electrode. Of the samples compared in section4.4.1, only the samples on quartz, glass and amorphous ZnO have been measured by transmittance measurements. This is due to the non-transparent nature of the Si and Si + SiO_2 substrates.

Figure 4.34 shows the transmittance of the films of different thickness deposited on amorphous ZnO and glass. It is important to note that the films on amorphous ZnO have two interfaces (Si doped ZnO/a-ZnO and a-ZnO/glass) the light must pass through in addition to the surfaces on each side of the glass slab. This will lower the apparent transmittance of the films. In figure 4.34 (a), a plasmonic interference effect is seen for the films. According to the Hall effect measurements, the 35 min sample had the highest carrier density with a decreasing carrier density with thicker films. The plasmonic interference of the transmittance measurements contradicts those values as the sample with lowest transmittance in the SWIR range (indicating highest carrier density) is the 140 min sample with the 35 min sample showing the highest transmittance in this area. However, the plasmon vibration frequency does not

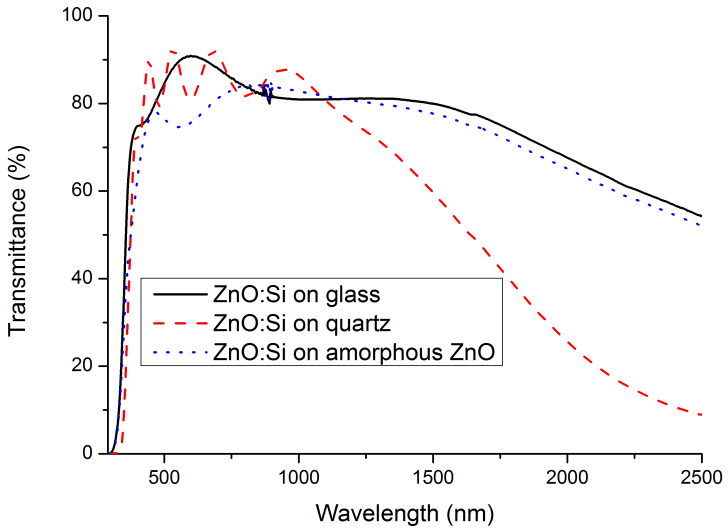

Figure 4.35: The transmittance of films on quartz, glass and amorphous ZnO

only depend on the number of electrons, and the different thicknesses of the films are likely to affect the onset of the plasmonic interference. By inspecting the transmittance around 300 nm, a slight blue-shift can be seen from the 140 min sample through the 70 min to the 35 min sample. Using the method outlined in section 3.4, the optical band gaps of the 35 min sample is estimated to 3.9±0.1 eV, the 70 min sample 3.8±0.1 eV and the 140 min sample to 3.7±0.1 eV (correcting for both the glass and the a-ZnO substrate). This supports the Hall effect results. On glass, the plasmonic interference situation is the opposite with the 35 min sample having the highest plasmonic interference and 140 min the lowest while there is a blue-shift from the 35 min sample to the 140 min sample, and the substrate is also a factor influencing the plasmonic interference. However, an estimation of the band gaps leads to a higher band gap for the 35 min sample. The transmittance in the SWIR range and the absorption around 300 nm thus confirm each other and states that the carrier density of the 35 min sample is the highest. This contradicts the values from the Hall effect measurements of the samples on glass.

In the visible range, the films on amorphous ZnO have a similar transmittance except for the different reflectance oscillation at the different thicknesses. The transmittance is low compared to the samples on glass, and this can probably be ascribed to the amorphous ZnO substrate and possibly the lower crystal quality of the films, but is reasonably high with a transmittance of around 80% in the visible spectrum. The films prepared on amorphous ZnO thus have good electrical and optical properties although they are close to amorphous. Such films may find an application as transparent flexible thin-film transistors [94].The transmittance of the films on glass seems to decrease with thicker films since a thicker film will absorb more of the light than a thinner film.

In figure 4.35, the transmittance of the films deposited on quartz, glass and amorphous ZnO are compared. The transmittance is naturally influenced by which substrate is used, and the difference in the visible range can just as well be ascribed to the differences in the substrates as in the films. As seen previously, the onset of the plasmonic intereference is not

Sample	Roughness (nm)
35 min on amorphous ZnO	2.6 ± 0.7
70 min on amorphous ZnO	2.9 ± 0.5
140 min on amorphous ZnO	5.9 ± 1.8

Table 4.5: The average roughness of the samples on amorphous ZnO.

only determined by the concentration of electrons, but also by the thickness of the film and the substrate. The differences in the SWIR range can for this reason not be used for any significant conclusions. Around 300 nm, the samples are slightly different with a blue-shift from the quartz sample via the amorphous ZnO sample to the glass sample. Estimating the optical band gaps give 3.5±0.1 eV for the glass sample, 3.7±0.2 eV for the quartz sample and 3.8±0.1 eV for the sample on amorphous ZnO. Although the values between different substrates are not directly comparable (since the film-substrate interface is different), it is interesting that the values confirm the Hall effect measurements stating that the sample on amorphous ZnO has the highest carrier density.

In conclusion, the transmittance measurements partly confirm the Hall effect measurements as band gap estimations of the samples on different substrates is consistent with the carrier densities from the Hall effect measurements. The transmittance in the SWIR range is more difficult to interpret, and different thicknesses and substrates in addition to carrier densities probably explain the differences between the samples. In the visible range, the samples on amorphous ZnO have a lower transmittance, but this may just as well be due to a less transmittive substrate as structural differences in the films. Regardless of how much the transmittance is influenced by the substrate, the transmittance of the films on amorphous ZnO substrates are reasonably good, and amorphous films with good optical and electrical properties have been prepared.

4.4.4 AFM Results

Table 4.5 gives the surface roughness of the samples with different deposition times on amorphous ZnO, and an increased roughness with thickness occurs. Comparing with the surface topography of the samples shown in figure 4.36, the roughness difference for the samples seems to reflect the topography. The 35 min and 70 min sample are quite similar, but the 140 min sample has large protrusions on the edge of the image, and these give a high roughness. The structures may be just contamination on the surface, or it may actually be the emergence of superstructures on the surface with thicker films. This superstructure then leads to larger lateral grains when the film is sufficiently thick. This is seen in figure 4.37, where the surface topography of films deposited on glass and Si + SiO_2 for 70 and 220 min, respectively, are shown in addition to a sample deposited on Si for 120 min. The surface topography changes for both the films on glass and Si + SiO_2, with significantly larger lateral grain size for the films deposited for 220 min. The thickness of the film displayed in figure 4.37 (e) (Si doped ZnO film on Si deposited for 120 min) is somewhere in between the thicknesses of the films in 4.37 (a)-(d), and the emergence of the superstructures are apparent. Comparing 4.37 (e) with the sample in figure 4.38 (c) (Si doped ZnO film deposited for 220 min on Si) shows that for even thicker films, the superstructures dominate. The lateral grain size thus increases as the films get thicker, and this reflects the results from the XRD analysis where the vertical grain size increases with thickness. The AFM data are therefore further evidence that the crystal

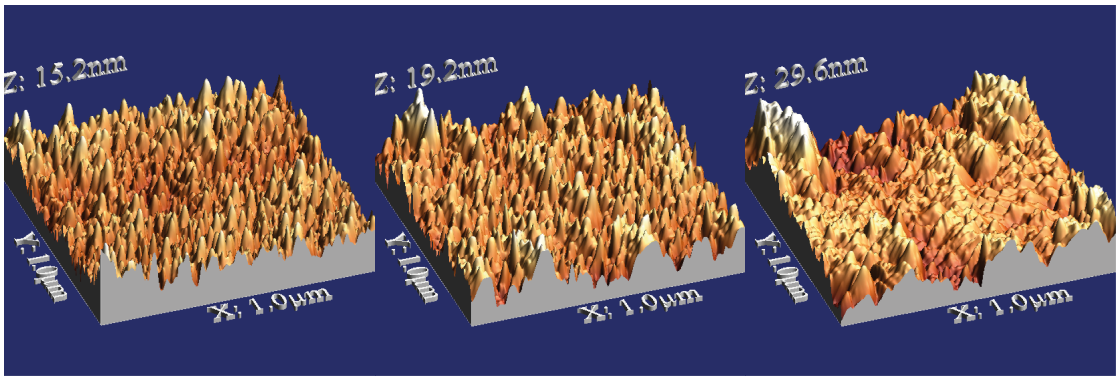

(a) (b) (c)

Figure 4.36: The surface topography of (a) sample deposited for 35 minutes on amorphous ZnO, (b) sample deposited for 70 minutes on amorphous ZnO and (c) sample deposited for 140 minutes on amorphous ZnO.

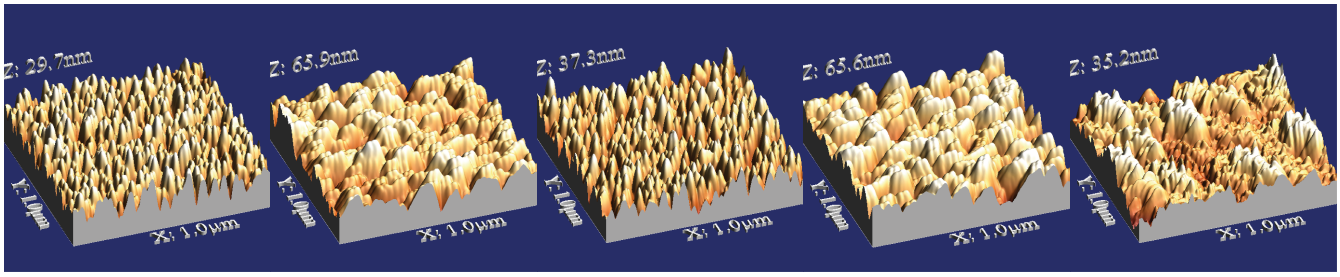

(a) (b) (c) (d) (e)

Figure 4.37: The surface topography of a Si doped ZnO film (a) deposited on glass for 70 min, (b) deposited on glass for 220 min, (c) deposited on Si + SiO_2 for 70 min, (d) deposited on Si + SiO_2 for 220 min and (e) deposited on Si for 120 min.

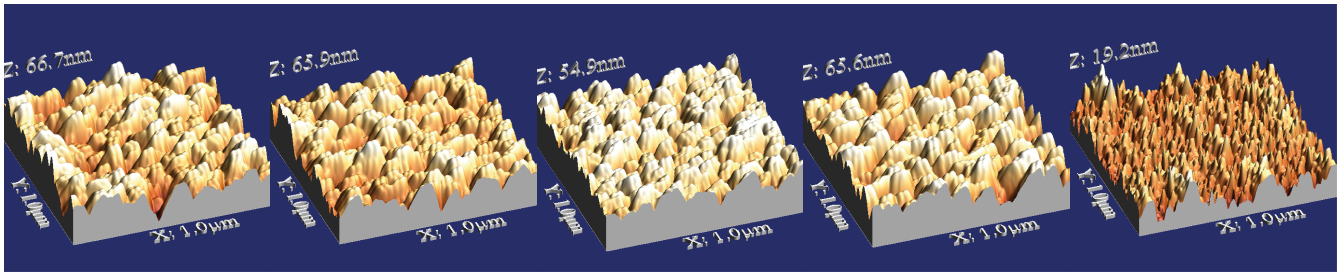

(a) (b) (c) (d) (e)

Figure 4.38: The surface topography of (a) Si doped ZnO on quartz, (b) Si doped ZnO on glass, (c) Si doped ZnO on Si, (d) Si doped ZnO on Si + SiO_2 and (e) Si doped ZnO on amorphous ZnO. The films all have a deposition time of 220 min, except the sample on amorphous ZnO which has a deposition time of 70 min.

Sample	Roughness (nm)
Sample on quartz	10.8 ± 0.8
Sample on glass	8.9 ± 0.7
Sample on Si	7.1 ± 0.5
Sample on Si + SiO_2	10.0 ± 0.5
Sample on amorphous ZnO	2.9 ± 0.5

Table 4.6: The average roughness of samples deposited on quartz, glass, Si, Si + SiO_2 and amorphous ZnO.

structure improves with thicker films.

In figure 4.38, the atomic force micrographs of the samples on quartz, glass, Si, Si + SiO_2 and amorphous ZnO is shown. All the samples are quite similar, except the sample deposited on amorphous ZnO, and this is reflected in the surface roughness presented in table 4.6. Although this may indicate differences in the crystal characteristics, it is more likely that the thickness difference is the key parameter in explaining the difference in the surface topography and surface roughness. Due to the similarities of the surface topography of the thick films, it is difficult to correlate the AFM data with the XRD results and the transmittance measurements.

In conclusion, the AFM images and analysis show that the surface lateral grain size of the films grows as the film thickness increases. This can be related to the larger vertical grain size and improved crystal quality determined by XRD. The samples on different substrates behave quite similarly and it is difficult to correlate these results to the data from other techniques or to draw any clear conclusions.

4.4.5 Summary

The electrical, optical and structural characteristics of a ZnO film naturally depend on which substrate is used. To quantify this dependence, Si doped ZnO films were deposited on glass, quartz, Si, Si + SiO_2 and amorphous ZnO and subsequently characterised by Hall effect measurements, XRD, transmittance measurements and AFM.

From XRD, it can be seen that the crystal quality of the films deposited on amorphous

ZnO improves with increasing thickness. However, the XRD signal is very low for all the films suggesting that the films are close to amorphous. The electrical characteristics obtained from the Hall effect measurements of the Si doped films on amorphous ZnO showed that the carrier density seemed to decrease when the films got thicker. Further, the films seemed to display improved carrier mobility when they got thicker supporting the XRD data suggesting that the crystal quality improves with thicker films and that amorphous ZnO is not a beneficial substrate for growing crystalline ZnO. The transmittance of the films partly supports the Hall effect measurements with a band gap estimation stating that the thinnest film has the highest carrier density. The transmittance in the visible region was around 80%. From this it is clear that by depositing Si doped ZnO films on amorphous ZnO, amorphous films with good electrical and optical characteristics can be obtained. Such films may be utilised to fabricate transparent flexible thin-film transistors. The AFM analysis supported the XRD measurements stating that the crystal quality improved as the films got thicker.

Comparison of the different substrates through XRD proved that amorphous ZnO was not a favourable substrate for growing crystalline ZnO, while Si and glass produced films of high crystal quality. Si + SiO_2 and quartz produced films of intermediate crystal quality. The transmittance measurements (cf. figure 4.35) is influenced by the different substrates and thicknesses, and just like the AFM analysis of the samples on different substrates it is difficult to extract any conclusive information from the data.

Chapter 5

Discussion

The work in this thesis can be divided into three parts with different focus. The study started with producing highly Si doped ZnO films with the aim of obtaining embedded Si nanocrystals. To this end, sputtering was employed and Hall effect measurements, XRD, AFM, TEM, RBS and transmittance measurements were used to search for Si nanocrystals and to characterise the films. The focus of the study then shifted to the highly interesting result obtained from Hall effect measurement showing that by annealing the films in air, the conductivity changed from n-type to p-type. The same techniques as in the first part, in addition to PL, were involved in preparing and characterising the films. A thorough study of the effect of annealing temperature and doping was hence done. In the third part, the effect of different substrates and film thicknesses on the properties of the films were investigated to provide a broader study including more parameters.

5.1 Si Nanocrystals

Si nanocrystals can through multiple exciton generation (MEG) act as down-converting agents to make solar cells more efficient. The quantum confinement of the nanocrystals, makes MEG a probable relaxation process for electrons in the Si nanocrystal [47]. If Si nanocrystals could be embedded in a ZnO matrix, this material could act as both a TCO and a down-converting layer on top of a photovoltaic cell, increasing the efficiency of the cell above the Shockley-Queisser limit. Following the work of Lai et al. [48] and Schofield [49], co-sputtering of ZnO and Si was used to produce films where the Si content was high enough for Si nanocrystals to precipitate. The films that gave the highest quality with regards to electrical and structural characteristics proved to be films sputtered with a ZnO target power of 50 W and Si target power of 12 W. To improve the mobility of the Zn, O and Si/Al atoms during film deposition, the samples were deposited at an elevated substrate temperature of 400°C.

If Si nanocrystals were present in the films, evidence of this would be possible to see by XRD, TEM, PL and FTIR as Lai et al. found in their study from 2008. In figure 2.10 (a), XRD spectra of films with different Si content from this study are displayed. Comparing with the XRD spectrum in figure 4.1 obtained from the 12 W Si target power sample on glass, it can be seen that the films in the present study have a much more directional growth than the films in the study by Lai et al. since only the (002) peak of ZnO is visible in figure 4.1 while in 2.10 (a), several ZnO related peaks are seen. Furthermore, there are no Si related peaks in the spectrum of figure 4.1 suggesting that the Si atoms in the film are rather uniformly

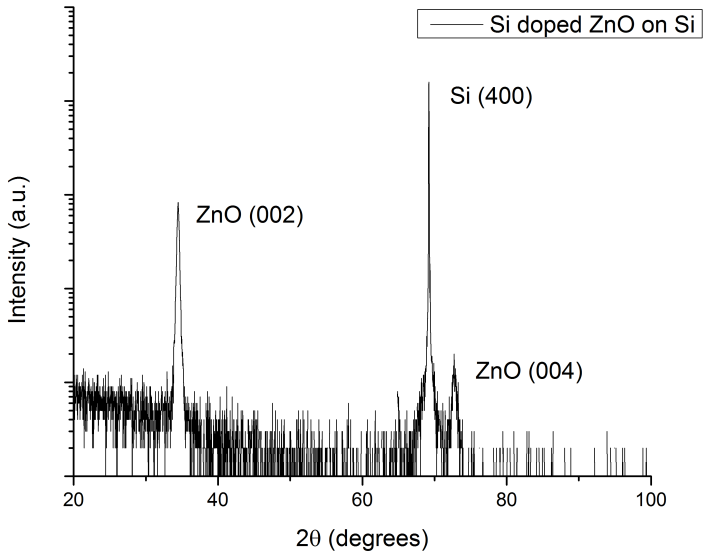

Figure 5.1: The XRD spectrum of a sample deposited on Si with a 12 W Si target power. The Si related peak around 70 degrees originates from the substrate, while the two other peaks are ZnO related.

distributed and no Si phases have precipitated. In figure 2.10 (a), several Si related peaks are seen, and a large volume of Si has precipitated in the films. That this large volume is present as Si nanocrystals is evidenced by TEM and figure 2.10 (b) shows HRTEM images which prove the presence of Si nanocrystals. Although HRTEM has not been used in the present study, "ordinary" TEM analysis presented no evidence of any Si precipitation in the films deposited on Si + SiO_2 with a 12 W Si target power.

To promote the formation of Si nanocrystals, quartz, Si and amorphous ZnO were used as substrates instead glass and Si + SiO_2. As seen in figure 4.30, the XRD signal and hence the crystal quality of the samples on amorphous ZnO was poor. No Si related peaks were present in the spectrum neither. The same applies for the samples on quartz although the crystal quality was quite good. The samples on Si naturally had Si related peaks as seen in figure 5.1, but these originated from the substrate. As XRD gave no indication of Si nanocrystal formation, TEM analysis of the films were not attempted (primarily due to logistic issues).

Another approach to producing the Si nanocrystals was by increasing the mobility of the atoms in the lattice, to make more Si atoms cluster together and forming precipitates. The higher mobility was achieved by thermal annealing in air for 1h at temperatures ranging from 550°C to 1200°C as described in section 4.3. Si + SiO_2, Si and quartz were used as substrates, but none of the XRD spectra of the samples showed any Si nanocrystal related peaks (exemplified by figure 5.2). The absence of Si nanocrystals was confirmed by TEM on a sample deposited on Si + SiO_2 and annealed at 650°C as seen in figure 4.26, where a TEM micrograph and SAD pattern are displayed. All the reflections seen in the SAD pattern can be assigned to ZnO reflections. Lai et al. also detected photoluminescence emitted by Si nanocrystals and were able to calculate the band gap of the Si nanocrystals using the intensity of the PL peak. PL spectroscopy was also utilised in the present study. All the samples on quartz were characterised, but no Si nanocrystal emission could be found in figure 4.12 (a). It can not be ruled out, however, that the emission is too weak to be resolved relative to the

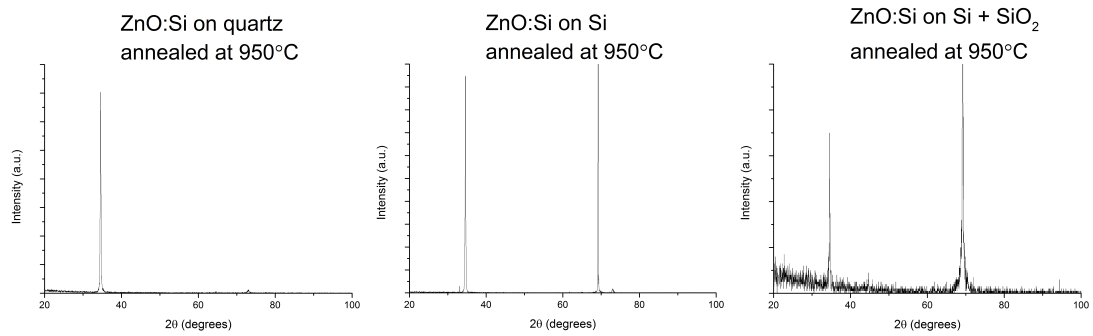

(a) (b) (c)

Figure 5.2: The XRD spectra of samples annealed at 950°C on different substrates. No Si nanocrystal related peak is visible.

more intense emission from the ZnO film itself.

Varying the substrates used and using post-deposition annealing to promote Si nanocrystal formation have proved fruitless since none of the analysis techniques utilised show any evidence of precipitation of Si nanocrystals. The procedure set forth by Lai et al. has been followed as far as possible, and the only deviation is the use of different substrate (Lai et al. used sapphire) and the deposition temperature (400°C in the present study vs no heating in the report from Lai et al.).

The most likely explanation as to why Si nanocrystals do not form is the ease with which SiO_2 forms compared to ZnO. The Gibbs free energy change of formation of SiO_2 is -856.7 kJ/mol, while the Gibbs free energy change of formation of ZnO is -318.3 kJ/mol [95]. The reaction

$$2ZnO(s) + Si(s) \rightleftharpoons 2Zn(s) + SiO_2(s) \tag{5.1}$$

will then have a Gibbs free energy gain of -220.1 kJ/mol and will be dominant as long as it is kinetically viable. This means that Si nanocrystal formation is not favoured in the ZnO lattice, rather will SiO_2 form. Although the Gibbs free energy change of formation of SiO_2 will probably be different when the Si (s) in equation 5.1 is not elemental but situated at substitutional positions in the crystal, SiO_2 is probably far more stable than ZnO, and SiO_2 formation will be preferred over Si nanocrystal formation. By increasing the diffusivity of the atoms via heat treatment, the formation of Si nanocrystals will not be promoted but rather will the increased mobility lead to more formation of SiO_2 since more Si and ZnO will be in contact. The formation of Si nanocrystals could, therefore, possibly be more favourable at low temperatures when the atoms have a low mobility.

5.2 P-type ZnO

One of the results that came out of the search for Si nanocrystals was the p-type conductivity exhibited by some of the annealed samples. The p-type ZnO was first discovered in samples annealed at 650°C and 950°C on Si + SiO_2 substrates (samples # 2 and # 3). SiO_2 proved to be an unfavourable substrate with regards to crystal quality, and ZnO films were deposited on quartz to make a broader investigation with undoped, Al doped and Si doped ZnO and with more extensive annealing treatments.

	Undoped	Si doped	Al doped
As-deposited	Ambiguous	n-type	n-type
550°C	p-type	n-type	n-type
650°C	n-type	n-type	p-type
800°C	n-type	Ambiguous	Ambiguous
950°C	Ambiguous	Ambiguous	Ambiguous
1050°C	p-type	p-type	p-type

Table 5.1: The type of conductivity in the different samples deposited on quartz. "Ambiguous" signifies that the measurements were not conclusively n or p-type.

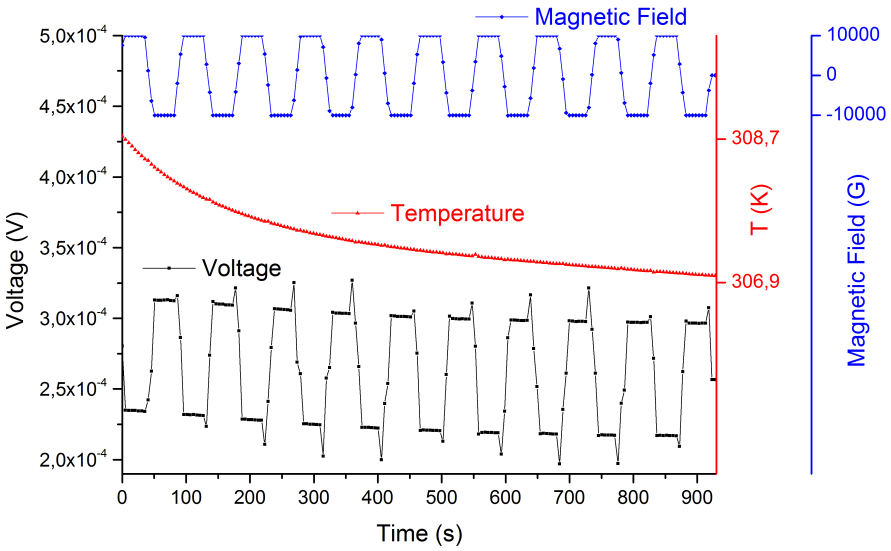

Figure 5.3: The voltage response to an applied magnetic field of the as-deposited Si doped sample on quartz. The voltage follows the magnetic field.

The p-type conductivity seemed to occur rather randomly as seen in table 5.1. One of the trends that can be seen by viewing both table 5.1 and figure 4.14 is that the onset of inconclusive measurements occurs when the resistivity is higher than 100 Ωcm (at 800°C for Si doped, at 650°C for Al doped and for the undoped as-deposited sample). This onset coincides with the unreliable carrier density measurements mentioned in section 4.3.2.1. The carrier densities are determined from the Hall voltage through equation 3.10, but for the samples with a resistivity above 100 Ωcm no Hall voltage was discernible when voltage tracking measurements were employed. This is problematic when determining the type of conductivity as well since this determination is made by looking at the sign of the averaged Hall voltage (averaged over negative and positive magnetic field and current direction). In figure 5.3, the voltage response of the Si doped as-deposited sample is shown. In this film, the voltage response is good, and the voltage follows the magnetic field. As the voltage is out of phase with the magnetic field, the material would be determined as n-type (in this particular set up). When a sample behaves as this, there are no problems in unambiguously determining the carrier density and type of conductivity. However, in figure 3.7 the magnetic field does not seem to have an effect on the measured voltage at all. This can be understood from the misalignment of the contacts

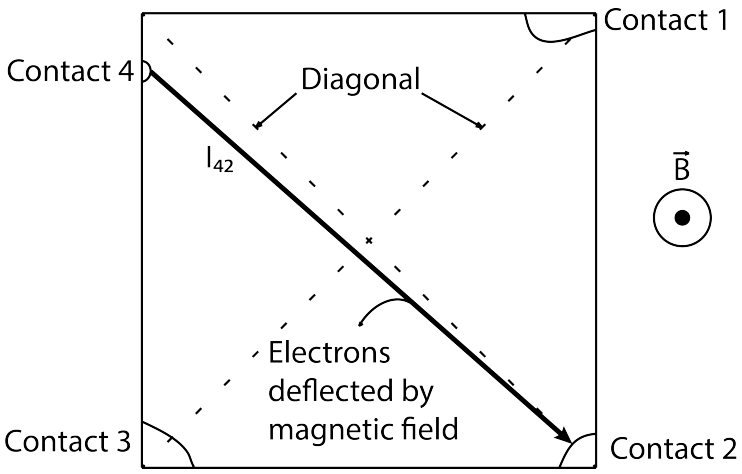

Figure 5.4: When a current is passed from contact 4 to contact 2, electrons are deflected towards contact 3, and a voltage difference is measured between contact 1 and contact 3. However, if the contacts are misaligned as seen in the figure, the current will have a component along the diagonal between contact 1 and 3. This current component will give rise to a voltage equal to the current component times the resistance of the sample ($V_{13} = R \times I_{13}$). This voltage can add or substract the contribution from the Hall voltage depending on the misalignment.

as explained in figure 5.4. In the figure, the contacts are misaligned, and this gives rise to a voltage along the diagonal from contact 1 to contact 3. The magnitude of this voltage depends on the resistivity of the sample, and at large resistivities (above 100 Ωcm), the misalignment voltage dominates the total measured voltage between contact 1 and 3 and the Hall voltage can not be determined (with a misalignment of 0.5mm, a sample resistivity of 100Ωcm and excitation current of 10 μA, the misalignment voltage would be $\sim$ 0.7 V for the samples on quartz). The misalignment voltage can be eliminated by reversing the current and subtracting the measurement at negative direction from the measurement at positive direction (this will cancel the misalignment voltage, but double the Hall voltage). However, as seen in figure 3.7, the measured voltage of sample # 29 is highly dependent on temperature (a temperature drop of 6°C gives a voltage difference of 0.4 V). A measurement of the voltage at positive and negative current direction will thus not cancel out (since the temperature may have drifted between measurements) and the subtracted voltage will give a significant contribution to the voltage used to extract the carrier density and the type of conductivity. Depending on whether the misalignment and temperature drift yield a positive or negative contribution to the voltage between contact 1 and 3, an apparent n-type or p-type film results. This explains why the samples with a resistivity higher than 100 Ωcm yield random conductivity type results.

P-type ZnO is elusive, and the preliminary results yielding p-type ZnO by an easy pathway through annealing in air were promising. However, as discussed above, the p-type behaviour was most probably due to the misalignment of the contacts and the strong temperature dependence of the resistivity.

5.3 Substrate Series

During the course of the thesis work, different substrates have been utilised with glass, Si + SiO_2, amorphous ZnO and Si used to promote formation of Si nanocrystals while quartz

was used due to practical issues regarding annealing the films (thermal stability, good crystal quality and easy Hall effect measurements). The films deposited on these substrates had already been characterised, and a comparative analysis of the films on different substrates was then natural.

The most significant difference between the films on different substrates is the poor crystal quality found on amorphous ZnO compared to the others. This difference was evidenced through XRD measurements where the intensity of the (002) ZnO peak was very low for the films on amorphous ZnO (cf. figure 4.30). The films deposited on quartz and Si + SiO_2 proved to have a better crystal quality than amorphous ZnO, but the films deposited on Si + SiO_2 with a 70 min deposition time also showed a low XRD signal (figure 4.4) indicating a poor crystal quality. TEM analysis of the samples on Si + SiO_2 show that a significant number of the grains in the films were in fact amorphous, and it is likely that this is the cause of the low XRD signal. Although the samples on amorphous ZnO have not been analysed by TEM, they probably exhibit the same amorphous nature. The origin of the films exhibiting both amorphous and crystalline grains has not been investigated, but it can be speculated that different nucleation mechanisms will apply for different grains during the film growth. The crystal quality of the samples on glass and Si were quite good, with Si giving the highest intensity for the (002) reflection of ZnO. Comparing the surface of the substrates in figure 4.27 shows that Si and Si + SiO_2 have very similar surface topographies. However, these two substrates produced very different films in terms of crystallinity, and this might suggest that a polar surface or an amorphous material or a combination (Si + SiO_2) therof is not favourable for ZnO crystal growth. However, glass is also amorphous and polar, but produced films of similar crystal quality as Si. The crystal growth of the films as a function of substrate thus seems to be a complex matter where several variables must be considered.

The electrical characteristics of the films on amorphous ZnO and Si were hard to extract since the substrates conducted a fair amount of the current and influenced the results. For the films on amorphous ZnO it was possible to extract information on the films through equation 4.1, but for the films on Si this was not possible. There was no big differences between the films, but the samples deposited on amorphous ZnO and Si + SiO_2 exhibited a higher carrier density and lower mobility than the samples on glass and quartz(figure 4.33). The amorphous nature of these films thus seems to promote a higher carrier density, while the poor crystal quality yields a lower mobility. Although the mobility in the films on amorphous ZnO is lower than the mobility in the films on quartz and glass, it is still superior to the mobility achieved in a-Si:H, and the electrical properties of the films are rather good. The transmittance of these films in the visible spectrum is around 80%, and it seems that by using amorphous ZnO and possibly Si + SiO_2 as a substrate, amorphous films with good electrical and optical characteristics can thus be accomplished by sputtering. Such films are relevant for the realisation of transparent flexible thin-film transistors for use in paper displays and wearable computers [94].

Chapter 6

Conclusion

6.1 Summary

Si doped, Al doped and undoped ZnO films have been prepared by RF/DC magnetron co-sputtering and subsequently characterised by Hall effect measurements, XRD, transmittance measurements, AFM, TEM, PL spectroscopy, RBS and stylus profilometry. The films were deposited on glass, Si + SiO_2 (thermally grown SiO_2 on a Si wafer), amorphous ZnO, quartz and Si.

It was attempted to precipitate Si nanocrystals in the ZnO matrix by having a high Si concentration (1.5±0.5%). Such Si nanocrystals are suitable for down-converting the energetic part of the solar spectrum (blue light) to less energetic radiation (red light) through a pathway known as multiple exciton generation [47]. By down-converting the solar spectrum, less energy is lost through thermalisation in a photovoltaic cell, and more efficient cells can be made. Different substrates and post-deposition annealing of the films were utilised in order to promote the formation of Si nanocrystals, but no evidence of such structures could be found with any of the characterisation techniques. It is argued that if clusters of Si would form, these would react with the ZnO in the films to yield SiO_2 since SiO_2 has a lower formation energy than ZnO.

It has been shown that the optimum electrical and structural characteristics of the sputtered films were achieved when using a Si target power of 12 W and a ZnO target power of 50 W. This coincides with what has been reported previously using the same set up [49].

Upon annealing, the films were determined to have a p-type conductivity. This is a property rarely found in ZnO. A broad investigation where Al doped, Si doped and undoped ZnO films were annealed at different temperatures ranging from 550°C to 1200°C was made. Several of the films exhibited p-type conductivity, but unfortunately the p-type conductivity as determined by Hall effect measurements was probably not real, but rather due to the misalignment of the contacts and the strong temperature dependence of the resistivity.

When annealing the films in air, the crystal quality, grain size and stress increased. The improvement of the structural characteristics prevailed up to a temperature of 1050°C-1100° where a change of phase to Zinc Silicate occured. Doping the films with Si and Al somehow inhibited the growth of grains at temperatures below 800°C. The carrier density of the films decreased significantly with annealing, and this is explained by chemisorption of Oxygen at the grain boundaries of the polycrystalline films and the creation of the compensating, intrinsic acceptors V_{Zn} and O_i. The chemisorbed Oxygen creates defects which trap electrons, and

the net carrier density is reduced. The carrier mobility is reduced, possibly as a result of the higher density of defects at the interface and in the bulk (through Oxygen chemisorption and V_{Zn} and O_i formation) leading to more grain boundary and impurity scattering.

Investigation of the effect of different substrates on the films revealed that amorphous ZnO is a substrate which is not beneficial for crystalline ZnO growth (evidenced through TEM and XRD). However, the near amorphous films yielded good electrical and optical characteristics; thus by depositing Si doped ZnO on amorphous ZnO, low resistive, transmittive, amorphous films can be produced. This result is interesting in regards to realisation of transparent flexible thin-film transistors. Using Si or glass as substrates proved to yield films with satisfactory structural characteristics, while deposition on quartz and thermally grown SiO_2 produced films with an intermediate crystal quality. It was also seen that the crystallinity of the films improved as the films got thicker.

6.2 Suggestions for Future Work

Annealing of ZnO in air proved to be disadvantageous for the electrical characteristics of the films since both the carrier density and the mobility decreased. To determine if the cause of the decrease in carrier density is due to Oxygen chemisorption or creation of V_{Zn} and O_i, an investigation using different ambients (such as forming gas, nitrogen and vacuum) and characterisation techniques such as XPS and SIMS in addition to the ones already used could be made.

A broader substrate investigation could be made by applying more characterisation techniques (e.g. XPS, TEM and FTIR) and more substrates (e.g. monocrystalline ZnO and sapphire).

To get a higher understanding of the Hall effect results which presented p-type conductivity in ZnO, a more thorough study where the temperature is controlled and the contacts are lithographically defined could be made. Taking these measures would provide accurate numbers for the misalignment voltage, the Hall voltage and the temperature drift of the resistivity.

Si nanocrystals were not possible to produce with the sputtering parameters used in the present study. Lai et al. [48] produced Si nanocrystals in a ZnO matrix by deposition on sapphire and with no heating of the substrate. The low diffusivity of the atoms at room temperature could promote Si nanocrystal formation and sputtering Si doped ZnO at a low temperature could hence be a viable route to explore. However, the low formation energy of SiO_2 compared to ZnO is likely to be an obstacle in Si nanocrystal formation. A different approach which avoids the issue with SiO_2 is by forming nanocrystals of a different material which has a oxide with a higher formation energy. A possible element in this regard is Germanium. The Gibbs free energy change of formation of GeO_2 (the most common oxide of Ge) is -497.1 kJ/mol [95]. This means that the reaction

$$2ZnO(s) + Ge(s) \rightleftharpoons 2Zn(s) + GeO_2(s) \tag{6.1}$$

has a Gibbs free energy of 139.5 kJ/mol and the left side of the reaction will be favoured. Co-sputtering of Ge and ZnO or implantation of Ge in ZnO in a concentration above the solid solubility limit could therefore lead to precipitation of Ge nanocrystals embedded in the ZnO matrix. If further work regarding down-converting ZnO is to be pursued, this could be a successful pathway.

Bibliography

[1] R. E. Smalley, "Top Ten Problems Facing Humanity Over the Next 50 years." http://cnst.rice.edu/content.aspx?id=246, 2003.

[2] International Energy Agency, "World Energy Outlook 2012," November 2012.

[3] International Panel on Climate Change, "IPCC Fourth Assessment Report: Climate Change 2007 (AR4)," 2007.

[4] International Panel on Climate Change, "Renewable Energy Sources and Climate Change Mitigation," 2011.

[5] G. W. Crabtree and N. S. Lewis, "Solar energy conversion," *Physics Today*, vol. 60, pp. 37–42, MAR 2007.

[6] B. Andersson, "Materials availability for large-scale thin-film photovoltaics," *Progress in Photovoltaics*, vol. 8, pp. 61–76, JAN-FEB 2000.

[7] C. Kittel and P. McEuen, *Introduction to Solid State Physics*. Wiley, 8th ed., 2005.

[8] P. C. Hemmer, *Faste Stoffers Fysikk*. Tapir Forlag, 1987.

[9] B. G. Streetman and S. K. Banerjee, *Solid State Electronic Devices*. Pearson Prentice-Hall, 6th ed., 2010.

[10] F. Bloch, "About the Quantum mechanics of Electrons in Crystal lattices.," *Zeitschrift für Physik*, vol. 52, pp. 555–600, JUL 1929.

[11] U. Ozgur, Y. I. Alivov, C. Liu, A. Teke, M. A. Reshchikov, S. Dogan, V. Avrutin, S. J. Cho, and H. Morkoc, "A comprehensive review of ZnO materials and devices," *Journal of Applied Physics*, vol. 98, AUG 15 2005.

[12] S. J. Pearton, D. P. Norton, K. Ip, Y. W. Heo, and T. Steiner, "Recent progress in processing and properties of ZnO," *Progress in Materials Science*, vol. 50, pp. 293–340, MAR 2005.

[13] R. B. Heller, J. Mcgannon, and A. H. Weber, "Precision Determination of the Lattice Constants of Zinc Oxide," *Journal of Applied Physics*, vol. 21, no. 12, pp. 1283–1284, 1950.

[14] S. J. Clark, J. Robertson, S. Lany, and A. Zunger, "Intrinsic defects in ZnO calculated by screened exchange and hybrid density functionals," *Physical Review B*, vol. 81, MAR 2010.

[15] S. Lany and A. Zunger, "Dopability, intrinsic conductivity, and nonstoichiometry of transparent conducting oxides," *Physical Review Letters*, vol. 98, JAN 26 2007.

[16] F. Tuomisto, K. Saarinen, K. Grasza, and A. Mycielski, "Observation of Zn vacancies in ZnO grown by chemical vapor transport," *Physica Status Solidi B-Basic Solid State Physics*, vol. 243, pp. 794–798, MAR 2006. 12th International Conference on II-VI Compounds, Warsaw, POLAND, SEP 12-16, 2005.

[17] A. Janotti and C. G. Van de Walle, "Native point defects in ZnO," *Physical Review B*, vol. 76, OCT 2007.

[18] T. R. Paudel and W. R. L. Lambrecht, "First-principles calculation of the O vacancy in ZnO: A self-consistent gap-corrected approach," *Physical Review B*, vol. 77, MAY 2008.

[19] F. Oba, A. Togo, I. Tanaka, J. Paier, and G. Kresse, "Defect energetics in ZnO: A hybrid Hartree-Fock density functional study," *Physical Review B*, vol. 77, JUN 2008.

[20] D. C. Look, J. W. Hemsky, and J. R. Sizelove, "Residual native shallow donor in ZnO," *Physical Review Letters*, vol. 82, pp. 2552–2555, MAR 22 1999.

[21] A. F. Kohan, G. Ceder, D. Morgan, and C. G. Van de Walle, "First-principles study of native point defects in ZnO," *Physical Review B*, vol. 61, pp. 15019–15027, JUN 1 2000.

[22] F. Oba, M. Choi, A. Togo, A. Seko, and I. Tanaka, "Native defects in oxide semiconductors: a density functional approach," *Journal of Physics - Condensed Matter*, vol. 22, SEP 29 2010. 3rd International Workshop on Theory Meets Industry, Nagoya Int, Nagoya, JAPAN, NOV 11-13, 2009.

[23] C. G. Van de Walle, "Hydrogen as a cause of doping in zinc oxide," *Physical Review Letters*, vol. 85, pp. 1012–1015, JUL 31 2000.

[24] S. F. J. Cox, E. A. Davis, S. P. Cottrell, P. J. C. King, J. S. Lord, J. M. Gil, H. V. Alberto, R. C. Vilao, J. P. Duarte, N. A. de Campos, A. Weidinger, R. L. Lichti, and S. J. C. Irvine, "Experimental confirmation of the predicted shallow donor hydrogen state in zinc oxide," *Physical Review Letters*, vol. 86, pp. 2601–2604, MAR 19 2001.

[25] T. Minami, H. Sato, H. Nanto, and S. Takata, "Highly Conductive and Transparent Silicon Doped Zinc-Oxide Thin-Films Prepared by RF Magnetron Sputtering," *Japanese Journal of Applied Physics Part 2-Letters*, vol. 25, pp. L776–L779, SEP 1986.

[26] A. K. Das, P. Misra, and L. M. Kukreja, "Effect of Si doping on electrical and optical properties of ZnO thin films grown by sequential pulsed laser deposition," *Journal of Physics D - Applied Physics*, vol. 42, AUG 21 2009.

[27] C. H. Park, S. B. Zhang, and S. H. Wei, "Origin of p-type doping difficulty in ZnO: The impurity perspective," *Physical Review B*, vol. 66, AUG 15 2002.

[28] N. Y. Garces, N. C. Giles, L. E. Halliburton, G. Cantwell, D. B. Eason, D. C. Reynolds, and D. C. Look, "Production of nitrogen acceptors in ZnO by thermal annealing," *Applied Physics Letters*, vol. 80, pp. 1334–1336, FEB 25 2002.

[29] M. Taguchi, K. Kawamoto, S. Tsuge, T. Baba, H. Sakata, M. Morizane, K. Uchihashi, N. Nakamura, S. Kiyama, and O. Oota, "HIT (TM) cells - High-efficiency crystalline Si cells with novel structure," *Progress in Photovoltaics*, vol. 8, pp. 503–513, SEP-OCT 2000.

[30] T. Mishima, M. Taguchi, H. Sakata, and E. Maruyama, "Development status of high-efficiency HIT solar cells," *Solar Energy Materials and Solar Cells*, vol. 95, pp. 18–21, JAN 2011. 19th International Photovoltaic Science and Engineering Conference and Exhibition (PVSEC-19), Jeju, SOUTH KOREA, NOV 09-13, 2009.

[31] T. Minami, "Transparent conducting oxide semiconductors for transparent electrodes," *Semiconductor Science and Technology*, vol. 20, pp. S35–S44, APR 2005.

[32] A. Suzuki, T. Matsushita, N. Wada, Y. Sakamoto, and M. Okuda, "Transparent conducting Al-doped ZnO thin films prepared by pulsed laser deposition," *Japanese Journal of Applied Physics Part 2-Letters*, vol. 35, pp. L56–L59, JAN 1 1996.

[33] A. Suzuki, T. Matsushita, T. Aoki, Y. Yoneyama, and M. Okuda, "Pulsed laser deposition of transparent conducting indium tin oxide films in magnetic field perpendicular to plume," *Japanese Journal of Applied Physics Part 2-Letters*, vol. 40, pp. L401–L403, APR 15 2001.

[34] D. C. Look and B. Claftin, "P-type doping and devices based on ZnO," *Physica Status Solidi B-Basic Solid State Physics*, vol. 241, pp. 624–630, MAR 2004. 11th International Conference on II-VI Compounds, NIAGARA FALLS, NY, SEP 22-26, 2003.

[35] S. B. Zhang, S. H. Wei, and A. Zunger, "Intrinsic n-type versus p-type doping asymmetry and the defect physics of ZnO," *Physical Review B*, vol. 63, FEB 15 2001.

[36] K. Minegishi, Y. Koiwai, Y. Kikuchi, K. Yano, M. Kasuga, and A. Shimizu, "Growth of p-type zinc oxide films by chemical vapor deposition," *Japanese Journal of Applied Physics Part 2-Letters*, vol. 36, pp. L1453–L1455, NOV 1 1997.

[37] K. Iwata, P. Fons, A. Yamada, K. Matsubara, and S. Niki, "Nitrogen-induced defects in ZnO : N grown on sapphire substrate by gas source MBE," *Journal of Crystal Growth*, vol. 209, pp. 526–531, FEB 1 2000. 7th International Conference on Chemical Beam Epitaxy and Related Growth Techniques (ICCBE-7), TSUKUBA, JAPAN, JUL 28-30, 1999.

[38] Y. F. Yan, S. B. Zhang, and S. T. Pantelides, "Control of doping by impurity chemical potentials: Predictions for p-type ZnO," *Physical Review Letters*, vol. 86, pp. 5723–5726, JUN 18 2001.

[39] E. C. Lee, Y. S. Kim, Y. G. Jin, and K. J. Chang, "Compensation mechanism for N acceptors in ZnO," *Physical Review B*, vol. 64, AUG 15 2001.

[40] T. Yamamoto and H. Katayama-Yoshida, "Solution using a codoping method to unipolarity for the fabrication of p-type ZnO," *Japanese Journal of Applied Physics Part 2-Letters*, vol. 38, pp. L166–L169, FEB 15 1999.

[41] M. Joseph, H. Tabata, and T. Kawai, "p-type electrical conduction in ZnO thin films by Ga and N codoping," *Japanese Journal of Applied Physics Part 2-Letters*, vol. 38, pp. L1205–L1207, NOV 1 1999.

[42] T. Yamamoto, "Codoping for the fabrication of p-type ZnO," *Thin Solid Films*, vol. 420, pp. 100–106, DEC 2 2002. 29th International Conference on Metallurgical Coatings and Thin Films, SAN DIEGO, CALIFORNIA, APR 22-26, 2002.

[43] L. G. Wang and A. Zunger, "Cluster-doping approach for wide-gap semiconductors: The case of p-type ZnO," *Physical Review Letters*, vol. 90, JUN 27 2003.

[44] L. Balakrishnan, S. Gowrishankar, P. Premchander, and N. Gopalakrishnan, "Dual codoping for the fabrication of low resistive p-ZnO," *Journal of Alloys and Compounds*, vol. 512, pp. 235–240, JAN 25 2012.

[45] K. K. Kim, H. S. Kim, D. K. Hwang, J. H. Lim, and S. J. Park, "Realization of p-type ZnO thin films via phosphorus doping and thermal activation of the dopant," *Applied Physics Letters*, vol. 83, pp. 63–65, JUL 7 2003.

[46] M. C. Beard, K. P. Knutsen, P. Yu, J. M. Luther, Q. Song, W. K. Metzger, R. J. Ellingson, and A. J. Nozik, "Multiple exciton generation in colloidal silicon nanocrystals," *Nano Letters*, vol. 7, pp. 2506–2512, AUG 2007.

[47] A. J. Nozik, M. C. Beard, J. M. Luther, M. Law, R. J. Ellingson, and J. C. Johnson, "Semiconductor Quantum Dots and Quantum Dot Arrays and Applications of Multiple Exciton Generation to Third-Generation Photovoltaic Solar Cells," *Chemical Reviews*, vol. 110, pp. 6873–6890, NOV 2010.

[48] L.-W. Lai, C.-H. Liu, C.-T. Lee, L.-R. Lou, W.-Y. Yeh, and M.-T. Chu, "Investigation of silicon nanoclusters embedded in ZnO matrices deposited by cosputtering system," *Journal of Materials Research*, vol. 23, pp. 2506–2511, SEP 2008.

[49] M. D. Schofield, "ZnO Deposited by Magnetron Sputtering Incorporating Si Nanocrystals," Master's thesis, University of Oslo, 2011.

[50] R. Sæterli, "Private Communication," 2013.

[51] R. W. Miles, G. Zoppi, and I. Forbes, "Inorganic photovoltaic cells," *Materials Today*, vol. 10, pp. 20–27, NOV 2007.

[52] S.-M. Park, T. Ikegami, and K. Ebihara, "Effects of substrate temperature on the properties of Ga-doped ZnO by pulsed laser deposition," *Thin Solid Films*, vol. 513, pp. 90–94, AUG 14 2006.

[53] K. Ellmer, "Resistivity of polycrystalline zinc oxide films: current status and physical limit," *Journal of Physics D - Applied Physics*, vol. 34, pp. 3097–3108, NOV 7 2001.

[54] T. Minami, "New n-type transparent conducting oxides," *MRS Bulletin*, vol. 25, pp. 38–44, AUG 2000.

[55] M. K. Puchert, P. Y. Timbrell, and R. N. Lamb, "Postdeposition annealing of radio frequency magnetron sputtered ZnO films," *Journal of Vacuum Science & Technology A - Vacuum Surfaces and Films*, vol. 14, pp. 2220–2230, JUL-AUG 1996.

[56] P. Nunes, E. Fortunato, and R. Martins, "Influence of the post-treatment on the properties of ZnO thin films," *Thin Solid Films*, vol. 383, pp. 277–280, FEB 15 2001. 3rd Symposium O on Thin Film Materials for Large Area Electronics of the E-MRS 2000 Spring Meeting, STRASBOURG, FRANCE, MAY 30-JUN 02, 2000.

[57] B. Du Ahn, S. H. Oh, C. H. Lee, G. H. Kim, H. J. Kim, and S. Y. Lee, "Influence of thermal annealing ambient on Ga-doped ZnO thin films," *Journal of Crystal Growth*, vol. 309, pp. 128–133, DEC 1 2007.

[58] T. Minami, H. Nanto, S. Shooji, and S. Takata, "The Stability of Zinc-Oxide Transparent Electrodes Fabricated by RF Magnetron Sputtering," *Thin Solid Films*, vol. 111, no. 2, pp. 167–174, 1984.

[59] H. Tong, Z. Deng, Z. Liu, C. Huang, J. Huang, H. Lan, C. Wang, and Y. Cao, "Effects of post-annealing on structural, optical and electrical properties of Al-doped ZnO thin films," *Applied Surface Science*, vol. 257, pp. 4906–4911, MAR 15 2011.

[60] S. Major, A. Banerjee, and K. L. Chopra, "Annealing Studies of Undoped and Indium-Doped Film of Zinc-Oxide," *Thin Solid Films*, vol. 122, no. 1, pp. 31–43, 1984.

[61] F. Ruske, M. Roczen, K. Lee, M. Wimmer, S. Gall, J. Huepkes, D. Hrunski, and B. Rech, "Improved electrical transport in Al-doped zinc oxide by thermal treatment," *Journal of Applied Physics*, vol. 107, JAN 1 2010.

[62] L. Tang, B. Wang, and J. Wang, "Effect of post-annealing ambient on electrical structural properties and optical properties of ZnO:Al transparent films," in *Materials and Manufacturing, Pts 1 and 2* (Wang, JH and Qi, JG, ed.), vol. 299-300 of *Advanced Materials Research*, (LAUBLSRUTISTR 24, CH-8717 STAFA-ZURICH, SWITZERLAND), pp. 675–678, Liaoning Univ Technol, TRANS TECH PUBLICATIONS LTD, 2011. International Conference on Materials and Manufacturing (ICMM 2011), Jinzhou, PEOPLES R CHINA, SEP 07-09, 2011.

[63] C. K. To, B. Yang, S. C. Su, C. C. Ling, C. D. Beling, and S. Fung, "Post-growth annealing induced change of conductivity in As-doped ZnO grown by radio frequency magnetron sputtering," *Journal of Applied Physics*, vol. 110, DEC 1 2011.

[64] S. Limpijumnong, S. B. Zhang, S. H. Wei, and C. H. Park, "Doping by large-size-mismatched impurities: The microscopic origin of arsenic- or antimony-doped p-type zinc oxide," *Physical Review Letters*, vol. 92, APR 16 2004.

[65] S. A. Campbell, *Fabrication Engineering at the Micro- and Nanoscale*. Oxford University Press, 3rd ed., 2008.

[66] K. Ellmer, "Magnetron sputtering of transparent conductive zinc oxide: relation between the sputtering parameters and the electronic properties," *Journal of Physics D - Applied Physics*, vol. 33, pp. R17–R32, FEB 21 2000.

[67] J. A. Thornton, "Influence of Apparatus Geometry and Deposition Conditions on Structure and Topography of Thick Sputtered Coatings," *Journal of Vacuum Science & Technology*, vol. 11, no. 4, pp. 666–670, 1974.

[68] G. Braeuer, B. Szyszka, M. Vergoehl, and R. Bandorf, "Magnetron sputtering - Milestones of 30 years," *Vacuum*, vol. 84, pp. 1354–1359, JUN 25 2010. 10th International Symposium on Sputtering and Plasma Processes, Kanazawa, JAPAN, JUL 08-10, 2009.

[69] P. Sigmund, "Theory of Sputtering. I. Sputtering Yield of Amorphous and Polycrystalline Targets," *Physical Review*, vol. 184, no. 2, pp. 383–416, 1969.

[70] C. D. Child, "Discharge from hot CaO," *Physical Review*, vol. 32, pp. 0492–0511, MAY 1911.

[71] L. I. Maissel and R. Glang, *Handbook of Thin Film Technology.* McGraw-Hill, 1970.

[72] B. A. Movchan and A. V. Demchishin, "Study of structure and properties of thick vacuum condensates of nickel, titanium, tungsten, aluminium oxide and zirconium dioxide," *Physics of Metals and Metallography-USSR*, vol. 28, no. 4, pp. 83–90, 1969.

[73] E. Lillestøl, O. Hunderi, and J. R. Lien, *Generell fysikk for universiteter og høgskoler, Bind 2 Varmelære og elektromagnetisme.* Universitetsforlaget, 2001.

[74] L. J. van der Pauw, "A Method of Measuring Specific Resistivity and Hall Effect of Discs of Arbitrary Shape," *Philips Research Reports*, vol. 13, pp. 1–9, 1958.

[75] M. Birkholz, P. F. Fewster, and C. Genzel, *Thin Film Analysis by X-Ray Scattering.* Wiley-VCH, 2006.

[76] R. Cebulla, R. Wendt, and K. Ellmer, "Al-doped zinc oxide films deposited by simultaneous rf and dc excitation of a magnetron plasma: Relationships between plasma parameters and structural and electrical film properties," *Journal of Applied Physics*, vol. 83, pp. 1087–1095, JAN 15 1998.

[77] E. Mollwo, *Landolt-Börnstein. Zahlenwerte und Funktionen aus Naturwiss. u. Technik. Neue Serie.* Springer, 1982.

[78] P. Scherrer, "Bestimmung der Grösse und der inneren Struktur von Kolloidteilchen mittels Röntgenstrahlen," *Göttinger Nachrichten Gesellschaft*, vol. 2, p. 98, 1918.

[79] D. Brandon and W. D. Kaplan, *Microstrucural Characterization of Materials.* Wiley, 2nd ed., 2008.

[80] V. M. Mironov, *Fundamentals of Scanning Probe Microscopy.* Russian Academy of Sciences, 2004.

[81] G. Binnig, C. F. Quate, and C. Gerber, "Atomic Force Microscope," *Physical Review Letters*, vol. 56, pp. 930–933, MAR 3 1986.

[82] R. Erni, M. D. Rossell, C. Kisielowski, and U. Dahmen, "Atomic-Resolution Imaging with a Sub-50-pm Electron Probe," *Physical Review Letters*, vol. 102, MAR 6 2009.

[83] G. D. Gilliland, "Photoluminescence spectroscopy of crystalline semiconductors," *Materials Science & Engineering R-Reports*, vol. 18, pp. 99–399, MAR 1997.

[84] W. K. Chu, J. W. Mayer, M. A. Nicolet, T. M. Buck, G. Amsel, and F. Eisen, "Principles and Applications of Ion-Beam Techniques for Analysis of Solids and Thin-Films," *Thin Solid Films*, vol. 17, no. 1, pp. 1–41, 1973.

[85] J. Perriere, "Rutherford Backscattering Spectrometry," *Vacuum*, vol. 37, no. 5-6, pp. 429–432, 1987.

[86] Evans Analytical Group, *RBS Theory Training Tutorial*.

[87] R. Krüger-Sehm, "Stylus Profilometry. In: Wang Q., Chung Y. (Ed.) Encyclopedia of Tribology," 2013.

[88] X. Su and Q. Zhang, "Dynamic 3-D shape measurement method: A review," *Optics and Lasers in Engineering*, vol. 48, pp. 191–204, FEB 2010.

[89] I. Horcas, R. Fernandez, J. M. Gomez-Rodriguez, J. Colchero, J. Gomez-Herrero, and A. M. Baro, "WSXM: A software for scanning probe microscopy and a tool for nanotechnology," *Review of Scientific Instruments*, vol. 78, JAN 2007.

[90] R. Schifano, M. Schofield, L. Vines, S. Diplas, E. V. Monakhov, and B. G. Svensson, "Al and Si doping of sputtered ZnO thin films," in *E-MRS 2011 Fall Symposium I: Advances in Transparent Electronics, from Materials to Devices III*, vol. 34 of *IOP Conference Series-Materials Science and Engineering*, (DIRAC HOUSE, TEMPLE BACK, BRISTOL BS1 6BE, ENGLAND), European Mat Res Soc (E-MRS), IOP PUBLISHING LTD, 2012. Symposium I on Advances in Transparent Electronics, from Materials to Devices III/Fall Meeting of the European-Materials-Research-Society (E-MRS), Warsaw, POLAND, SEP 19-23, 2011.

[91] D. Kandel and E. Kaxiras, "Surfactant-Mediated Crystal-Growth of Semiconductors," *Physical Review Letters*, vol. 75, pp. 2742–2745, OCT 2 1995.

[92] A. V. Singh, R. M. Mehra, N. Buthrath, A. Wakahara, and A. Yoshida, "Highly conductive and transparent aluminum-doped zinc oxide thin films prepared by pulsed laser deposition in oxygen ambient," *Journal of Applied Physics*, vol. 90, pp. 5661–5665, DEC 1 2001.

[93] J. R. Bellingham, W. A. Phillips, and C. J. Adkins, "Intrinsic Performance Limits in Transparent Conducting Oxides," *Journal of Materials Science Letters*, vol. 11, pp. 263–265, MAR 1992.

[94] K. Nomura, H. Ohta, A. Takagi, T. Kamiya, M. Hirano, and H. Hosono, "Room-temperature fabrication of transparent flexible thin-film transistors using amorphous oxide semiconductors," *Nature*, vol. 432, pp. 488–492, NOV 25 2004.

[95] H. Ellis, R. D. Harrison, and H. D. B. Jenkins, eds., *Nuffield Advanced Science: Book of Data*. Longman Group Ltd., 2007.